# Toward the Very Long Baseline Interferometric Calibration of the CHIME/FRB Outriggers

Vishwangi Shah

Master of Science

Department of Physics

McGill University Montreal, Québec

A thesis submitted to McGill University in partial fulfillment of the requirements of the degree of Master of Science

 $\bigodot$ Vishwangi Shah, September 2023

### **ABSTRACT**

Fast Radio Bursts (FRBs) are extremely luminous radio signals of micro-to-millisecond duration with an unknown extragalactic origin. An important step towards constraining models for their progenitors is identifying their host galaxies, or even better, their positions within their hosts. This requires skylocalising FRBs to sub-arcsecond precision which would give a clue about the type of galaxies and local environments in which FRBs occur.

The Canadian Hydrogen Intensity Mapping Experiment Fast Radio Burst (CHIME/FRB) project has observed a large sample of FRBs with its unique design optimised for rapid wide-field observations. The CHIME/FRB Outriggers are a VLBI network of three CHIME-like antennas which will enable the localisation of FRBs to milli-arcsec precision. For calibrating the VLBI network, we plan to employ a novel approach of using pulsars spread over the entire sky as calibrators. The implementation of this approach requires the real-time beamforming of pulsars every second to track a pulsar calibrator as it transits through the sky and saving the beamformed voltage data upon an FRB event to enable offline phase referencing. In this thesis, we describe upgrades made to the rudimentary realtime beamformer to meet these requirements.

KKO, the first CHIME/FRB Outrigger, saw first light in June 2022, and has been in commissioning ever since. With a 66-km line of sight distance to CHIME, it can provide a sky-localisation accuracy of 1 arcsecond. As the pathfinder for the Outriggers, KKO enabled the development and testing of software pipelines aimed at FRB localisation. In this thesis, we will also discuss the pipelines set up to acquire FRB data at the Outriggers, and an analysis carried out to obtain the accuracy and estimated errors of our VLBI calibration techniques.

### ABRÉGÉ

Les sursauts radio rapides (FRB) sont des signaux radio extrêmement lumineux d'une durée de l'ordre de la microseconde à la milliseconde avec une origine extragalactique inconnue. Une étape importante vers des modèles contraignants pour leurs progéniteurs consiste à identifier leurs galaxies hôtes, ou mieux encore, leurs positions au sein de leurs hôtes. Cela nécessite de localiser les FRB dans le ciel avec une précision inférieure à la seconde d'arc, ce qui donnerait une idée du type de galaxies et des environnements locaux dans lesquels les FRB se produisent.

Le projet Canadian Hydrogen Intensity Mapping Experiment Fast Radio Burst (CHIME/FRB) a observé un large échantillon de FRB grâce à sa conception unique optimisée pour des observations rapides à grand champ. Les Outriggers CHIME/FRB sont un réseau VLBI de trois antennes de type CHIME qui permettront au localisation des FRB avec une précision au millième d'arcsec. Pour calibrer le réseau VLBI, nous prévoyons d'employer une nouvelle approche consistant à utiliser des pulsars répartis dans tout le ciel comme calibrateurs. La mise en œuvre de cette approche nécessite la formation de faisceaux en temps réel de pulsars chaque seconde pour suivre un calibrateur de pulsar alors qu'il transite à travers le ciel et enregistre les données de tension formées par le faisceau lors d'un événement FRB pour les activer hors ligne référencement de phase. Dans cette thèse, nous décrivons les améliorations apportées au formateur de faisceaux rudimentaire en temps réel pour répondre à ces exigences.

KKO, le premier Outrigger CHIME/FRB, a vu sa première lumière en juin 2022 et est en mise en service depuis cette date. Avec une distance de visibilité directe de 66 km par rapport à CHIME, il peut fournir une précision de localisation du ciel de 1 seconde d'arc. En tant qu'éclaireur pour les Outriggers, KKO a permis le développement et le test de logiciels pipelines destinés à la localisation des FRB. Dans cette thèse, nous aborderons également les pipelines mis en place pour acquérir des données des FRBs aux Outriggers, et une analyse effectuée pour obtenir l'exactitude et les erreurs estimées de nos techniques d'étalonnage VLBI.

### ACKNOWLEDGEMENTS

Firstly, I want to thank my supervisor, Vicky Kaspi, for providing me the opportunity to work on something as extraordinary as CHIME/FRB, for her constant support and guidance, and for creating a nurturing research environment within the CHIME/FRB collaboration.

I am grateful to Dr. Adam Lanman for his mentorship which helped me learn everything from the very basics of radio astronomy to VLBI. This thesis wouldn't have been possible without him. Thank you to Prof. Kiyoshi Masui, Dr. Calvin Leung, Shion Andrew, and Mattias Lazda for insightful discussions on VLBI. Thank you to Andre Renard and Dr. Mubdi Rahman for sharing your expertise on the technical aspects of CHIME.

Thank you to my friends in India, Shristy, and Akhil, for lending me an ear whenever I needed to talk it out. Thank you to Manas for sharing my curiosity about the cosmos, and for your undying optimism. Thank you to Ayushi for your warmth, care, and all the delicious meals you cooked for us. Thank you to Sri, Viru, Nimo, and Mohan for your friendship and support. Thank you to my friends and colleagues at the Trottier Space Institute, Alice, Ketan, Bridget, and Marcus, for providing motivation (especially during the writing of this thesis) and guidance, and for our Indian cooking nights.

Thank you to Mom and Dad for encouraging me to dream big, for being my inspiration in hard times, and for our daily 9 p.m. calls which make me miss home a little less. Thank you to my little brother for being my confident and steady support for all these years.

### CONTRIBUTIONS

Development of the CHIME/FRB Instrument has largely been a team effort, involving many years of dedicated efforts. Individuals who contributed to the building of this instrument can be found in the author list of CHIME/FRB Collaboration et al. (2021). The baseband pipeline used for ~arcminute precision localisation of FRBs at CHIME was developed by Daniele Michilli. Calvin Leung, Tomás Cassanelli, and Pranav Sanghavi first demonstrated the use of VLBI with CHIME and the CHIME/FRB Outrigger testbeds (ARO and TONE) to localise FRBs to sub-arcsecond precision. They laid the groundwork for the CHIME/FRB Outriggers. The algorithms for VLBI cross-correlation, calibration and localisation were developed by Calvin Leung and Shion Andrew. As we learn more about the availability and usefulness of VLBI calibrators, the VLBI calibration strategy is being actively revised by Shion Andrew, Mattias Lazda and the author.

The realtime beamformer used for pulsar tracking was developed by the authors of CHIME/Pulsar Collaboration et al. (2021). Kotekan and coco were developed by Andre Renard. The ~100 pulsars usable for the calibration of the VLBI network of CHIME and the outriggers were identified by Alice Curtin and Jane Kaczmarek. The algorithm for tracking, gating and cross-correlating pulsar calibrators is in active development by Aaron Pearlman, Calvin Leung and Andre Renard. Calvin Leung and Tomás Cassanelli identified the discrepancy between the realtime beamformer and the offline beamformer used for beamforming FRBs. The development of the upgraded realtime beamformer which fixes this discrepancy is an original contribution from the author.

Commissioning of KKO, the first CHIME/FRB Outrigger, is a team effort led by Adam Lanman. The FRB trigger management system used for acquiring FRB data at KKO was developed by Ryan Mckinven, Shiny Brar, Tarik Zegmott and the author. The utility to schedule baseband acquisition of sources of interest was originally developed by Calvin Leung and set up at KKO by the author. The offline beamforming pipeline was set up at KKO by Mattias Lazda and tested by him, Shion Andrew and the author. The SEFD measurement for KKO and its comparison to CHIME SEFD was done by the author. The pipeline to calculate instrument gains used in the process of beamforming was set up at KKO by Adam Lanman. Testing the effect of these instrument gains on VLBI delays was done by the author. The clock stabilisation pipeline was developed by Juan Mena-Parra and set up at KKO by him and Nina Gusinskaia. The author used this pipeline to measure clock delays. The measurement of the impact of ionosphere and clock-drift on VLBI delays is an original contribution from the author.

# Contents

	ABS	STRAC	T	i			
	ABI	RÉGÉ		ii			
1	$\mathbf{A}\mathbf{n}$	Introd	luction to Fast Radio Bursts	1			
	1.1	Propa	gation Effects	1			
		1.1.1	Dispersion Measure	1			
		1.1.2	Scattering and Scintillation	3			
	1.2	Repea	ting FRBs	3			
	1.3	Locali	sation of FRBs	4			
		1.3.1	VLBI to localise FRBs	5			
		1.3.2	Constraining progenitor models	6			
		1.3.3	Localised FRBs as cosmological probes	10			
2	VLI	BI wit	h CHIME and the Outriggers	13			
	2.1	Detect	ting FRBs with CHIME	13			
		2.1.1	Overview of CHIME	13			
		2.1.2	The CHIME/FRB Instrument	14			
	2.2	Baseb	and data	16			
	2.3	CHIM	E/FRB Outriggers	17			
	2.4	VLBI	Calibration and Localisation algorithms	18			
		2.4.1	Cross-Correlation	18			
		2.4.2	Calibration	20			
		2.4.3	Localisation	24			
3	Realtime Beamforming of Pulsar Calibrators 25						
	3.1	Theor	y of Beamforming	25			
	3.2	The R	Lealtime Beamformer	27			
		3.2.1	Kotekan and Coco	27			
	3.3	Pulsar	rs for VLBI Calibration	28			
	3.4	Upgra	ded Realtime Beamformer	29			
		3.4.1	Methods for Calculating Hour Angles	29			
		3 / 2	Phase Centre and Feed Positions	31			

KK	O: Commissioning and Towards Science Readiness	33
4.1	Overview of KKO	33
4.2	Baseband Data Acquisition	34
	4.2.1 FRB trigger management system	34
	4.2.2 Scheduled acquisition of bright sources	37
4.3	KKO system characteristics	37
	4.3.1 Beamforming tests	37
	4.3.2 Noise Characteristics	37
4.4	VLBI Analysis	39
	4.4.1 Effect of instrument gains on VLBI delays	40
	4.4.2 Effect of clock-drift on VLBI delays	42
	4.4.3 Effect of ionosphere on VLBI delays	43
Cor	nclusion	47
	4.1 4.2 4.3	4.2.1 FRB trigger management system 4.2.2 Scheduled acquisition of bright sources 4.3 KKO system characteristics 4.3.1 Beamforming tests 4.3.2 Noise Characteristics 4.4 VLBI Analysis 4.4.1 Effect of instrument gains on VLBI delays 4.4.2 Effect of clock-drift on VLBI delays

# List of Figures

1.1	Waterfall plot of the Lorimer Burst, the first detected FRB	2
1.2	Figure showing the dispersive sweep of an FRB and its scattering tail	4
1.3	Schematic diagram showing how VLBI is done between two telescopes	6
1.4	Localisation of FRB 121102 and the persistent radio source associated with it	7
1.5	Localisation region of the repeating FRB M81R	8
1.6	Localisation of a repeating FRB close to a star forming region in a spiral galaxy	9
1.7	Plot showing the Macquart relation for 15 localised FRBs	11
2.1	Photo of CHIME	14
2.2	Map showing the locations of CHIME and the CHIME/FRB Outriggers	18
2.3	Amplitude of Crab pulsar cross-correlation for the CHIME-KKO baseline	21
2.4	Correlation power and signal to noise ratio for a CHIME-KKO Crab pulsar cross-correlation	22
3.1 3.2	Schematic diagram showing how beamforming is done for a 3 feed interferometer Differences in hour angle and phases computed by the realtime and offline beamformers .	26 32
4.1		0.5
4.1	Photo of KKO	35
4.2	Schematic diagram of the FRB trigger management system	36
4.3	A test for the beamforming pipeline deployed at KKO	38
4.4	Waterfall plot of the first pulsar pulse detected at KKO	39
4.5	Comparison between the SEFD of CHIME and KKO	40
4.6	Coarse-delay and phase residuals for a CHIME-KKO Crab pulsar cross-correlation	41
4.7	Coarse delay as a function of instrument gains	42
4.8	Clock drifts for the CHIME and KKO clocks	43
4.9	Phase of the cross-correlated visibility when ionospheric impact is negligible	45
4.10	Phase of the cross-correlated visibility when ionospheric impact is not negligible	45
4.11	VLBI delays for 12 data acquisitions spanning 2 hours and taken during night	46
4.12	VLBI delays for 12 data acquisitions spanning 2 hours and taken during sunrise	46

# List of Tables

2.1	Table describing the key properties of CHIME	14
4.1	Table describing the key properties of KKO	34

# Chapter 1

# An Introduction to Fast Radio Bursts

The field of short-duration astrophysical transients emitting coherent radio emission was fast-evolving at the beginning of the 21st century with thousands of radio pulsars known and attempts to find new radio transients by blindly searching for single pulses in archival telescope data. During one such single-pulse search of the Small Magellanic Cloud (SMC) archival data taken by the Parkes telescope in 2001, Lorimer et al. (2007) detected an extremely bright pulse of peak flux density > 30 Jy, lasting only a few milliseconds. This burst, called the Lorimer Burst, had a frequency-dependent dispersive delay (see Section 1.1.1) much greater than that expected from the Milky Way Interstellar Medium (ISM) or even from the SMC suggesting an extra-galactic origin. This opened a new class of these enigmatic astrophysical transients called the Fast Radio Bursts (FRBs). Since then, hundreds of FRBs (CHIME/FRB Collaboration et al., 2021) with micro-millisecond durations (CHIME/FRB Collaboration et al., 2021a; Gajjar et al., 2018), and with a vast range of energies from  $\sim 10^{35}$  erg to  $\sim 10^{41}$  erg (CHIME/FRB Collaboration et al., 2020b) have been reported. The origin of FRBs still remains a mystery. In the following sections, I describe the observational properties of FRBs (Section 1.1), repetition of some FRBs (Section 1.2), and localisation of FRBs to their host galaxies (Section 1.3).

### 1.1 Propagation Effects

#### 1.1.1 Dispersion Measure

As the FRB signal travels from the source to our telescope, the group velocity of the wavefront is frequency dependent in the intervening ionised plasma such that its time of arrival  $t_{arrival}$  is

$$t_{\rm arrival} = -\frac{L}{c} + \frac{e^2}{2\pi m_e c} \frac{{\rm DM}}{\nu^2} \tag{1.1}$$

$$DM = \int_0^L n_e dL \tag{1.2}$$

where L is the distance to the source, c is the speed of light, e is the electron charge,  $m_e$  is the electron mass,  $\nu$  is the observing frequency,  $n_e$  is the free-electron density. The dispersion measure, DM, is the

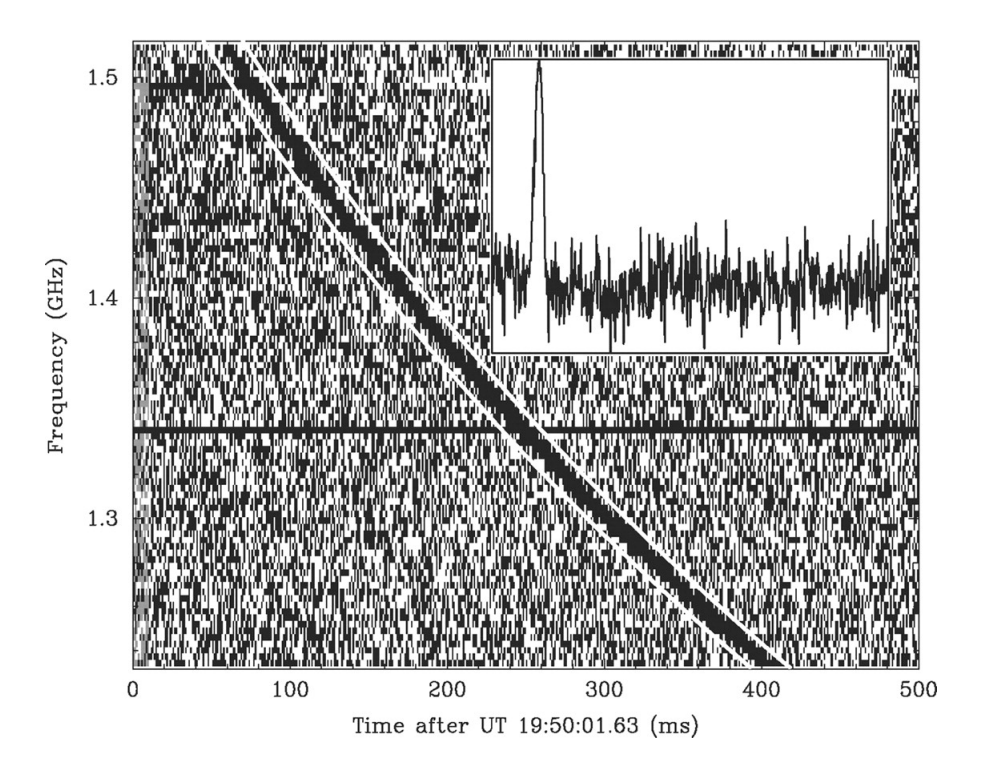


Figure 1.1: Figure taken from Lorimer et al. (2007) showing the dynamic frequency vs. time ("waterfall") plot of the Lorimer Burst. The color scale show the intensity of the signal. The dispersion sweep is clearly visible and corresponds to a DM of 375 pc cm<sup>-3</sup>. The inset shows the total power signal after a dispersive delay correction.

integrated free-electron density along the line of sight to the FRB. The dispersion constant  $k_{\rm DM}$  is defined as

$$k_{\rm DM} = \frac{e^2}{2\pi m_e c} = 4.15 \times 10^3 \text{ s MHz}^2 \text{ pc}^{-1} \text{ cm}^3$$
 (1.3)

It is apparent from Equation 1.1 that higher frequencies arrive earlier than lower frequencies, spreading the FRB signal over frequency and time and causing a dispersion sweep as seen in Figure 1.1. Since FRBs are of extra-galactic origin, their DM encompasses the electron content encountered in their host galaxy ( $DM_{host}$ ), in the intergalactic medium ( $DM_{IGM}$ ), in the interstellar medium of the Milky Way Galaxy ( $DM_{MW,ISM}$ ), and in the Milky Way halo ( $DM_{MW,halo}$ ) such that  $DM_{total}(z)$  is

$$DM_{total}(z) = DM_{MW,ISM} + DM_{DM,halo} + DM_{IGM}(z) + DM_{host}$$
(1.4)

where z is the redshift of the host galaxy. The  $DM_{MW,ISM}$  along different line of sights is estimated using two models, NE2001 (Cordes and Lazio, 2002) and YMW16 (Yao et al., 2017), both calibrated to Galactic pulsars of known DM and distance. The  $DM_{MW,halo}$  is traditionally taken to be  $\sim 50$  pc cm<sup>-3</sup> (Deng and Zhang, 2014), however Cook et al. (2023) recently placed upper limits of 52 - 111 pc cm<sup>-3</sup> on  $DM_{MW,halo}$ . Localising FRBs to host galaxies is crucial for accurately constraining the other contributions to  $DM_{total}(z)$ . After a large sample of spectroscopic-z for the localised host galaxies are available, the mean DM contribution of the IGM can be estimated. As shown by Macquart et al.

(2020), this can in-turn make FRBs useful for investigating some of the fundamental questions about the Universe such as the location of the "missing" baryons (see Section 1.3.3). The line-of-sight to the localized host galaxy can also allow us to estimate the DM contributed by the halos of the intervening foreground host galaxies (Lee et al., 2021). Accounting for all the other DM contributions lets us to extract  $DM_{host}$ , which is highly dependent on the FRB progenitor environment and thus a very useful tool to constrain the progenitor models.

### 1.1.2 Scattering and Scintillation

While the free-electron density along the line of sight causes the FRB signal to be dispersed, the fluctuations in the electron density cause the FRB signal to be scattered. This causes multi-path propagation of signals and later times of arrival for signals with longer paths. For the simple case where there is one thin scattering screen along the line of sight, the multi-path propagation will cause an exponential decay tail for the FRB pulse where the decay time is strongly frequency dependent:

$$\tau \propto \nu^{-4}.\tag{1.5}$$

Figure 1.2 shows the dispersive sweep of FRB 110220 and the inset shows the frequency dependent scattering tail. In VLBI imaging, the scattering tail can cause angular broadening of the imaged FRB such as the angular broadening of FRB 121102 reported in Marcote et al. (2017). In addition to scattering, multi-path propagation can cause wavefronts to constructively and destructively interfere when they meet, causing a complex frequency and time dependent structure of the detected FRB pulse. This is called scintillation.

The inhomogeneities in the electron density causing scattering and scintillation are expected to be present mainly in the FRB host environment, the host galaxy or the Milky Way. Masui et al. (2015), for example, detect scintillation and scattering by two scattering screens in FRB 110523, and associate it with a dense nebula surrounding the FRB source which favors progenitor models involving young stellar populations such as magnetars.

### 1.2 Repeating FRBs

Some Fast Radio Bursts repeat (Spitler et al., 2016; CHIME/FRB Collaboration et al., 2019; Fonseca et al., 2020; CHIME/FRB Collaboration et al., 2023), such that multiple bursts are detected at the same sky position with the same DM. This rules out cataclysmic progenitor models like compact object mergers or collapse of neutron stars (Platts et al., 2019) for at least this class of FRBs. Repeating FRBs are seen to have wider burst durations and narrower bandwidths (Pleunis et al., 2021b) than the apparent non-repeaters, suggesting intrinsic differences between the two classes of FRBs or propagation effects related to distinct local and host-galaxy environments. CHIME/FRB Collaboration et al. (2023) also report that repeating FRBs are seen to have average DM less than that of apparent non-repeaters, although this could also be a result of an observational bias since it is easier to detect a repeat burst

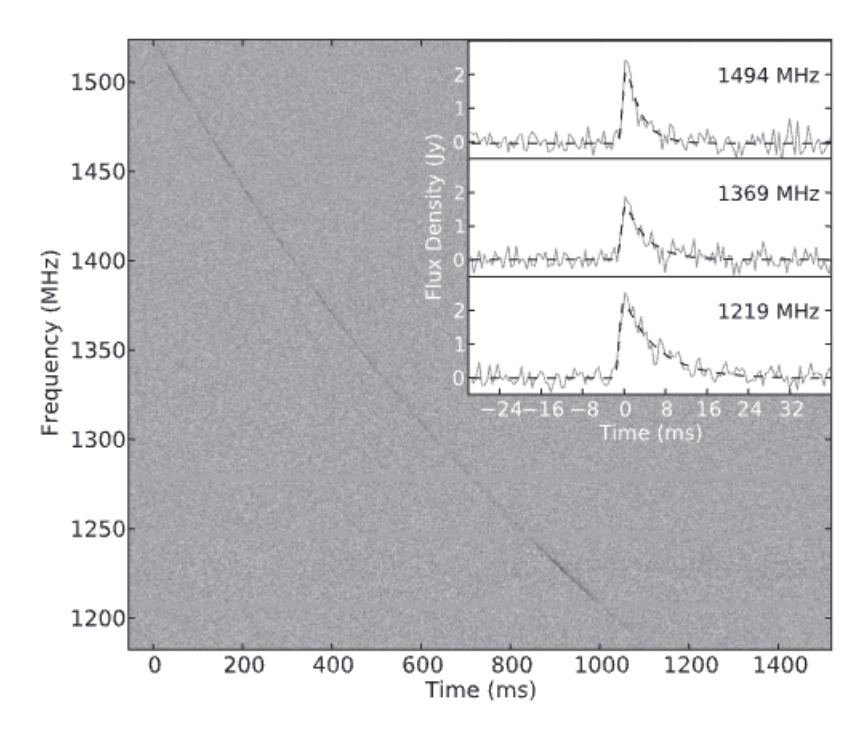


Figure 1.2: Figure taken from Thornton et al. (2013) showing the waterfall plot for FRB 110220. The inset shows the total-power signal for three 25-MHz wide subbands centered at different frequencies, showing the  $\nu$  dependence of the scattering tail.

from a nearer source.

While most repeating FRBs burst sporadically, CHIME/FRB Collaboration et al. (2020a) reported a 16.35 day periodicity in FRB 180916.J0158+65 and Rajwade et al. (2020) reported a possible 157 day periodicity in FRB 121102. These have led to progenitor model theories involving neutron stars in binaries and precessing isolated neutron stars (Zhang, 2020). The detection of repeating FRB-like bursts from a Galactic magnetar (CHIME/FRB Collaboration et al., 2020b) confirms magnetars as the origin of at least some FRBs. Whether all FRBs repeat and the apparent non-repeating nature of most FRBs is a result of selection effect is an open question and detailed population studies are required to understand the differences between these two possible classes of FRBs.

The repeating nature of a handful of FRBs has provided unprecedented insight into their local environments, host galaxies and possible progenitor models of FRBs. Follow-up observations of these FRBs have led to their sub-arcsecond localisation through Very Long Baseline Interferometry to very varied local environments, from one having extreme magneto-ionic activity (Michilli et al., 2018) to another in a globular cluster with old stellar populations (Kirsten et al., 2022). See Section 1.3.2 for a detailed description of some of the most notable FRB localisations.

### 1.3 Localisation of FRBs

Hundreds of FRBs have been discovered till now, most of them by the Canadian Hydrogen Intensity Mapping Experiment Fast Radio Burst Project (CHIME/FRB) (CHIME/FRB Collaboration et al., 2021). However, only about two dozen have been localised to their host galaxies. These localisations

have primarily come from the Very Long Baseline Interferometric facilities such as the Very Large Array (VLA), the Australian Square Kilometre Array Pathfinder (ASKAP), the Deep Synoptic Array (DSA-110), and the European VLBI Network (EVN). These localisations have informed us about the occurrence of FRBs in various dynamic environments giving clues about their origin, and also their usefulness as probes of the diffuse gas in the IGM. In this section I describe the basic principles of using VLBI to localise FRBs (Section 1.3.1), using localised FRBs to constrain progenitor models (Section 1.3.2) and FRBs as cosmological probes (Section 1.3.3).

#### 1.3.1 VLBI to localise FRBs

To localise an FRB to its host galaxy, an angular resolution of  $\lesssim 1$  arcsecond is required (Eftekhari and Berger, 2017). Depending on the redshift of the FRB, an even more precise resolution of a few milli-arcseconds is required to locate the local environment of the FRB within its host galaxy. Governed by the Rayleigh criterion, the angular resolution of diffraction limited systems goes as  $\sim \lambda/D$ , where  $\lambda$  is the wavelength of light and D is the diameter of the telescope. To do FRB science in the higher wavelength radio regime, this implies a telescope diameter of thousands of kilometres which is practically impossible to build. However, radio waves from FRBs (hereafter "signals") detected by smaller radio telescopes separated by thousands of kilometers can be combined digitally to behave similarly to signals detected by one large telescope. This technique is called Very Long Baseline Interferometry (VLBI). It involves observing the FRB simultaneously using all the telescopes in the VLBI array where the signals are amplified, digitized and sent to a common location over network links. The cross-correlations of signals from the telescopes reveal the position of the FRB on the sky. Middelberg and Bach (2008) gives a good introduction to VLBI.

Figure 1.3 shows a schematic diagram of how VLBI is done between two telescope sites A and B. The magnitude of the baseline vector **b** from A to B gives the distance between the telescopes. As a result of their physical separation, there is a time delay of  $\tau_{\rm geo}$ , referred to as the geometric delay, between the FRB signal arriving at the two sites. Equation 1.6 describes the baseline angle  $\theta$  which is a function of the RA ( $\alpha$ ) and DEC ( $\delta$ ) of the source and gives its localisation

$$\theta(\alpha, \delta) = \arccos\left(\frac{\tau_{\text{geo}}c}{b}\right) \tag{1.6}$$

where c is the speed of light and b is the baseline. Unfortunately, the observable in the VLBI experiment is not  $\tau_{\text{geo}}$ , but  $\tau_{\text{total}}$  which contains many delays

$$\tau_{\text{total}}(t,\nu) = \tau_{\text{geo}}(t,\theta) + \tau_{\text{clock}}(t) + \tau_{\text{iono}}(t,\nu) + \tau_{\text{inst}}(\nu) + \xi \tag{1.7}$$

where  $\tau_{\rm clock}$  is clock error,  $\tau_{\rm iono}$  is the dispersive delay due to ionosphere,  $\tau_{\rm inst}$  is the delay due to instrumental effects,  $\xi$  is noise error, t is the time of observation and  $\nu$  is frequency. The cross-correlation function  $\rho(\tau)$  (see Equation 2.13) between the signals observed at the two sites is a function of the delay  $\tau$  and is maximised when  $\tau = \tau_{\rm total}$ .  $\rho(\tau)$  is described in detail in Chapter 2. The key to localisation is

extracting  $\tau_{\text{geo}}$  from  $\tau_{\text{total}}$ . A detailed description of the other components of  $\tau_{\text{total}}$  and how to estimate them can be found in Chapter 4.

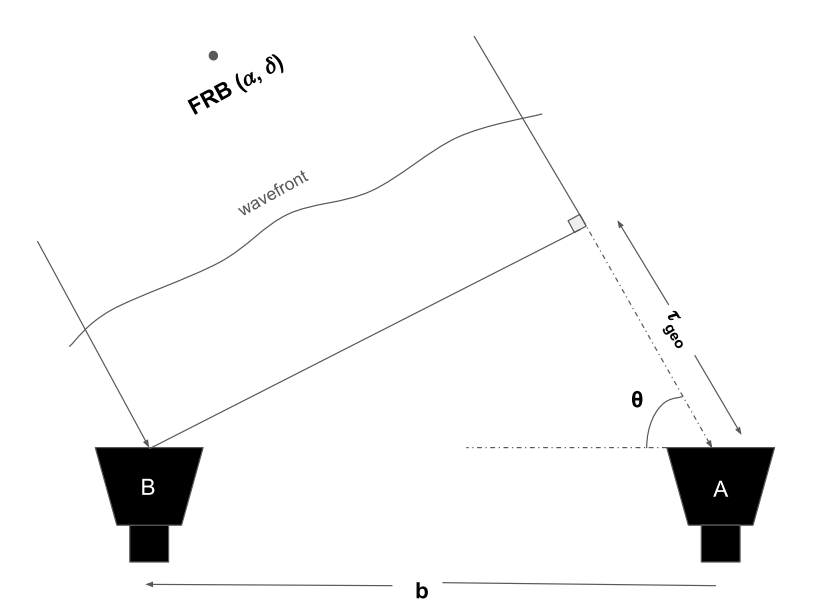


Figure 1.3: Schematic diagram showing two telescopes A and B observing an FRB located at (RA, DEC) =  $(\alpha, \delta)$ . The FRB signal arrives at A with a time delay of  $\tau_{\rm geo}$  due to its physical separation from B. The baseline angle  $\theta$  gives the localisation of the FRB and depends on  $\tau_{\rm geo}$  and the distance b between the two telescopes.

### 1.3.2 Constraining progenitor models

In this section, I discuss some of the most informative FRB localisations and how they have given us clues about FRB progenitors.

• Repeating FRBs with associated persistent radio counterparts: FRB 20121102 was the first repeating FRB to be identified (Spitler et al., 2016). Its extreme activity enabled its localisation to sub-arcsecond precision by the VLA (Chatterjee et al., 2017) which revealed the presence of a compact persistent radio source (PRS) co-located with the FRB localisation position. Tendulkar et al. (2017) used the Gemini North telescope to do optical imaging and spectroscopy at the localisation position and identified a low-metallicity, star-forming dwarf galaxy at a redshift of z = 0.193 which is the host-galaxy of the FRB. Marcote et al. (2017) observed the FRB and the PRS using the Arecibo telescope and the EVN and found that they are located within a linear separation of 40 parsec, hinting at a direct physical link between the two (see Figure 1.4). This localisation stood out among the other localisations of repeating and non-repeating FRBs until yet another repeating FRB, FRB 20190520B, was localised to a dwarf galaxy at z = 0.241 with a high-star formation rate (Niu et al., 2022). This highly-active FRB was identified by the Five-hundred meter Aperture Spherical radio Telescope (FAST) and localised using VLA which also led to the discovery of a compact PRS co-located with this FRB, thus making it strikingly similar to FRB 20121102.

Marcote et al. (2017) suggested two possible scenarios which can explain a compact PRS associated with a FRB. The FRB could be a young neutron star, such as a pulsar or magnetar and the PRS could be a supernova remanant (SNR) energised by the spin down of the rapidly rotating neutron star. Alternatively, the PRS could be a low-luminosity Active Galactic Nucleus (AGN) powered by a low-mass black hole with a low accretion rate and the bursts could be caused by plasma turbulence excited by relativistic jets of the AGN. Additionally, it is interesting that long-duration gamma-ray bursts (LGRBs) and super-luminous supernovae (SLSNe) also tend to occur to in low-metallicity dwarf galaxies with high star-formation rates suggesting their possible connection with the above-mentioned repeating FRBs (Tendulkar et al., 2017).

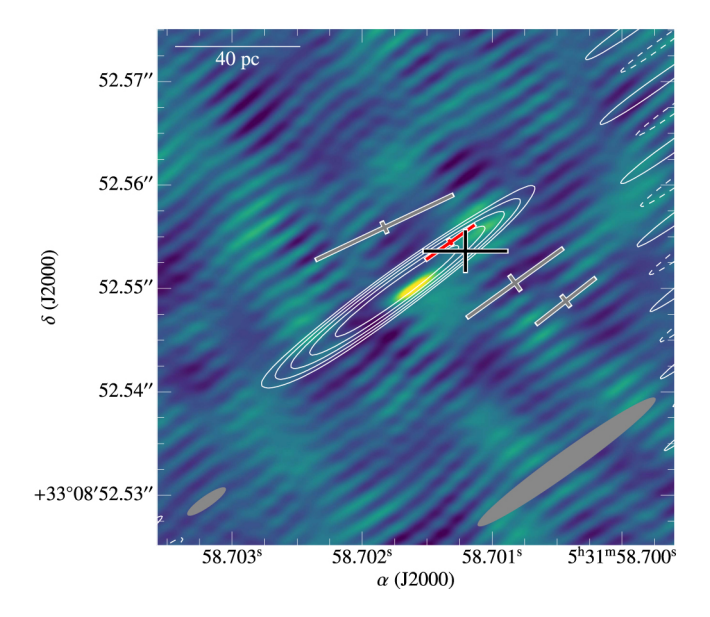


Figure 1.4: A high-resolution EVN image of FRB 121102 at a frequency of 1.7 GHz taken from Marcote et al. (2017). The bright spot within the white contours show the persistent radio source. The red cross shows the localisation position of the brightest FRB burst, the grey crosses show the position of other three observed burst, the black corss shows the position obtained by averaging all four bursts.

Yet another repeating FRB, FRB 20201124A (Lanman et al., 2022) was associated with a radio continuum source (Ricci et al., 2021). This FRB was localised to a massive star-forming galaxy at z=0.098 (Nimmo et al., 2022b; Day et al., 2021). However, Piro et al. (2021) showed that unlike the previous two cases, the radio continuum source in this case was associated with star-formation such that the FRB source was located at the centre of the star-forming region. The host galaxy and local environment properties pointed towards a magnetar formed via the core-collapse of a massive star as the progenitor for this FRB.

• A repeating FRB in a Globular Cluster: Bhardwaj et al. (2021) identified a repeating FRB with the lowest recorded DM of 87.82 pc cm<sup>-3</sup> in the CHIME/FRB data, having a maximum Milky Way DM contribution of 40 pc cm<sup>-3</sup> along the line of sight. The authors ruled out a Galactic or Milky Way halo origin for this FRB. The relatively coarse 14 sq. arcmin localisation of this nearby FRB was 20 kiloparsec from the centre of a grand-design spiral Galaxy called M81 (see Figure 1.5).

This is a huge offset from the galaxy centre when compared to the other localised FRBs and added more speculations to the nature and origin of FRBs. Kirsten et al. (2022) later used EVN to localise this FRB, henceforth referred to as M81R, to a globular cluster associated with M81 and did not detect a persistent radio counterpart. Globular clusters have old stellar populations which makes it difficult to invoke progenitor models involving magnetars formed via core-collapse supernova. Since globular clusters are known to host short-orbital period binaries, the FRB progenitor could be a magnetar formed via accretion-induced collapse of a white dwarf or via merger-induced collapse of a white dwarf-white dwarf, neutron star-white dwarf or neutron star-neutron star binary.

In addition to hinting at different progenitor channels for FRBs, this FRB is also particularly interesting because it shows the usefulness of nearby low-DM FRBs. A low-DM FRB localised to a near-by Galaxy and followed up by high-resolution optical telescopes such as the Hubble Space Telescope to reveal the source of the FRB could solve the mystery of FRB progenitors.

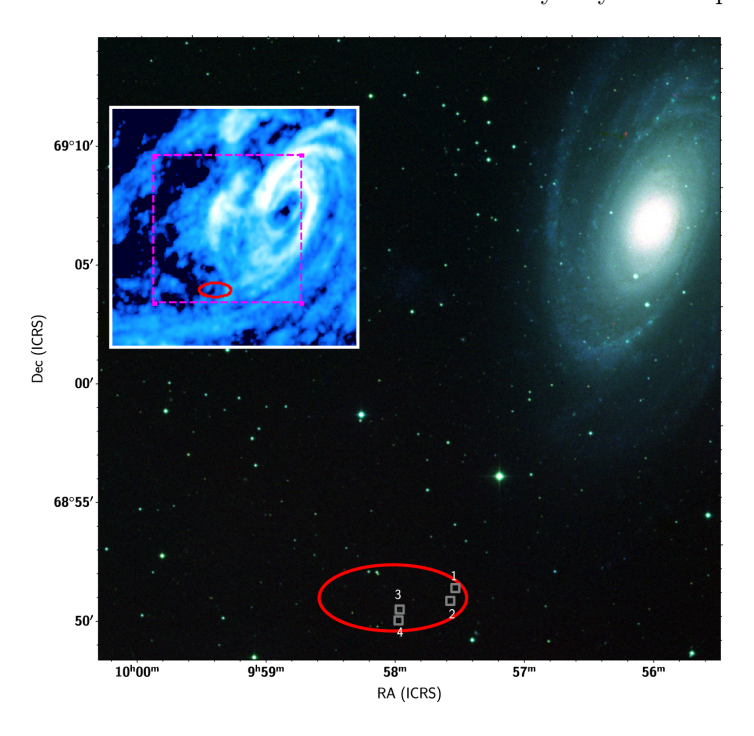


Figure 1.5: Figure showing the localisation region of M81R, taken from Bhardwaj et al. (2021). This Digital Sky Survey (DSS) image shows the spiral galaxy M81 with the red ellipse representing the 90% confidence localisation region. 1, 2, 3 and 4 are an M81 H II region, an X-ray source, an M81 globular cluster [PR95] 30244, and a point radio source respectively. EVN later localised M81R to [PR95] 30244. The inset shows the 21 cm view of the M81 circumgalactic medium with the dashed box representing the DSS image field of view.

• A periodic repeater in a spiral galaxy: FRB 180916.J0158+65, henceforth referred to as R3, was the third repeating FRB identified by CHIME/FRB. It is by far the most prolific FRB source as it exhibits a periodicity of 16.35 days (CHIME/FRB Collaboration et al., 2020a) favouring binary progenitor models. Nimmo et al. (2022a) also found that the burst durations for R3 range from microseconds to milliseconds, placing tight constraints on the size of the emitting region. EVN localised R3 to an accuracy of 2.3 milliarcsecond to a massive spiral galaxy at a redshift of 0.0337 and did not find an associated PRS (Marcote et al., 2020). More interestingly, the authors found

the FRB located at the apex of a V-shaped star-forming clump. Tendulkar et al. (2021) later used the Hubble Space telescope to do high resolution optical and infrared imaging of the localisation position and found that the FRB is offset by 250 pc from the nearest knot of active star formation in the V-shaped feature (see Figure 1.6). This disfavours progenitor models involving young magnetars which are found close to their star-forming birth sites. Instead, this positional offset, periodicity and constraints on emitting region size make a binary system involving a neutron star and a late O-type or B-type star a possible progenitor. In such a system, the interactions between the neutron star's magnetic field and ionised wind of the massive companion would produce coherent radio bursts. Like M81R, the R3 localisation is also an example of how exceptionally high-angular resolution astrometry of FRBs can reveal unusual local environments and open up possibilities of different kinds of progenitors.

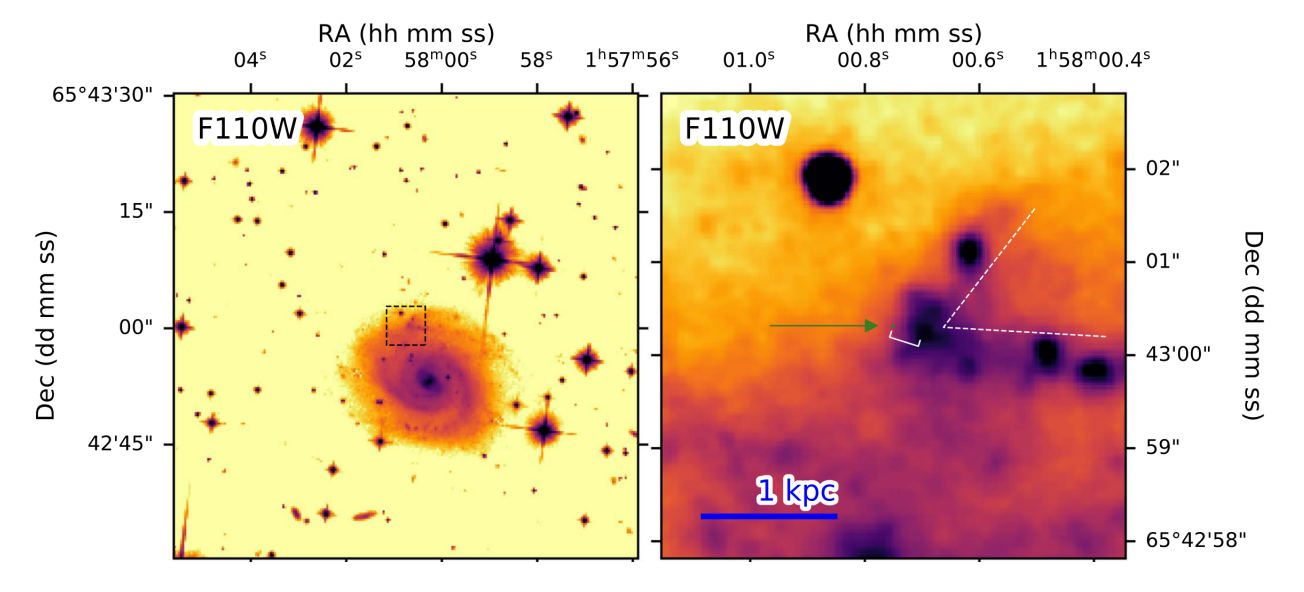


Figure 1.6: Figure showing the Hubble Space Telescope observation of the localisation region of R3, taken from Tendulkar et al. (2021). The left image shows the spiral host galaxy and its surroundings. The right image shows the localisation region in a green ellipse pointed by a green arrow, which is 250 pc offset from the closest peak of star formation in the V-shaped clump.

• Localisation of non-repeating FRBs: In the past half-decade, ASKAP has emerged as the leading instrument to localise non-repeating FRBs (Bannister et al., 2019), followed by DSA-110 (Ravi et al., 2019). These are radio interferometers with multiple dishes which detect FRBs by searching the data for dispersed signals (see Section 2.1.2). The sky-location of the burst is then obtained from images formed using the phase and amplitude information of the FRB voltage data. Since (apparently) non-repeating FRBs are known to occur at a much higher rate than repeating FRBs, the ability to localise them to ~arcsecond precision has opened up a huge sample space of host galaxy (HG) and local environment (LE) properties to study. Various works have carried out detailed analysis to study the colour, star formation rate (SFR), and masses of the HG and positions of LE within the HG and compared them with other transients. These studies have not found a particular type of HG or LE where FRBs preferentially reside, but rather found that HG exhibit a broad, continuous range of colour, stellar mass, star formation rates, ages and luminosities

(Heintz et al., 2020). Mannings et al. (2021) studied the UV and IR spectrum of the HG and found that 5/8 HGs have spiral arms. The FRBs localised to such galaxies reside within the spiral arms but not in the brightest star-forming regions hinting at a spatial drift from the progenitor's birth location to its explosion site. Bhandari et al. (2022) studied the largest sample of localised FRBs and found that most FRBs occur in moderately star forming galaxies. Thus far, no significant differences have been seen between the host properties of repeating and non-repeating FRBs. The LE of FRBs are not consistent with the positions of globular clusters found in late-type spiral and early-type elliptical galaxies, making M81R an exception rather than a rule. All of these studies report the HG and LE properties of FRB 121102 and FRB 20190520B as an outlier, and rule out LGRBs and SLSNe as possible progenitors for most FRBs. Instead, the positions of LE within HG are the most consistent with short gamma-ray-bursts (SGRBs) and core-collapse supernova (CC-SNe). These point to magnetars formed via binary neutron-star mergers as more probable progenitors. These studies highlight the importance of localising a large number of FRBs to their HG which makes population studies and comparison to other transients possible.

### 1.3.3 Localised FRBs as cosmological probes

In the z < 2 Universe, baryons in the stars, the interstellar medium, the galaxy clusters and the intergalactic photo-ionized gas account for  $\lesssim$ 50% of the total (Nicastro et al., 2008). The remaining baryons are thought to reside in the circum-galactic medium (CGM) surrounding galaxies and the intergalactic medium (IGM) between galaxies in the form of shock-heated, diffused and ionised gas. The diffuse nature of this gas makes it difficult to directly observe it, thus giving rise to the "missing" baryon problem. As stated in Equation 1.4, the DM of FRBs also constitute the DM due to the ionised gas in the IGM, making FRBs excellent tracers of the baryons in the IGM. For the standard model of cosmology of a flat universe with dark matter and dark energy, the average value of DM  $_{\rm IGM}$  to a redshift  $_{\rm ZFRB}$  is:

$$\langle \mathrm{DM}_{\mathrm{IGM}} \rangle = \int_0^{\mathrm{z}_{\mathrm{FRB}}} \frac{c\bar{n}_e(z)dz}{H_0(1+z)^2 \sqrt{\Omega_m (1+z)^3 + \Omega_\Lambda}}$$
(1.8)

$$\bar{n}_e = f_d \rho_b(z) m_p^{-1} (1 - Y_{\text{He}}/2)$$
 (1.9)

where  $m_p$  is the mass of proton,  $Y_{He}=0.25$  is the mass fraction of doubly ionoised helium,  $f_d(z)$  is the fraction of cosmic baryons in diffuse ionised state,  $\rho_b(z)=\Omega_b\rho_{c,0}(1+z)^3$ ,  $\Omega_m$  and  $\Omega_\Lambda$  are the dark matter and dark energy densities today,  $\rho_{c,0}=3H_0^2/8\pi G$  and  $H_0$  is the Hubble's constant. Figure 1.7 taken from Niu et al. (2022) shows this theoretical DM-z relation plotted with the extragalactic DM and redshifts of 15 localised FRBs. Contributions to the extragalactic DM from the local environments and host galaxies of some FRBs cause a deviation of the observed value from the theoretical expectation, but in general the FRBs clearly track the expected relation. Macquart et al. (2020) first showed that the localised FRBs follow Equation 1.8, now known as the Macquart relation, and thus the "missing" baryons are in the IGM.

Additionally, when a large sample of redshifts are available from localised FRBs, the variance in the

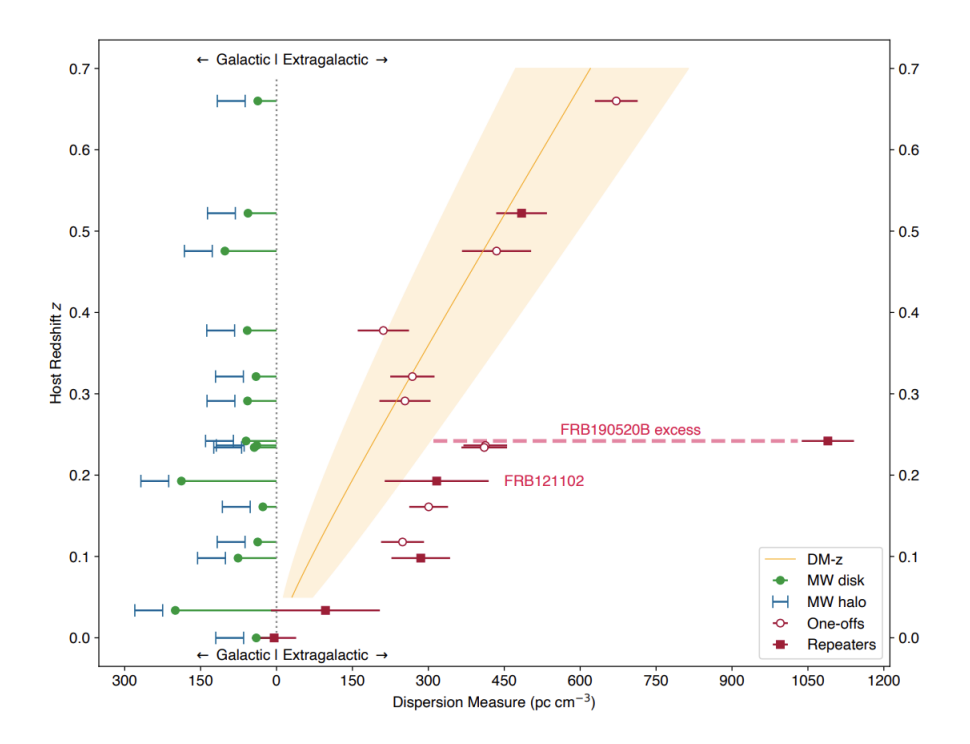


Figure 1.7: Plot taken from Niu et al. (2022) showing the DM-z relation with the extragalactic DM and z of 15 localised FRBs. The Milky Way disk DM is estimated using the NE2001 model with 20% uncertainties, the Milky Way halo DM is taken to be 25-80 pc cm<sup>-3</sup>. The yellow line and the shaded region represent the theoretical DM-z relation and the 68% confidence interval respectively. The extragalactic DMs are shifted right from the expected values due to DM contributions from the host galaxy and local environments of the FRB, with FRB 190520B being a clear outlier.

observed DM-z relation will give important clues about how baryonic matter is distributed in the halos of the galaxies encountered along the line of sight (Bhandari and Flynn, 2021).

It is clear that a large sample of localised FRBs are essential to unlock the mystery of their origin and to use them for studies of the CGM and IGM. While facilities like ASKAP and DSA-110 have made significant leaps in FRB localisations, the number of FRBs they detect is limited by their field of view. CHIME is a novel transit telescope with a 200 square degree field of view and observes the entire northern sky everyday. This has enabled CHIME to detect a large sample of FRBs but with poor localisations. The CHIME/FRB Outriggers are three smaller CHIME-like telescopes which will form a VLBI network with CHIME and localise FRBs to ~50 milli-arcsecond precision. In Chapter 2, I describe CHIME, CHIME Outriggers and our algorithms to localise FRBs.

For calibrating the VLBI network, we plan to employ a novel approach of using pulsars spread over the entire sky as calibrators. The implementation of this approach requires the real-time beamforming of pulsars every second to track a pulsar calibrator as it transits through the sky. In Chapter 3, I describe the upgrades I made to the rudimentary realtime beamformer to meet these requirements.

KKO, the first CHIME/FRB Outrigger, saw first light in June 2022, and has been in commissioning ever since. With a 66-km line of sight distance to CHIME, it can provide a localisation accuracy of 1 arcsecond. As the pathfinder for the Outriggers, KKO enabled the development and testing of software pipelines aimed at FRB localisation. In Chapter 4, I describe the pipelines I set up to acquire FRB data

at the Outriggers, and an analysis I carried out to obtain the accuracy and estimated errors of our VLBI							
calibration techniques.							

### Chapter 2

# VLBI with CHIME and the Outriggers

In this Chapter, I describe CHIME, its FRB search and localisation capability and the need to build the CHIME/FRB Outriggers for better localisation precision. I also describe in detail the VLBI algorithms we will use to localise FRBs with milli-arcsecond precision using CHIME and the Outriggers.

### 2.1 Detecting FRBs with CHIME

#### 2.1.1 Overview of CHIME

The Canadian Hydrogen Intensity Mapping Experiment (CHIME) is a transit radio telescope located on the grounds of the Dominion Radio Astrophysical Observatory (DRAO) near Penticton, British Columbia. CHIME was designed to detect the Baryon Acoustic Oscillation (BAO) by intensity mapping the 21-cm hyperfine emission of neutral hydrogen from redshift z=0.8-2.5 where dark energy began to exert its influence. This will enable a better understanding of the expansion history of the Universe (CHIME Collaboration, 2022). This goal motivates the design features of the telescope such as a large collecting area of 8000 m<sup>2</sup> and a powerful correlator which together enable fast mapping speeds to overcome the sample variance, and an observing frequency band of 400 – 800 MHz. CHIME consists of four 100 m  $\times$  20 m cylindrical paraboloidal reflectors each having 256 dual polarization cloverleaf feeds suspended along the focal line, providing 2048 signal paths and a field of view (FoV)  $\gtrsim$  200 deg<sup>2</sup>. Figure 2.1 shows a photo of CHIME and Table 2.1 gives a brief summary of its properties.

The focal line of the cylinders consists of the feeds and low-noise amplifiers which receive and amplify the signal which is then passed over coaxial cables to the receiver huts. CHIME has two Radio Frequency Inteferfence (RFI) shielded receiver huts, each of which processes 1024 signals from two cylinders and is located between them. In the receiver huts, the signal is further amplified in a stage that includes a bandpass filter before passing through the F-engine electronics. The F-engine consists of 128 "ICE" motherboards (Bandura et al., 2016) each of which digitises 16 analog signals with 8-bit accuracy. Then, the 400 MHz bandwidth of each digitised timestream is channelised into 1024 frequency channels, each 390 kHz wide with a sampling cadence of 2.56  $\mu$ s, using a polyphase filter bank. A gain and phase offset are applied to each frequency channel and the data are rounded to a 4+4 bit accuracy. At this point, each



Figure 2.1: Photo of CHIME taken from CHIME/FRB Collaboration (2018) showing the four cylindrical reflectors and the shipping containers on the right which house the X-engine and the FRB search backend.

Collecting area	$8000 \text{ m}^2$
Longitude	$119^{\circ}37'25\ 25\ West$
Latitude	$49^{\circ}19'14\ 52\ North$
Frequency range	400-800  MHz
Polarization	orthogonal linear
E-W FoV	$2.5^{\circ}$ – $1.3^{\circ}$
N-S FOV	$\sim 110^{\circ}$
Focal ratio	0.25
Receiver noise temperature	50 K
Number of beams	1024
Beam width (FWHM)	40'-20'
FRB search time resolution	0.983  ms
FRB search frequency resolution	$24.4~\mathrm{kHz}$
Source transit duration	Equator: 10–5 minutes
	45°: 14–7 minutes
	North celestial pole: 24 hr

Table 2.1: Table taken from CHIME/FRB Collaboration (2018) describing the key properties of CHIME.

data stream consists of data for all frequency channels for a single feed. The next stage is the "corner turn" stage in which the frequency channelised signals from each of the ICE boards are rearranged so that signals from all feeds belonging to a single frequency channel are assembled at a single GPU node in the X-engine. The X-engine consists of 256 GPUs having 4 nodes each, where one node processes data from one of the 1024 frequency channels. This is called baseband data and are saved in a 30-s ring buffer which can be saved to disk upon an FRB detection. The GPU nodes correlate signals from each pair of feeds to form  $N^2$  (where N refers to the 2048 signals) time-averaged visibilities which can be manipulated offline for BAO mapping.

### 2.1.2 The CHIME/FRB Instrument

The combination of a large field-of-view (FoV), wide bandwidth and powerful correlator also makes CHIME an excellent FRB detector. This led to the CHIME/FRB project where upgrades were made to

the original X-engine correlator and a dedicated FRB search engine called the CHIME/FRB instrument was installed at CHIME. This consists of five "Levels", named L0–L4 which are described below.

• L0: L0 runs in the X-engine correlator where 256 beams are formed in the North-South (N-S) direction via a Fast Fourier Transform (FFT) algorithm (Ng et al., 2017). These N-S beams are tiled across a range of angles evenly spaced in the  $\sin\theta$  space where  $\theta$  is the zenith angle. Four beams are formed in the East-West direction which gives a total of 1024 static beams tiled across the entire FoV of CHIME.

To detect an FRB in the CHIME observing band, the incoherently dedispersed intensity data are searched for an FRB signal. As explained in Section 1.1.1, DM causes the FRB signal in a frequency channel centered at a frequency  $\nu$  to be shifted in time from the reference frequency  $\nu_{\rm ref} = 800$  MHz by an amount:

$$t_{\rm DM}(\nu) = k_{\rm DM} DM \left( \frac{1}{\nu^2} - \frac{1}{\nu_{\rm ref}^2} \right)$$
 (2.1)

Incoherent dedispersion involves reversing this time shift so that the data are aligned in time across all frequency channels. This is done in the next stage, however, to prevent a significant residual dispersive smearing within a frequency channel, it is important to have narrow frequency channels, especially at CHIME's low observing frequencies. Moreover, since FRBs are millisecond transients, a comparable time resolution is required. The CHIME/FRB project searches for FRBs using a 24.4 kHz frequency resolution and a 1-ms time resolution. This requires a trade-off in the original time resolution of 2.56- $\mu$ s offered by CHIME to achieve a finer frequency resolution. This is achieved in the L0 stage by Fourier-transforming 128 successive 2.56- $\mu$ s voltage samples, squaring the magnitude of this spectrum and downsampling in frequency by a factor of 8, averaging three successive downsampled transforms and adding the two polarisations to produce a Stokes-I data stream. This intensity data are buffered in a 20-s ring buffer which can be stored to disk upon an detection. These 1024 total intensity beams with a 0.983-s time resolution and 16348 frequency channels are searched by L1 for a FRB signal.

• L1: L1 has 128 nodes, each of which processes intensity data from 8 beams. The first step in L1 requires rearranging the data from the 256 X-engine GPUs each processing 4 frequency channels so that data for all frequency channels for 8 beams are consolidated in one L1 node. After that, L1 performs the most computationally expensive task of "dedispersion transform" where intensity data are converted from time and frequency space to time and DM space. This is implemented using a tree-algorithm called bonsai which outputs a 5D grid of detection signal-to-noise ratios (SNRs) based on an input search grid of DM, arrival time, spectral index, scattering time (explained in Section 1.1.2), and intrinsic pulse width. The search grid has a maximum DM of 13,000 pc cm<sup>-3</sup> and a maximum pulse width of 100 ms. A SNR threshold of 10σ is set to identify candidate events. A "L1 Header" is created for the candidates which holds information such as the DM, time, RFI rating, SNR value and a sky-position based on the beam in which the event was detected. The fact that we can get the latency of this algorithm down to ~ 2-3 s is crucial since intensity data

are buffered only for 20 s in L0 and baseband data are buffered only for 30 s in the X-engine.

• L2/L3: Once L1 headers reporting detections are created for all beams for a data block, they are collected at a single endpoint and the existence of multi-beam events is searched in the L2 stage. This is done by a DBSCAN algorithm which searches for clusters in the DM, time and sky position space. After a cluster having one or more beams is detected, a L2 header is created from one or more L1 headers from the grouping. Although several levels of RFI excision are performed in the previous stages, RFI can still seep in and the next step in L2 is to classify the event as RFI or astrophysical. This is done using the fact that RFI is near-field and will have a broader intensity distribution in the beams as opposed to the sharply focused intensity distribution pattern for the far-field astrophysical events. For the events which are classified as astrophysical, a refined position is estimated based on the SNRs from each beam to what is expected from a beam model. The refined position, SNR and pulse width are used to estimate the radio flux of the event.

L3 classifies the events into known/unknown and Galactic/extragalactic and based on that determines what action to take on the event. The refined position and DM of the event are compared to the positions and DMs in a database consisting of known radio transients. A probability of association with nearby sources is calculated and true associations are decided based on a threshold determined from simulated events. For events not classified as known sources, the DM<sub>MW,ISM</sub> is estimated based on models of Galactic free electron density (Cordes and Lazio, 2002; Yao et al., 2017). If the DM exceeds the predicted DM<sub>MW,ISM</sub> by  $5\sigma$ , it is classified as extragalactic. If the DM exceeds the predicted DM<sub>MW,ISM</sub> by  $2\sigma$ – $5\sigma$ , it is classified as ambiguous. Otherwise, it is classified as Galactic. Based on this classification, L3 assigns actions such as saving intensity data for all unknown extragalactic events having a SNR > 8 and saving baseband data for all unknown extragalactic event having a SNR > 12.

• L4: L4 assigns event numbers to all events which are sent past the L1 stage including RFI and known/unknown Galactic/extragalactic events and saves their header information and associated analysis products in the CHIME/FRB archive. L4 also implements the actions assigned to the events by L3 including sending "triggers" to save intensity and baseband data. As described in Section 4.2.1, L4 also sends triggers to save FRB baseband data at the Outrigger sites and plays the crucial role of ensuring simultaneous acquisition of data at CHIME and Outriggers which can be cross-correlated and localised using VLBI.

### 2.2 Baseband data

As described in Section 2.1.1, baseband data are the voltage data with a time resolution of 2.56  $\mu$ s and frequency resolution of 390 kHz which are buffered for 30 s in the X-engine. While the intensity data are used for searching for an FRB signal, it is the complex-valued baseband data which have the phase information used for astrometric localisation of FRBs. In order to economise disk space, only 100 ms of baseband data from the 30 s ring buffer are stored to disk upon an FRB detection. The format of the

data consists of an array of M=1024 frequency channels, N time bins of size 2.56- $\mu$ s, each of which is known as a "frame", and the X (CHIME E-W) and Y (CHIME N-S) polarisations. This array of baseband data for the X and Y polarisation will be henceforth referred to as  $\mathbf{V}_{\rm X}[{\rm m, n}]$  and  $\mathbf{V}_{\rm Y}[{\rm m, n}]$  respectively where m ranges from 0 to M-1 and n ranges from 0 to N-1.  ${\rm m}=0$  has a centre frequency of 800 MHz and  ${\rm m}=1023$  has a centre frequency of 400.390625 MHz. Each frame has a GPS time stamp associated with it which marks the beginning of the 2.56- $\mu$ s window. The data are saved in a way which traces the dispersion sweep of the FRB, thus each frequency channel data will have a different start time (corresponding to the frame  ${\rm n}=0$ ) with the 800 MHz channel having the earliest start time.

The baseband data allow interferometric localisation of the FRB at CHIME. This process involves offline digital beamforming by aligning phases of the data in the M channels and N frames towards a skylocation. Beamforming is done on a grid of sky positions centered at the intensity localisation of the FRB output by L2, and the position giving the maximum intensity of the beamformed pulse is taken to be the baseband localisation position of the FRB. The beamformed data towards this position are stored in a HDF5 file called the "singlebeam" file. This pipeline is described in detail in Michilli et al. (2021). The interferometric capabilities of CHIME allow a localisation angular resolution which scales as:

$$\theta_{\rm res} = \frac{\sqrt{6}}{\pi} \frac{\lambda}{\rm D} \frac{1}{\rm SNR} \frac{1}{\cos(\theta_z)}$$
 (2.2)

where  $\theta_z$  is the zenith angle of the FRB,  $\lambda$  is the observing wavelength, D is the diameter of the telescope. This is better than the Rayleigh criterion resolution of  $\sim \lambda/D$ , and a higher SNR FRB yields a better localisation (Masui et al., 2017). For a typical FRB, this would yield a CHIME localisation uncertainty of  $\sim$ 1 arcminute (Michilli et al., 2021) which can only allow host-galaxy identification for nearby low-DM FRBs.

### 2.3 CHIME/FRB Outriggers

To associate an FRB with its host galaxy, a localisation precision of ~1 arcsecond is required (Eftekhari and Berger, 2017). To identify the local region of an FRB within the host galaxy, a localisation precision of tens of milliarcseconds is required. Baseband localisation with CHIME alone does not provide this accuracy. Consequently, CHIME/FRB is building three outrigger telescopes to form a VLBI array with CHIME and localise FRBs to ~50 milli-arcsecond precision. KKO, the first outrigger, is built in Princeton, British Columbia providing a 66-km baseline and ~1 arcsecond localisation accuracy. Chapter 4 describes the commissioning of KKO and VLBI accuracy tests for the CHIME-KKO baseline. GBO, the second outrigger, is built in Green Bank, West Virginia, USA providing a ~3300 km baseline and ~50 milliarcsecond localisation accuracy. It is currently in the commissioning phase. HCO, the third outrigger, will be built in Hat Creek, California, USA, providing a ~1300 km baseline and ~150 milliarcsecond localisation accuracy with CHIME. Figure 2.2 shows the location of CHIME and the Outriggers and the baselines they provide. The orthogonal CHIME-GBO and CHIME-HCO baselines will provide a sub-arcsecond localisation in two-dimensions, to easily pinpoint the local environment and

host galaxy of the FRB.

All outriggers consist of one cylindrical paraboloidal reflector and optical, analog and digital designs



Figure 2.2: Map of North America showing the locations of CHIME and the Outriggers and the baselines they provide.

similar to CHIME. KKO has 64 dual polarisation cloverleaf antennas, while GBO and HCO have 128 dual polarisation cloverleaf antennas. The cylinders are rolled and rotated to see the same sky as CHIME, which allows an FRB detected at CHIME to also be seen by the Outriggers. The signal path from the antennas involves a F-X engine, similar to CHIME's signal path described in Section 2.1.1. However, the Outriggers do not have an FRB search engine. They buffer baseband data in a 30-s ring buffer in the X-engine, and save 100 ms of baseband data to disk upon an FRB trigger sent by CHIME's L4 stage. These simultaneous acquisition of FRB baseband data are later cross-correlated to obtain a localisation using algorithms described in the next section.

### 2.4 VLBI Calibration and Localisation algorithms

As described in Section 1.3.1, cross-correlation between FRB baseband data from two interferometers gives a delay  $\tau_{\text{total}}$  which has many components. The goal of VLBI calibration is to cancel out or fit-out all the other components except for  $\tau_{\text{geo}}$ , which can be used to constrain the region of the sky from which the FRB signal came. The steps leading up from simultaneous acquisition of baseband data at CHIME and the Outriggers to localisation of the FRB are detailed in this section. These algorithms are developed by and implemented in Leung et al. (2021) and Cassanelli et al. (2022).

#### 2.4.1 Cross-Correlation

As a first step, the FRB baseband data at CHIME are localised using the baseband localisation pipeline described in Section 2.2, giving an initial coarse estimate of its position ( $\alpha_0$ ,  $\delta_0$ ). The data at CHIME and the Outriggers are beamformed to this position and incoherently dedispersed using the DM of the

FRB, giving the beamformed voltage data  $\mathbf{V}_{P_C}[m,n]$  and  $\mathbf{V}_{P_O}[m,n]$ , where P represents polarisation, C and O represent CHIME and a Outrigger telescope respectively, m represents frequency channels and n represents time frames.  $P_C$  and  $P_O$  can take values 0 and 1, which represent the E-W and N-S polarisations respectively. Then, the following steps are implemented to form the cross-correlation visibility  $\mathcal{V}_{P_CP_O}[m,n]$ :

- 1. The time of arrival (TOA) of the FRB signal at CHIME is identified as the time frame at which the power |V<sub>PC</sub>[m,n]|<sup>2</sup> of the baseband data peaks. The pulse width t<sub>w</sub> is also calculated by finding the times at either side of the TOA at which the power drops by less than 20%. Using the TOA, the locations of CHIME and the Outrigger and the initial localisation (α<sub>0</sub>, δ<sub>0</sub>), a routine called difxcalc11 (Gordon et al., 2016) can calculate the initial estimate of the geometric delay τ<sub>geo0</sub>[n] between the signal arriving at the two sites. τ<sub>geo0</sub> is a function of the time frame n since the position of the FRB source on the sky will vary with time due to Earth's rotation. The time duration of our baseband data (~ 100 ms) ensures that this variation is sub-frame, that is, less than the frame size of 2.56 μs.
- 2.  $\tau_{\text{geo}_0}[n]$  is split into integer number of time frames  $n_{\text{shift}}$  and the remaining sub-integer delay:

$$n_{\text{shift}} = \left| \frac{\tau_{\text{geo}_0}[n]}{2.56 \ \mu s} \right| \tag{2.3}$$

$$\tau_{\rm geo_0}^{\rm sub-int}[{\bf n}] = \tau_{\rm geo_0}[{\bf n}] - {\bf n}_{\rm shift} \times 2.56~\mu s \tag{2.4}$$

where  $\lfloor \rfloor$  denotes a floor function. The integer delay is removed by "rolling" or shifting  $\mathbf{V}_{P_O}[m,n]$  by  $n_{shift}$  number of frames. This essentially takes  $n_{shift}$  frames from the start and puts them towards the end of the data. The sub-integer delay is removed by applying a phase-shift  $\phi_{geo_0}^{sub-int}[m,n]$ . Altogether:

$$\widetilde{\mathbf{V}}_{\mathrm{P_{\mathrm{O}}}}[\mathrm{m,n}] = \mathbf{V}_{\mathrm{P_{\mathrm{O}}}}[\mathrm{m,n-n_{\mathrm{shift}}}] \; \mathrm{exp}[\; -\mathrm{i} \; \phi_{\mathrm{geo_{0}}}^{\mathrm{sub\text{-}int}} \; ] \tag{2.5}$$

$$\phi_{\rm geo_0}^{\rm sub-int}[m,n] = 2\pi \ \tau_{\rm geo_0}^{\rm sub-int}[n] \ \nu[m] \eqno(2.6)$$

where  $\nu[m]$  is the centre of the frequency channel m. After this, the remaining geometric delay  $\tilde{\tau}_{geo}$  between the two baseband datasets is sub-frame and because of the difference between the true location of the FRB and its initial coarse location ( $\alpha_0$ ,  $\delta_0$ ) estimated by the baseband pipeline:

$$\widetilde{\tau}_{\text{geo}} = \tau_{\text{geo}} - \tau_{\text{geo}_0} \tag{2.7}$$

3.  $\widetilde{\mathbf{V}}_{\mathrm{Po}}$  and  $\mathbf{V}_{\mathrm{Pc}}$  are incoherently dedispersed signals. The next step is to coherently dedisperse the signal at each telescope site to remove intra-channel dispersion smearing. Lorimer and Kramer (2012) describes the coherent dedispersion algorithm.

4. The time-integrated cross-correlated visibility  $\langle \mathcal{V}_{P_CP_O} \rangle_{t_w}[m]$  is then formed:

$$\langle \mathcal{V}_{P_C P_O} \rangle_{t_w}[m] = \sum_{n=toa-t_w/2}^{n=toa+t_w/2} \mathbf{V}_{P_C}[m,n] \ \widetilde{\mathbf{V}}_{P_O}[m,n]^*$$
(2.8)

where \* represents complex conjugate. The time-integration over the pulse width  $t_w$  cancels out random phase errors. When doing this, we are safely assuming that the delay  $\tilde{\tau}_{geo}$  is constant for the time period  $t_w$ , since  $t_w$  is only a few milliseconds during which we do not expect the source position on the sky to change significantly.

A metric we use to evaluate the success of a cross-correlation is the behaviour of the integrated visibility as a function of "lag". Lag is the residual delay in  $\langle \mathcal{V}_{P_CP_O} \rangle_{t_w}[m]$  expressed in units of number of frames. In addition to the integrated visibility obtained by rolling  $\mathbf{V}_{P_O}[m,n]$  by  $n_{shift}$  number of frames, we also obtain the integrated visibility by rolling  $\mathbf{V}_{P_O}[m,n]$  by a range of values from  $n_{shift}$  - 100 to  $n_{shift}$  + 100, which gives the lag l varying from -100 to 100. The other delay contributions to  $\tau_{total}$ , namely,  $\tau_{clock}$ ,  $\tau_{iono}$ ,  $\tau_{inst}$ , and  $\xi$  (see Equation 1.7) are expected to be sub-frame. Thus, if we have estimated  $\tilde{\tau}_{geo}$  correctly and if the systematic errors are also sub-frame, then the amplitude of  $\langle \mathcal{V}_{P_CP_O} \rangle_{t_w}[m,l]$  should peak at l=0, and the integrated visibility for  $l\neq 0$  should just be noise. The cross-correlation power  $P_{xcorr}[l]$  can be obtained by averaging the amplitude of  $\langle \mathcal{V}_{P_CP_O} \rangle_{t_w}[m,l]$  over m. The SNR of cross-correlation can be obtained by taking a ratio of the maximum and the median absolute deviation (MAD) of  $P_{xcorr}[l]$ . For a successful cross-correlation,  $P_{xcorr}[l]$  should peak at l=0. Additionally, we have opted for a SNR threshold of 20 for a cross-correlation to be considered successful, since we have observed that this threshold ensures acceptable noise in the phase of the visibility.

Figure 2.3 shows the amplitude of the  $\langle \mathcal{V}_{P_CP_O} \rangle_{t_w}[m,l]$  for a Crab pulsar cross-correlation for the CHIME–KKO baseline. The four plots are for the four pairs of  $P_CxP_O$ , where both  $P_C$  and  $P_O$  take values 0 and 1, and x represents cross-correlation between them. Figure 2.4 shows the corresponding  $P_{xcorr}[l]$  and SNR. The RFI contaminated channels are masked out. As can be seen, this is a successful cross-correlation. There is a weak cross-correlation between the 0x1 and 1x0 polarisation pairs which can be attributed to the intrinsic linear polarisation of the Crab pulsar and leakage between the two polarisations on the feeds of the telescopes. Only the stronger 0x0 and 1x1 correlations will be used for localisation.

### 2.4.2 Calibration

As discussed in the previous section,  $\tilde{\tau}_{geo}$  is sub-frame and  $\tau_{clock}$ ,  $\tau_{iono}$ ,  $\tau_{inst}$ , and  $\xi$  are expected to be sub-frame. Thus, these delays cannot be resolved in the time-domain, but can be estimated using the phase  $\phi_{P_CP_O}[m]$  of the integrated visibility:

$$\phi_{P_{C}P_{O}}[m] = \text{Arg} \left[ \langle \mathcal{V}_{P_{C}P_{O}} \rangle_{t_{w}}[m] \right]$$

$$= 2\pi \ \nu[m] \ (\widetilde{\tau}_{geo} + \tau_{clock} + \tau_{iono}[m] + \tau_{inst}[m] + \xi)$$

$$= 2\pi \ \nu[m] \ \widetilde{\tau}_{total}[m]$$
(2.9)

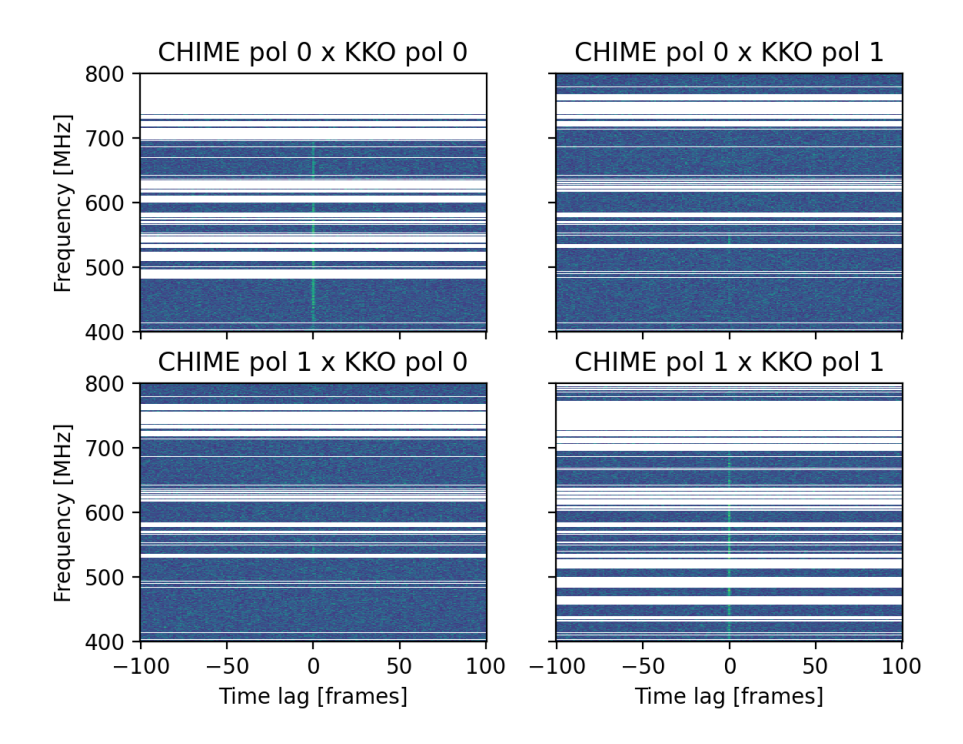


Figure 2.3: Amplitude of Crab pulsar cross-correlation for the CHIME-KKO baseline as a function of lag. 0 and 1 represent the East-West and North-South polarisations respectively, and x represents cross-correlation. The dedispersed cross-correlated pulses are visible at time lag 0 for all polarisation pairs. White patches are the RFI contaminated frequency channels which are masked out.

where  $\nu[m]$  is an array representing the central frequency of the frequency channel m, such that  $\nu[0] = 800$  MHz and  $\nu[1023] = 400.390625$  MHz. The goal of VLBI calibration is to extract  $\tilde{\tau}_{geo}$  from  $\tilde{\tau}_{total}$  by using known radio sources as calibrators.

 $au_{
m clock}$  is approximately tens of nanoseconds and encompasses the errors in the timestamps the GPS clock assigns to the baseband data. The free electron density in Earth's ionosphere also introduces a dispersive delay in the signal, similar to dispersive delay introduced by  ${
m DM_{total}}$  (Equation 1.4), but on nanosecond timescale.  $au_{
m iono}$  is due to the differential dispersive delay in the signal reaching CHIME and the Outrigger due to the differential ionospheric content  $\Delta {
m DM_{iono}}$  encountered along their line of sights.  $\Delta {
m DM_{iono}}$  is expected to be  $< 1 \times 10^{-6}$  pc cm<sup>-3</sup> and is thus much smaller than  ${
m DM_{total}}$ . It is important to note that while  $ilde{ au}_{
m geo}$  and  $au_{
m clock}$  are frequency-independent,  $au_{
m iono}$  is not due to its dispersive nature:

$$\tau_{\rm iono} = \frac{k_{\rm DM} \Delta DM_{\rm iono}}{\nu^2} \tag{2.10}$$

 $\tau_{\rm inst}$  encompasses the delay due to instrumental effects, such as longer cables at one site which carry the signals from the feeds to the F-X engine, introducing extra light travel time. This also encompasses frequency dependent beam effects which are not well understood, but are dependent on the position of the sky the data is beamformed to.  $\xi$  encompasses other repetitive noise errors.

Since  $\tau_{\rm inst}$  is dependent on position of the FRB on the sky, phase referencing  $\langle \mathcal{V}_{\rm P_C P_O} \rangle_{\rm t_w}$  to the integrated visibility of a calibrator close to the FRB position will cancel out  $\tau_{\rm inst}$  (see Section 4.4.1 for more details).

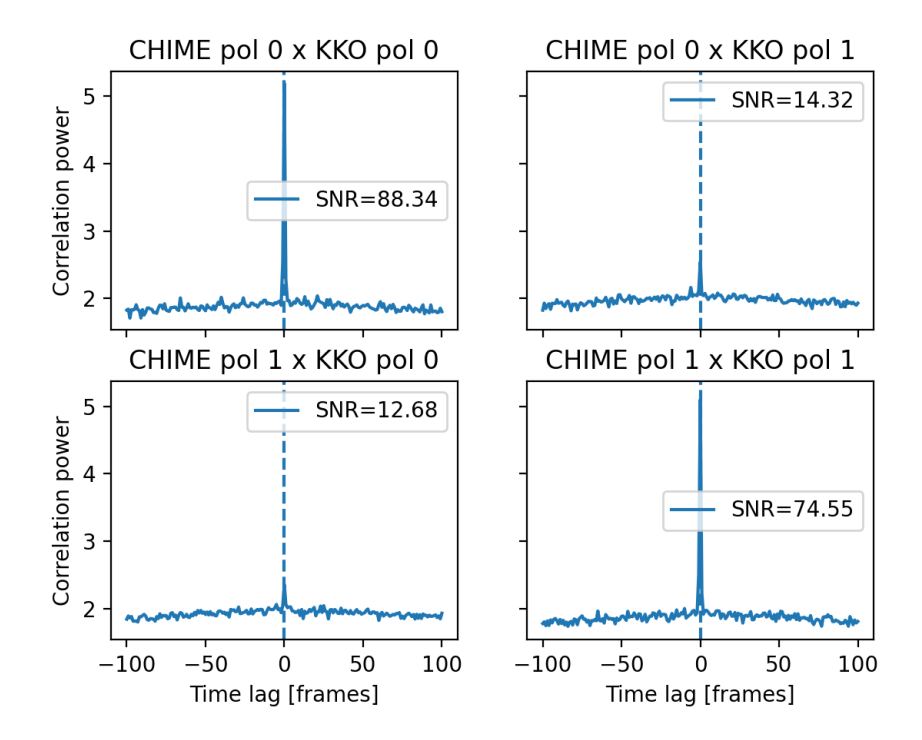


Figure 2.4: Correlation power and SNR corresponding to the cross-correlation visibility shown in Figure 2.3

It would also cancel out the repetitive error  $\xi$ . Due to spatial and temporal ionospheric fluctuations,  $\tau_{\rm iono}$  is highly dependent on the position of the FRB and also its TOA. Thus, if the calibrator is close in position and also close in time to when the FRB happened, referencing would cancel out most of  $\tau_{\rm iono}$ . An ideal calibrator is a radio source that is compact enough to be unresolved, bright enough to be detected in cross-correlation, and whose position is known to milli-arcsecond precision. For VLBI between CHIME and the Outriggers, we have opted to use pulsars (see Chapter 3 for more details) and in-beam steady continuum sources (see Section 4.4 for more details) as calibrators.

The following steps describe calibrating  $\langle \mathcal{V}_{P_C P_O} \rangle_{t_w}$  and extracting  $\tilde{\tau}_{geo}$ :

1. Firstly, we choose a viable calibrator which is close in time and position on the sky to the FRB and form its integrated visibility. We then form the phase-referenced visibility  $\mathcal{V}_{P_CP_O}^{tc}$ :

$$\mathcal{V}_{P_{C}P_{O}}^{tc}[m] = \langle \mathcal{V}_{P_{C}P_{O}}^{t} \rangle_{t_{w_{t}}}[m] \times \langle \mathcal{V}_{P_{C}P_{O}}^{c} \rangle_{t_{w_{c}}}^{*}[m]$$
(2.11)

where t and c represent target and calibrator respectively. The phase of this referenced visibility

looks like:

$$\begin{split} \phi^{\text{tc}}_{\text{P}_{\text{C}}\text{P}_{\text{O}}}[\mathbf{m}] &= \text{Arg} \left[ \left. \mathcal{V}^{\text{tc}}_{\text{P}_{\text{C}}\text{P}_{\text{O}}}[\mathbf{m}] \right. \right] \\ &= 2\pi \left. \nu[\mathbf{m}] \left[ \left( \widetilde{\tau}_{\text{geo}} + \tau^{\text{t}}_{\text{clock}} + \tau^{\text{t}}_{\text{iono}}[\mathbf{m}] + \tau^{\text{t}}_{\text{inst}}[\mathbf{m}] + \xi \right) - \left( \tau^{\text{c}}_{\text{clock}} + \tau^{\text{c}}_{\text{iono}}[\mathbf{m}] + \tau^{\text{c}}_{\text{inst}}[\mathbf{m}] + \xi \right) \right] \\ &= 2\pi \left. \nu[\mathbf{m}] \left[ \widetilde{\tau}_{\text{geo}} + \tau^{\text{tc}}_{\text{clock}} + \tau^{\text{tc}}_{\text{iono}}[\mathbf{m}] \right] \right. \\ &= 2\pi \left. \left[ \left( \widetilde{\tau}_{\text{geo}} + \tau^{\text{tc}}_{\text{clock}} \right) \nu[\mathbf{m}] + \frac{k_{\text{DM}} \delta \text{DM}^{\text{tc}}_{\text{iono}}}{\nu[\mathbf{m}]} \right] \right. \\ &= 2\pi \left. \nu[\mathbf{m}] \left. \widetilde{\tau}^{\text{tc}}_{\text{total}}[\mathbf{m}] \right. \end{split} \tag{2.12}$$

where  $\delta DM_{iono}^{tc} = \Delta DM_{iono}^{t} - \Delta DM_{iono}^{c}$ . Here we are assuming that  $\tau_{inst}^{t}[m] - \tau_{inst}^{c}[m]$  is negligible, since the instrumental delay is direction-dependent. Also, the calibrator does not have a geometric delay component since its position is well known.

2. The next step is to get a coarse-delay (cd) estimate  $\tau_{\rm cd}$  for  $\tilde{\tau}_{\rm total}^{\rm tc}$ .  $\tau_{\rm cd}$  is the  $\tau$  which maximises the subframe cross-correlation function  $\rho_{\rm P_C P_O}^{\rm sf}[\tau]$  (Cassanelli et al., 2022):

$$\rho_{\mathrm{P_CP_O}}^{\mathrm{sf}}[\tau] = \sum_{m=0}^{M-1} \mathcal{V}_{\mathrm{P_CP_O}}^{\mathrm{tc}}[\mathrm{m}] e^{-i2\pi\tau\mathrm{m/M}} = \mathrm{FFT}\left[\mathcal{V}_{\mathrm{P_CP_O}}^{\mathrm{tc}}\right]$$
(2.13)

$$\tau_{\rm cd} = \operatorname{argmax} \left( \rho_{\rm P_C P_O}^{\rm sf}[\tau] \right)$$
 (2.14)

3. A  $\chi^2$  minimisation (Equation 2.15) is used to fit  $\phi^{tc}_{P_CP_O}$  with a model  $\phi_{model}$  (Equation 2.16) and obtain a fine estimate  $\tau_{ff}$  for ( $\tilde{\tau}_{geo} + \tau^{tc}_{clock}$ ) and  $\delta DM_{ff}$  for  $\delta DM^{tc}_{iono}$  (Equation 2.17) . In this step, a grid of  $\tau$  formed around  $\tau_{cd}$  and  $\delta DM$  is searched and the values which minimise the  $\chi^2$  are the best-fit values:

$$\chi^{2}[\tau, \delta \text{DM}] = \sum_{m=0}^{M-1} \left| \frac{\mathcal{V}_{\text{P}_{\text{C}}\text{P}_{\text{O}}}^{\text{tc}}[\text{m}] - |\mathcal{V}_{\text{P}_{\text{C}}\text{P}_{\text{O}}}^{\text{tc}}[\text{m}]|e^{-i\phi_{\text{model}}[\text{m}, \tau, \delta \text{DM}]}}{\sigma_{\mathcal{V}_{\text{P}_{\text{C}}\text{P}_{\text{O}}}^{\text{tc}}}[\text{m}]^{2}} \right|^{2}$$
(2.15)

$$\phi_{\text{model}}[\mathbf{m}, \tau, \delta \mathbf{DM}] = 2\pi \left( \tau \nu[\mathbf{m}] + \frac{k_{\text{DM}} \delta \mathbf{DM}}{\nu[\mathbf{m}]} \right)$$
 (2.16)

$$[\tau_{\rm ff}, \delta DM_{\rm ff}] = \operatorname{argmin} (\chi^2 [\tau, \delta DM])$$
(2.17)

where  $\sigma_{\mathcal{V}_{P_{C}P_{O}}^{tc}}[m]$  is the variance of the phase-referenced visibility  $\mathcal{V}_{P_{C}P_{O}}^{tc}$ . This method essentially fits out  $\tau_{iono}^{tc}$ .

4.  $\tau_{\rm clock}^{\rm tc}$  can be calculated given the TOA of the FRB and the calibrator at CHIME and the Outrigger using the clock stabilisation pipeline developed by Mena-Parra et al. (2022) and described in detail in Section 4.4.2. Then, our estimate of  $\tilde{\tau}_{\rm geo}$  will be:

$$\widetilde{\tau}_{\text{geo}} = \tau_{\text{ff}} - \tau_{\text{clock}}^{\text{tc}}$$
 (2.18)

The errors in  $\tilde{\tau}_{geo}$  can stem from remaining instrumental delay, inaccurate fit for  $\delta DM_{iono}^{tc}$ , and the

errors in the clock stabilisation pipeline. We aim to estimate  $\tilde{\tau}_{geo}$  to an accuracy of 0.1 ns or better.

### 2.4.3 Localisation

 $\tilde{\tau}_{\text{geo}}$  (see Equations 2.7, 2.18) is the difference in geometric delay between the true location of the FRB  $(\alpha, \delta)$  defined by the baseline angle  $\theta(\alpha, \delta)$  and its initial coarse location  $(\alpha_0, \delta_0)$  defined by the baseline angle  $\theta_0(\alpha_0, \delta_0)$ . Then, according to Equation 1.6:

$$\frac{c}{b} \times \tilde{\tau}_{\text{geo}} = \cos \theta - \cos \theta_0 \tag{2.19}$$

$$\cos \theta - \cos \theta_0 = -\delta \theta \sin \theta_0 \tag{2.20}$$

$$\delta\theta = \theta - \theta_0 = \frac{c}{b} \times \frac{\widetilde{\tau}_{\text{geo}}}{\sin\theta_0}$$
 (2.21)

where c is the speed of light and b is the length of the baseline.  $\delta\theta$  gives the true location of the FRB relative to its initial location. As is apparent from Figure 1.3 and Equation 2.21,  $\delta\theta$  will only constrain the location of the FRB in one-dimension, along the baseline. For milli-arcsecond localisation in two-dimensions to reliably pin-point the FRB host galaxy, the procedure described above will be followed for nearly orthogonal baselines CHIME-GBO and CHIME-HCO (see Figure 2.2).

A successful implementation of these calibration and localisation techniques has recently been shown by Cassanelli et al. (2023), where a one-off FRB was localised to its host galaxy using the CHIME-ARO and CHIME-TONE baseline. ARO (Cassanelli et al., 2022) and TONE (Sanghavi et al., 2023) were the pathfinders to the Outriggers, and played a crucial role in the development of these algorithms. Section 4.4 describes using these algorithms for the CHIME-KKO baseline and testing our VLBI localisation accuracy.

# Chapter 3

# Realtime Beamforming of Pulsar

# Calibrators

Contributions: The realtime beamforming pipeline described in Section 3.2 was developed by and deployed at CHIME by the CHIME/Pulsar collaboration. Aaron Pearlman, Calvin Leung and Andre Renard are developing the algorithm for tracking, gating and cross-correlating pulsar calibrators described in Section 3.3. The discrepancy between the realtime and offline beamformers described in Section 3.3 was identified by Tomas Cassanelli and Calvin Leung. The work on figuring out and fixing the cause of this discrepancy described in Section 3.4 was done by myself.

As discussed in Section 2.4.2, VLBI calibrators should be unresolved on our baselines and bright enough to be detected in cross-correlation. Traditionally, radio continuum sources have been used for VLBI calibration, but most of these calibrators are either not detectable in our relatively low frequency band of 400-800 MHz or would be resolved on our longest baseline of ~3300 km. To overcome this challenge, we plan to employ a novel approach of using pulsars as calibrators since they are compact and would generally be unresolved on our baselines. Also, though individual pulsar pulses can be dim, a pulsar can be tracked as it transits through the sky and data for hundreds of its pulses can be recorded and stacked together to obtain high SNR. In this Chapter, I will discuss the realtime beamforming capability which allows tracking a pulsar calibrator and the upgrades I made to this beamformer to minimise the errors it can introduce in our localisations.

### 3.1 Theory of Beamforming

Beamforming is the process of digitally combining baseband data from all feeds in an interferometer to increase sensitivity towards a region of the sky. For a voltage stream  $v_n$  from feed n, the beamformed

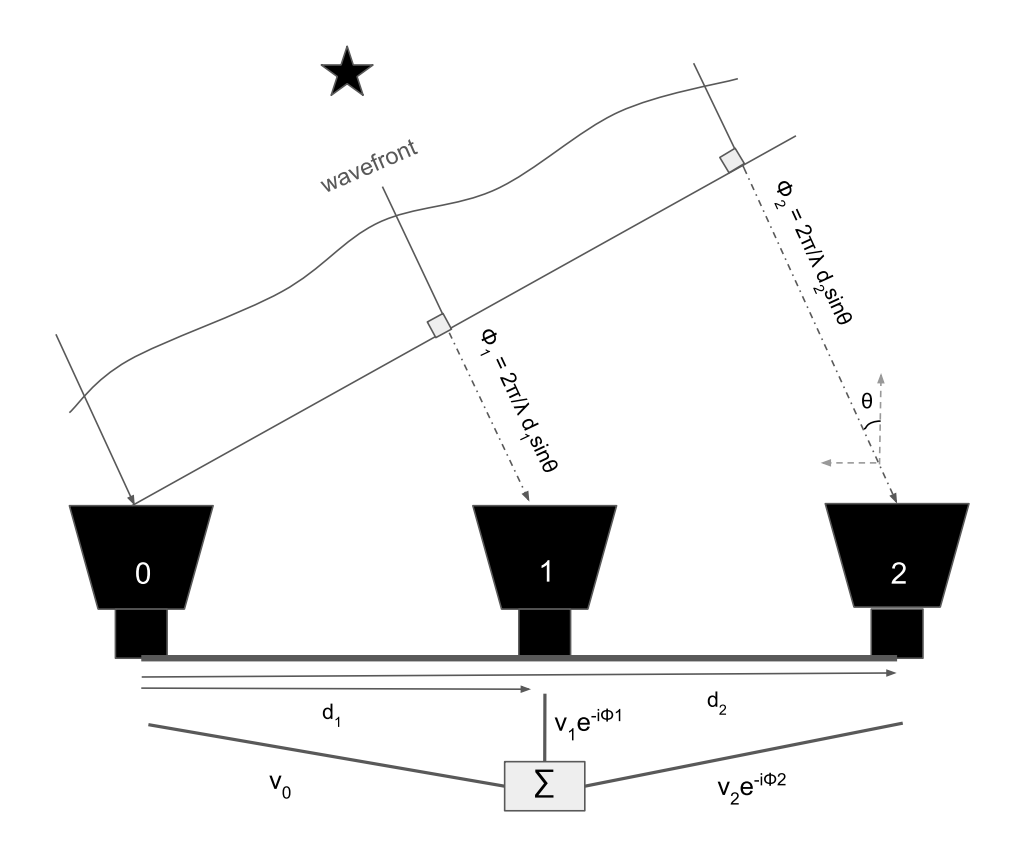


Figure 3.1: Figure showing 3 feeds of an interferometer where feed 0 is the phase centre and feeds 1 and 2 are separated by a distance  $d_1$  and  $d_2$  from feed 0.  $\lambda$  is the observing wavelength. The voltage data from feeds 0, 1 and 2 are rotated by a phase 0,  $\phi_1$  and  $\phi_2$  respectively and added to coherently beamform towards the source position.

voltage stream looks like:

$$V_{BF} = \sum_{n=1}^{N} a_n e^{i\phi_n} v_n \tag{3.1}$$

where  $a_n$  are amplitude weightings for the feeds and  $\phi_n$  are the phases. Ignoring instrument phases for now,  $\phi_n$  encompasses the geometric delay in the signals from a sky direction reaching the different feeds. If  $\hat{k}$  is the pointing vector to the source direction we want to beamform to and  $\mathbf{d}_n$  is the position vector from a reference point in the telescope called the phase centre to a feed n then:

$$\phi_{n} = \phi_{\text{geo}} = \frac{2\pi}{\lambda} \mathbf{d}_{n} \cdot \hat{k}$$

$$= 2\pi (u, v, w) \cdot \hat{k}$$

$$= 2\pi (u \hat{\mathbf{u}} \cdot \hat{k} + v \hat{\mathbf{v}} \cdot \hat{k} + w \hat{\mathbf{w}} \cdot \hat{k})$$
(3.2)

where  $\cdot$  represents dot product,  $(u, v, w) = (d_{ew}/\lambda, d_{ns}/\lambda, d_{vert}/\lambda)$ ,  $(d_{ew}, d_{ns}, d_{vert})$  are the projections of the vector  $\mathbf{d}_n$  on the x (east-west), y (north-south) and z (vertical) axes. As shown in Figure 3.1, a phase rotation is applied to  $\mathbf{v}_n$  to remove the geometric phase and the signals from all feeds are added to coherently beamform towards the desired direction. This will essentially destructively interfere signals

in all directions within the primary beam envelope except for the desired direction and the signals from the source will constructively interfere at the phase centre.

Given the RA ( $\alpha$ ) and Dec ( $\delta$ ) of the source, the latitude (lat) and longitude (long) of the telescope, the time of observation and Equation 3.2,  $\phi_n$  can be estimated using spherical trigonometry:

$$\phi_n = 2\pi (u, v, w) \cdot \begin{pmatrix} -\cos \delta \sin HA \\ \cos (\operatorname{lat}) \sin \delta - \sin (\operatorname{lat}) \cos \delta \cos HA \\ \sin (\operatorname{lat}) \sin \delta + \cos (\operatorname{lat}) \cos \delta \cos HA \end{pmatrix}$$
(3.3)

where the hour angle HA is the difference between the RA of the telescope's local meridian and RA of the source.

Realistically, beamforming by correcting for the geometric phases only would just give noise. This is because the signal seen by the correlator is very different from the signal hitting the feeds due to the extra phases called instrument gains added to the signal along the signal path by the amplifiers, FPGAs, coaxial cables, etc. It is thus essential to estimate and remove these phases while beamforming. The instrument gains are calculated once per day at CHIME during a bright continuum source transit when the N<sup>2</sup> matrix can be treated as a product of the gains and the sky signal. The eigendecomposition of this matrix for each frequency channel is done in the GPUs and the eigenvectors corresponding to the two largest eigenvalues represent the gains for the X and Y polarisations of each input (CHIME Collaboration, 2022). Thus, a gain is obtained for each input for each frequency channel and applied to the voltage stream before correcting for the geometric phase.

### 3.2 The Realtime Beamformer

Baseband data are used for cosmology and FRB science, and also for pulsar studies by the CHIME/Pulsar backend (CHIME/Pulsar Collaboration et al., 2021). This system consists of 10 compute nodes within the X-engine which beamform the baseband data in the 30 s buffer to form 10 dual-polarisation tied-array beams towards 10 different pulsar positions. As the pulsar transits across the sky, the compute nodes calculate and update the phases used for beamforming every 10s to repoint the beams and track the pulsars. This beamformed data are stored to disk in the VLBI Data Interchange Format (VDIF)<sup>1</sup> and later used for a variety of science projects. To decide which sources to track using these 10 "tracking" beams, a system called the tracking beam scheduler (TBS) is used which employs a probabilistic scheduling algorithm to prioritise sources based on user-defined weights. Once a pulsar tracked by a beam completes its transit, a new source to be tracked is decided by the TBS.

#### 3.2.1 Kotekan and Coco

Kotekan<sup>2</sup> is a highly optimised framework written in C and C++, primarily designed for processing data streams from radio telescopes (Recnik et al., 2015). It consists of buffer objects which buffer data

<sup>&</sup>lt;sup>1</sup>https://vlbi.org/vlbi-standards/vdif/

<sup>&</sup>lt;sup>2</sup>https://zenodo.org/record/5842660

and signal processing modules which can read/write data from/to the buffers and perform various data manipulation tasks. CHIME's X-engine runs kotekan to perform a variety of tasks including collecting data from the network and storing it in the ring buffers, computing the N<sup>2</sup> visibilities and the instrument gains from them and receiving FRB triggers from L4 to save data to disk. Kotekan also runs on CHIME/Pulsar's 10 compute nodes to calculate the phases used for beamforming.

Kotekan works in unison with coco (short for configuration controller) which tells it when to perform tasks. Coco is a framework which organises various nodes into groups and performs specific operations on the groups by calling endpoints when certain conditions are met. For example, CHIME's GPU nodes form a coco group and the FRB triggers from L4 are relayed to kotekan running on these nodes via the baseband endpoint. Once TBS selects a new pulsar to be tracked, a coco endpoint provides coordinates of this pulsar to kotekan running on the pulsar nodes. Kotekan and coco thus play a crucial role in CHIME's various operations.

## 3.3 Pulsars for VLBI Calibration

We plan to employ a novel approach of using pulsars as calibrators for our VLBI array of CHIME and CHIME/FRB Outriggers since pulsars are compact, abundant, and detectable in CHIME's observing band. About 100 potential pulsar calibrators have been identified which do not have complex morphologies, give a good RA and Dec coverage, and whose positions are known to milli-arcsecond accuracy. We are developing a framework in which two of the CHIME/Pulsar tracking beams will track two of these calibrators at any given time and their beamformed baseband data will be copied from the pulsar nodes and stored in a buffer after gating. The tracking beams at the Outriggers will also simultaneously track and buffer data from these pulsars. The gating algorithm will use the period of the pulsar to identify which part of the data will have the pulsar pulse. Only this on-pulse data will be stored in the buffer to economise data storage. Upon an FRB trigger, data from the buffer will be stored to disk at all telescope sites and cross-correlated. Since single pulses are dim for most pulsars, the cross-correlated visibilities from many gated pulses will be stacked together to reach a SNR threshold. After the FRB trigger, TBS will search for two more pulsar calibrators which are closest in space and time to the FRB. These will then be tracked by the tracking beams, and their gated data will be stored to disk, cross-correlated and stacked. This will give two pulsar calibrator cross-correlations before and after the FRB time of arrival to be used for calibration.

As described in Section 2.4.2, VLBI calibration should remove the unwanted instrumental and ionospheric delays. It is thus crucial that the process of calibration does not introduce any extra delays. Since the positions of the pulsar calibrators are known to <50 milli-arcsecond accuracy, difxcalc11 will remove all its geometric delay contribution while cross-correlating and calibration would not introduce any extra geometric delay. However, there is a major difference in how the FRB baseband data and pulsar calibrator baseband data are beamformed. The FRB data are beamformed offline using a python module called baseband-analysis at the initial localisation position determined by the baseband pipeline described in Section 2.2. The pulsar data are beamformed in realtime using kotekan C++ functions. To test that

these different beamforming schemes agree with one another, a gaint pulse from the Crab pulsar was recorded and beamformed using the tracking beams and baseband data for the same pulse was saved to disk from the ring buffer for offline beamforming. The realtime and offline beamformed pulses were then cross-correlated to find any delays between them. Several nanoseconds of sub-frame delay were found, hinting at a discrepancy between the beamformers. It is crucial to remove this discrepancy to minimise FRB localisation errors.

## 3.4 Upgraded Realtime Beamformer

In this Section, I describe my work on identifying the differences between the offline and realtime beamformers and writing an upgraded phase calculation code for the realtime beamformer to remove these differences. I also show a test I performed to demonstrate the agreement between the offline and upgraded realtime beamformers.

#### 3.4.1 Methods for Calculating Hour Angles

As described in Section 3.1, to compute the phases used for beamforming, the hour angle (HA) of the source is required. There are two methods used to compute HA, given the J2000 (RA, Dec) =  $(\alpha, \delta)$  of the source, the longitude  $\lambda$  of the telescope and the UT1 time of observation. The UT1 time, short for Universal Time, is a linear function of the Earth's average angular velocity of rotation  $\omega$ . Since  $\omega$  is changing with time<sup>3</sup>, UT1 deviates from the Universal Coordinated Time (UTC). The GPS timestamp assigned to the baseband data is UTC time which provides a constant rate of time measurement based on the International Atomic Time. An occasional 1-second adjustment called a leap second is added to UTC time to keep it within 0.9s of UT1 time. Past observation and future predictions of UT1-UTC offsets are published by the International Earth Rotation and Reference Service (IERS), which can be used to get the UT1 time from UTC time. The two methods to compute HA differ in their complexity but if employed correctly, should result in the exact same HA. The realtime beamformer uses the Local Sidereal Time (LST) approach while the offline beamformer uses the Local Stellar Angle (LSA) approach to calculate HA. The LST and LSA approaches are described below:

• LST approach: This approach makes use of the Greenwich Mean Sidereal Time (GMST) which is the RA of the Greenwich Meridian with respect to the mean equinox. As the Earth precesses about its axis, the vernal equinox moves along the celestial equator. Mean equinox is the current position of the equinox after taking into account precession. GMST can be calculated from UT1 time using a polynomial function which incorporates the accumulated precession of the equinox since J2000. The Local Sidereal Time (LST) and HA can then be calculated using GMST:

$$LST = GMST + \lambda; HA = LST - \alpha_{LST}$$
(3.4)

<sup>&</sup>lt;sup>3</sup>Historically,  $\omega$  was shown to decrease with time due to Moon's tidal effects. However, an increase in  $\omega$  has been observed since 2020 (Jones and Bikos, 2020) possibly due to climate change which has caused redistribution of Earth's mass due to melting of polar ice (Pappas, 2018).

where  $\alpha_{\text{LST}}$  is the RA of the source measured with respect of the mean equinox. TBS calculates  $\alpha_{\text{LST}}$  from  $\alpha$  using the python module astropy before passing it to the phase calculation function in kotekan. GMST should be computed using UT1 time, however, the realtime beamformer computes it using the UTC time provided by GPS. The UT1-UTC offset is small, but not negligible. Hence, this leads to an error in the HA calculation by the realtime beamformer.

- LSA approach: This approach makes use of the Earth Rotation Angle θ which is defined in the Celestial Intermediate Reference System (CIRS) with respect to the Celestial Intermediate Pole (CIP), the Celestial Intermediate Origin (CIO) and Terrestrial Intermediate Origin (TIO):
  - CIP is the celestial pole whose position is given by the new precession-nutation model adopted by the International Astronomical Union (IAU) (Kaplan, 2005). CIP is the true pole, orthogonal to the true equator. It has motion in the celestial reference frame because of Earth's precession and nutation. Additionally, it also has motion in the terrestrial reference frame because of the polar motion of the Earth. The Earth's axis is defined as the line through the geocenter in the direction of the CIP.
  - CIO is a point on the geocentric celestial sphere such that the rate of change of  $\theta$  with respect to this point is the angular velocity of the Earth. As the Earth precesses and nutates, CIO moves such that it always remains in the plane of the equator. The instantaneous motion of the CIO is always orthogonal to the equator, unlike the equinox which moves along the equator due to precession.
  - TIO is a point on the equator of CIP and on the surface of the Earth, that is, it rotates about the CIP as the Earth rotates. As the CIP moves due to the polar motion of the Earth, the equator of the CIP has a slight quasi-annual wobble around the geodetic equator. The TIO also moves accordingly to remain on the equator of the CIP.

 $\theta$  is the geocentric angle between the directions of CIO and TIO. Since CIO and TIO are defined in a way which takes into account the precession and nutation of the Earth,  $\theta$  can be calculated from UTI time using a linear function:

$$\theta = 2\pi \left( 0.7790572732640 + 1.00273781191135448 \, D_{U} \right) \tag{3.5}$$

where  $D_U$  is the number of UT1 days since JD 2451545 UT1. Then, the LSA and HA can be calculated using  $\theta$ :

$$LSA = \theta + \lambda; HA = LSA - \alpha_{LSA}$$
 (3.6)

where  $\alpha_{LSA}$  is the RA of the source in the CIRS reference frame, measured with respect to the CIO. In the offline beamformer, it is calculated from  $\alpha$  using the python module skyfield<sup>4</sup>.

I upgraded the phase calculation function in kotekan to calculate the HA using the LSA method

 $<sup>^4</sup>$ https://rhodesmill.org/skyfield/

which requires UT1 time as an input. The offline beamformer uses skyfield to get UT1-UTC offset provided by IERS, and converts the UTC timestamp given by GPS to UT1 time. However, this is difficult to do in the realtime beamformer since it is written in C++ which does not provide a module similar to skyfield. Consequently, we will calculate the UT1-UTC offset in the TBS (which is written in python) and provide it to kotekan using a coco endpoint periodically. I also upgraded the TBS to calculate  $\alpha_{LSA}$  using astropy and pass it to kotekan.

#### 3.4.2 Phase Centre and Feed Positions

As described in Section 3.1, the beamformed signals constructively interfere at the phase centre. The offline beamformer has the centre of CHIME as its phase centre, which also corresponds to the geographic location of CHIME defined in Table 2.1. The realtime beamformer, however, has the very first (top-left) CHIME feed as the phase centre. This is the major source of discrepancy between the beamformers, since different phase centres correspond to different light travel times from the source to the telescope. Depending on the source position, this can cause several nanoseconds (ns) of delay between the signals seen by the two beamformers. This ns scale error can be introduced in the referenced visibilities while calibrating with a pulsar calibrator and lead to a significant FRB localisation error. To counter this, the upgraded realtime beamformer has the same phase centre as that of the offline beamformer. Moreover, since the feed positions are defined with respect to the phase centre (see Figure 3.1), the upgraded beamformer has feed positions with respect to the updated phase centre.

To test these upgrades, I beamformed towards the position of the Crab pulsar at 24 different timestamps spread across a day at 400 MHz frequency and using 4 adjacent CHIME antennas in the North-South direction (that is, belonging to the same cylinder) instead of the full-array of antennas. The first of these antennas is defined as the phase centre, giving three baselines with the other 3 antennas. Since we are trying to make the realtime beamformer as similar to the offline beamformer as possible, I beamform using the offline beamformer and employ three approaches to beamform using the realtime beamformer. These three approaches are:

- 1. LST approach to calculate HA, with a UTC time input. This is the approach used in the original realtime beamformer.
- 2. LSA approach to calculate HA, with a UTC time input.
- 3. LSA approach to calculate HA, with a UT1 time input. This is the approach used in the offline beamformer.

Figure 3.2 shows the differences in the hour angles between the offline beamformer and the three approaches for the realtime beamformer described above across the 24 epochs. It also shows the corresponding differences in the beamforming phase  $\phi_n$  calculated for one of the feeds using the HA. As expected, the realtime beamformer is the most similar to the offline beamformer when it uses the LSA approach with the UT1 time inputs to calculate HA.

Since the realtime beamformer resides in kotekan and is an integral part of the software used for pulsar

science, the availability of kotekan and CHIME/Pulsar experts is crucial during the deployment of the upgraded realtime beamformer. For this reason, the upgraded code is yet to be deployed at CHIME and the Outriggers. Once it is deployed, data from the two beamformers will be cross-correlated to check for any remaining discrepancies between them.

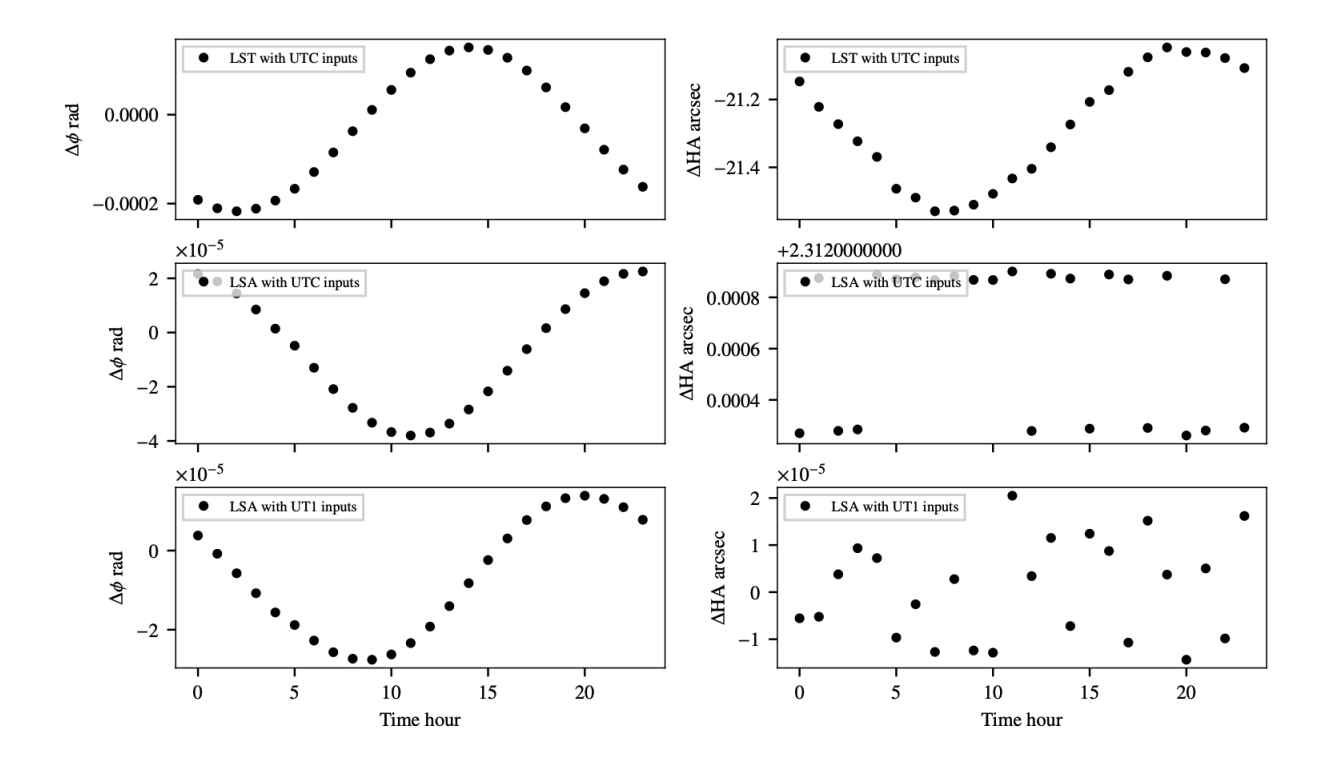


Figure 3.2: Figure showing the differences in hour angles ( $\Delta$ HA) and phases ( $\Delta\phi$ ) computed by the offline and realtime beamformers at different times during the day for the Crab pulsar at 400 MHz frequency. Top, middle and bottom rows are for the different approaches to the realtime beamforming listed above. This shows that the majority of discrepancy comes from using the LST approach and that the realtime beamformer is the most similar to the offline beamformer when it uses the LSA approach with the UT1 time inputs to calculate HA.

## Chapter 4

# KKO: Commissioning and Towards

## Science Readiness

Contributions: The commissioning of KKO has largely been a team effort. The trigger management system described in Section 4.2.1 was developed by Ryan Mckinven, Shiny Brar, Tarik Zegmott and myself. The scheduled acquisitions pipeline described in Section 4.2.2 was set up at KKO by myself. The offline beamforming pipeline, including the code to make the waterfall plot (Figure 4.4) was set up at KKO by Mattias Lazda. The beamforming tests described in Section 4.3.1 were done by Mattias Lazda, Shion Andrew and myself. The SEFD measurement described in Section 4.3.2 was done by myself. The analysis on measuring the effect of instrument gains on VLBI delays described in Section 4.4.1 was done by myself. The clock stabilisation pipeline described in Section 4.4.2 and the code to make Figure 4.8 was set up at KKO by Juan Mena-Parra and Nina Gusinskaia. The analysis on testing the accuracy of our calibration techniques described in Section 4.4.3 was done by myself.

In this chapter, I give an overview of KKO, the first CHIME/FRB Outrigger. I describe the pipelines we set up to acquire data at KKO and the tests we carried out to ensure data integrity and performance of the telescope. I also describe the analysis I did to test the accuracy of our VLBI techniques for the CHIME–KKO baseline.

### 4.1 Overview of KKO

k'ni?atn k'l\_stk'masqt¹ (KKO), the first CHIME/FRB Outrigger, is located in Princeton, British Columbia. With a 66-km line-of-sight distance to CHIME, it can achieve 1 arcsec resolution in the CHIME band of 400-800 MHz. This relatively short baseline makes KKO easily accessible to CHIME's DRAO and UBC staff for maintenance purposes. While the choice of site provides excellent Radio Frequency Interference (RFI) protection from the neighbouring towns, a significant portion of the frequency

<sup>&</sup>lt;sup>1</sup>From the upper Similkameen language, this translates to "a listening device for outer space"

band from 600 - 640 MHz and 700 - 760 MHz is contaminated by RFI from wireless communication, TV broadcasting bands, direct transmission from satellites and airplanes, and from a LTE/5G tower installed near KKO. Table 4.1 describes the KKO system.

Geographic location	49° 25' 8.5794" N
	$120^{\circ} \ 31' \ 31.08" \ \mathrm{W}$
Elevation	$800\mathrm{m}$
Baseline to CHIME	$66.2\mathrm{km}$
Cylinder width	$20\mathrm{m}$
Cylinder length	$40\mathrm{m}$
Instrumented cylinder length	$19.5\mathrm{m}$
Number of dual-polarization feeds	64
Observing band	$400800\mathrm{MHz}$

Table 4.1: KKO characteristics

KKO is very similar to CHIME in terms of its optical design, analog and digital systems (CHIME Collaboration, 2022). It has one 40 m long and 20 m wide cylindrical paraboloidal reflector with a 5-m focal length aligned north-south and occupies 1/16 of CHIME's collecting area (see Figure 4.1). The telescope is rolled and rotated by  $\sim 0.5^{\circ}$  so that it sees the same sky as CHIME. The focal line contains 64 dual-polarisation cloverfeed antennas giving 128 signals which are carried using coaxial cables to the receiver hut for further processing. The receiver hut houses the F-X engine. The F-engine performs amplification, bandpass filtering, digitisation, channelisation of the signals into 1024 frequency channels and the "corner-turn" operation using 8 ICE boards each of which processes 16 input signals. The X-engine is a 128-input correlator composed of 2 GPU nodes, each of which processes 512 frequency channels. It receives the corner-turned data from the F-engine and buffers it in a 30-second ring buffer, performs cross-multiplication and integration to produce visibilities used for calculating the daily calibration solutions, and transfers data to other nodes for further processing. In addition, KKO has three compute/storage nodes called c1, c2, c3 to receive, post-process and store data as well as for on-site analysis. There are also has two "auxiliary" (aux) nodes, which run services meant for housekeeping and emergency shutdowns and manage the distribution of processes across other nodes.

KKO saw first light in June 2022 and has been in commissioning since then. It does not have a FRB detection backend. Instead, it has a system in place to receive triggers from CHIME upon an FRB detection by CHIME's FRB backend. Data are saved to disk upon such a FRB trigger. The following section describes the systems for handling and forwarding these triggers in more detail.

## 4.2 Baseband Data Acquisition

#### 4.2.1 FRB trigger management system

At CHIME, when an FRB is detected with a SNR > 12, L4 initiates the acquisition of baseband data by calling the coco baseband endpoint. As described in Section 3.2.1, coco enables organisation of various nodes into groups and performing specific operations on the groups by calling endpoints when certain



Figure 4.1: Aerial view of KKO. The receiver hut on the side houses the F-X engine. The trolley attached on the focal line allows easy access to the feeds for assembly and maintenance.

conditions are met. To trigger a baseband acquisition, L4 calls the baseband endpoint with a payload containing the event id, the file path where the data must be saved, the start time of the acquisition, the duration of data to be saved and the DM of the FRB. The duration sent with the payload is always ~100 ms, which economizes disk space and is sufficient for FRB bursts having durations of only a few milliseconds. Coco forwards this payload to kotekan running on the X-engine nodes. Since the latency of the FRB search backend is only a few seconds, FRB data corresponding to the start time specified in the payload will be contained in the 30-s ring buffer. Upon receiving the payload, kotekan stores 100 ms of voltage data centred around the start time from the ring buffer to an internal buffer which is then transferred to the FRB archiver. CHIME/FRB Collaboration (2018) gives a detailed description of this triggered baseband recording system.

Since the outriggers are rolled and rotated to see the same sky as CHIME, an FRB detected by CHIME would also be seen by the outriggers. Thus, the outriggers do not need to detect an FRB, and do not have the L1-L4 backend. However, they do need to save data at the time of an FRB detection by CHIME to be able to do VLBI. To enable this, a triggered VLBI baseband acquisition system was developed where upon an FRB detection, L4 simultaneously sends the baseband payload to baseband endpoint at CHIME and to the workflow system. The workflow system provides a well-defined framework for sharing information across networks and acts as a interface between CHIME and the Outriggers. The Outriggers persistently run a receiver service which queries the workflow system to look for new payloads deposited by L4. Upon receiving such a payload, the receiver service forwards it to the coco baseband endpoint at the Outrigger site. After that, a procedure similar to that at CHIME is followed to save 100 ms of voltage data centred around the start time specified in the payload from the ring buffer to an

internal buffer. A persistent service running kotekan saves the data from the internal buffer to c1. The latency of forwarding the trigger from L4 to coco at the Outrigger sites is < 1 s, and the light travel time between CHIME and the Outriggers is only a few milliseconds (< 1 millisecond for KKO), thus, 100 ms of FRB data can be safely saved from the 30-s ring buffer. The receiver service also calls the coco baseband\_status endpoint to check the status of the triggered baseband acquisition and returns the status to workflow. A useful feature of workflow is that it provides a GUI where all the baseband triggers to the outrigger sites, their payloads and their status can be easily viewed. See Figure 4.2 for a schematic diagram explaining the baseband acquisition system at CHIME and the Outriggers.

My contribution to this system was setting up coco at KKO and implementing the coco baseband

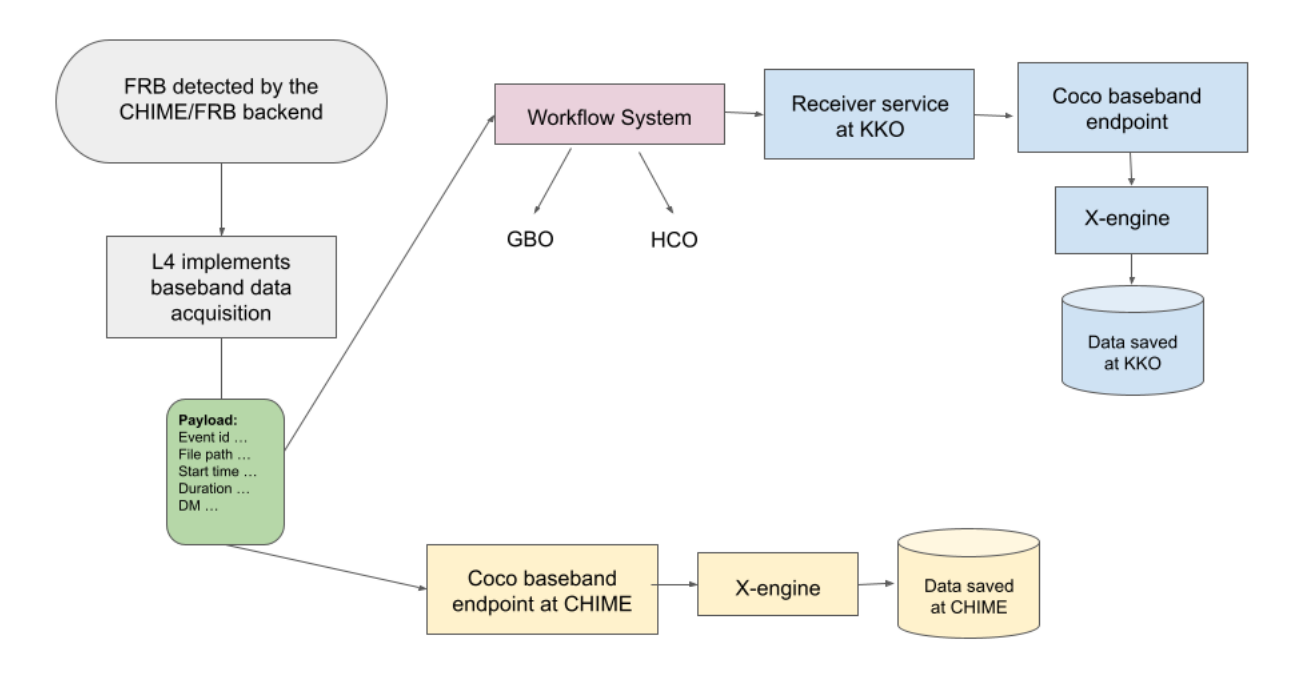


Figure 4.2: Schematic diagram of the FRB trigger management system.

endpoint call in the receiver service. Unlike CHIME, most of the services running at KKO use docker which provides an easy framework to package software in containers, and also to package co-dependently running software together in stacks. I set up the coco docker service at KKO which enabled running the coco daemon persistently on one of the aux nodes. I also set up the baseband endpoint and baseband\_status endpoint files<sup>2</sup> which define the payload accepted by the endpoints and where the payload should be forwarded. Finally, I wrote a python function called baseband\_dump\_status<sup>3</sup> which enables the receiver service to call the baseband\_status endpoint.

 $<sup>^2</sup> The \quad endpoint \quad files \quad can \quad be \quad found \quad here: \quad https://github.com/CHIMEFRB/outrigger-devops/tree/main/docker/stacks/kko/configs/coco\_endpoints$   $^3 The \quad python \quad function \quad can \quad be \quad found \quad here: \quad https://github.com/CHIMEFRB/outrigger-coordination-devolution-de$ 

#### 4.2.2 Scheduled acquisition of bright sources

Once the coco docker service to obtain baseband data was set up, we were in a position to obtain data not just from FRBs but also from bright radio continuum sources and pulsars to test the performance of KKO as a radio interferometer. To get data for these bright sources, we need to send a trigger to the X-engines to save data at the transit time of the source at KKO. The transit time is the time when the source crosses the meridian of KKO and can be easily calculated using python modules such as skyfield given the RA of the source and the latitude and longitude of KKO. A script already existed to get the transit times of required sources, construct a payload for the coco baseband endpoint and call the endpoint with the payload. I modified this script so that it can be used at KKO, and so that a trigger is sent to the X-engines no more than 5 minutes before the transit time of the source. This would avoid the issue of the X-engines waiting for a start time way in the future and missing the triggers that come in between. Making use of cron, which is a utility used to schedule tasks repeatedly at a specific time, I set up a cron job to send baseband triggers for continuum radio sources Cygnus A (CygA) and Cassiopeia A (CasA) and the bright pulsar B0329+54 every day and get 500 ms of data for these sources. As described in the next section, these daily baseband acquisitions enabled tests of data integrity and debugging of pipelines.

## 4.3 KKO system characteristics

### 4.3.1 Beamforming tests

As described in Chapter 3, the baseband voltage data can be digitally beamformed to any position in the sky using the offline beamforming pipeline. The scheduled acquisitions of bright sources (described in 4.2.2) allowed tests of the offline beamforming pipeline set up at KKO. Firstly, we beamformed CygA data at its true RA but over a range of declinations, taking the amplitude square of the beamformed voltage data to obtain power as a function of declinations. Ideally, we would expect to see a peak in the power at the true declination of CygA. Departure from this behaviour helped us identify and fix a bug in the phase of the instrumental gains. Fig 4.3 shows the resulting baseband power peaking at the true declination of CygA for multiple frequencies.

We also beamformed the pulsar B0329+54 and plotted a dedispersed waterfall plot to show the pulsar pulse in the frequency and time domain. Fig 4.4 shows the first pulsar pulse beamformed at KKO, proving that KKO is capable of detecting millisecond transients! Along with the beamforming pipeline, these tests also proved the efficient working of the entire data acquisition pipeline, starting from the analog feeds to the baseband receiver docker service on c1.

## 4.3.2 Noise Characteristics

The scheduled baseband acquisitions also allowed measurements of the system noise and sensitivity, including the System Equivalent Flux Density (SEFD). Traditionally, SEFD is defined as the flux density of a radio point source at the centre of the telescope beam which would double the system temperature

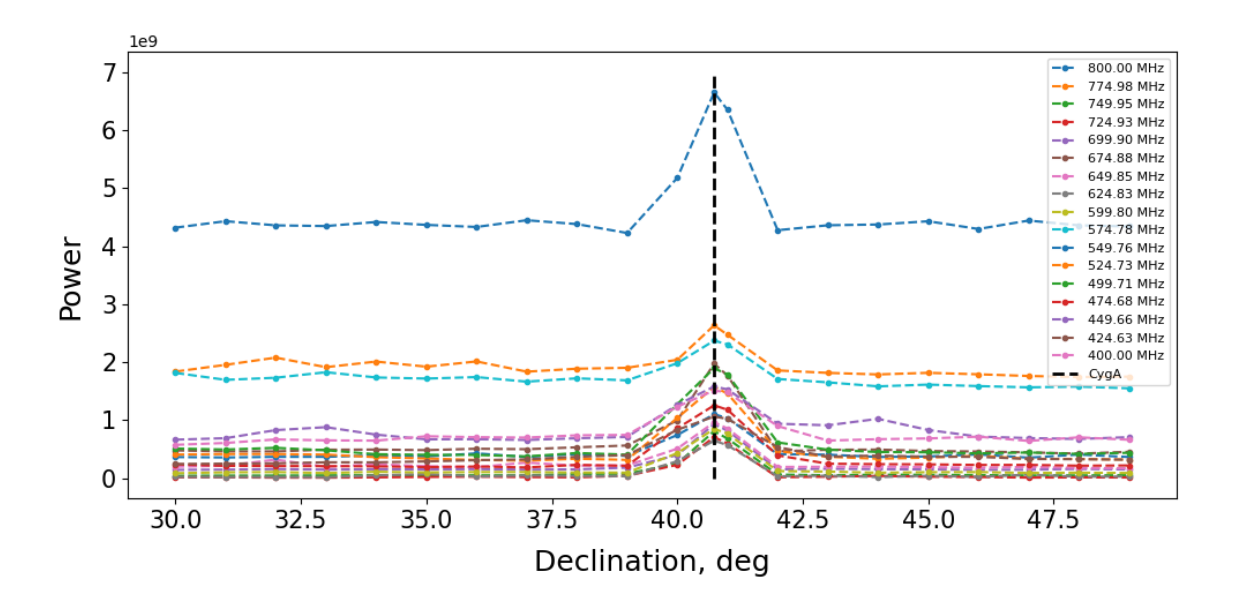


Figure 4.3: A plot showing the beamforming test where the baseband power peaks at the true declination of CygA, and thus proves the correctness of the beamforming pipeline.

 $T_{\rm sys}$ , but it could also be thought of as  $T_{\rm sys}$  expressed in units of flux density (Jansky (Jy)).  $T_{\rm sys}$  encompasses the radio noise from the feeds and receiver chain of the telescope and also from background sources such as RFI and the Milky Way's Galactic plane. The lower the SEFD, the better the sensitivity of the telescope. Since we will use the beamformed voltage data for our science purposes, we want to estimate the SEFD of the phased-array and not individual feeds. This can be done using Equation 4.1.

$$\begin{aligned} \text{SEFD}_{\nu} &= \text{T}_{\text{sys},\nu} \times \text{gain}_{\nu} = \text{T}_{\text{sys},\nu} \times \frac{\text{F}_{\nu}}{\text{T}_{\text{src},\nu} - \text{T}_{\text{sys},\nu}} \\ &= \text{P}_{\text{sys},\nu} \times \frac{\text{F}_{\nu}}{\text{P}_{\text{src},\nu} - \text{P}_{\text{sys},\nu}} \end{aligned}$$
(4.1)

where  $\nu$  is frequency, gain<sub> $\nu$ </sub> is the conversion factor at frequency  $\nu$  which converts K to Jy,  $T_{src,\nu}$  is the telescope temperature when there is a bright point source in the field of view,  $P_{sys,\nu}$  is the beamformed power when there is no bright source in the beam,  $P_{src,\nu}$  is the beamformed power when there is a bright source in the beam,  $F_{\nu}$  is the flux of the bright source in Jy. Equation 4.1 follows from the fact that power observed by the telescope is directly proportional to its temperature.

I measured the SEFD of the KKO phased array using 500 ms of scheduled baseband data of the bright source CygA. I beamformed these data towards the true position of CygA at (RA, Dec) = (299.86815, 40.73392) degrees and got  $P_{\text{src},\nu}$  by taking the amplitude square of the beamformed data. Similarly, I beamformed the same data at a source-free region of the sky at (RA, Dec) = (299.86815, 60) degrees and got  $P_{\text{sys},\nu}$ . This resulted in power as a function of frequency and time in arbitrary digital units. I added the time frames to get the power as a function of frequency alone.  $F_{\nu}$  can be easily calculated since the theoretical spectral flux density of CygA as a function of frequency is known (Perley and Butler, 2017; Vollmer et al., 2010). Using Equation 4.1, I obtain the SEFD.

I repeated the same analysis at CHIME using CygA baseband data and beamforming only using 64 central antennas on one cylinder to match KKO's antenna configuration. Figure 4.5 shows the measured

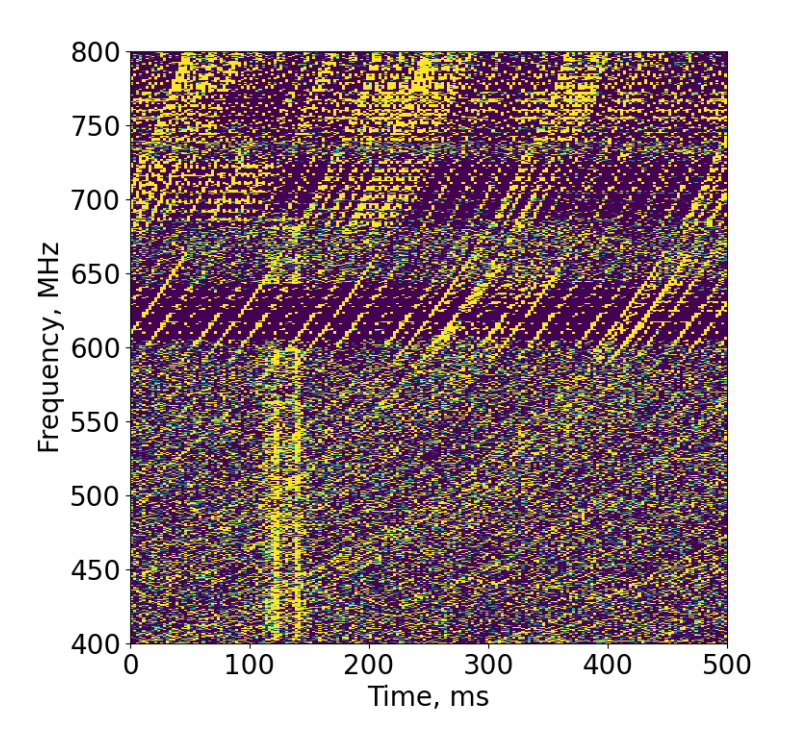


Figure 4.4: Waterfall plot of the first PSR B0329+54 pulse detected at KKO from the scheduled baseband acquisition. There are two sub-pulses separated by  $\sim\!20$  ms, a known feature of this pulsar. The RFI contaminated frequency channels from 600 - 640 MHz, 690 - 730 MHz, and 740 MHz - 800 MHz are masked out.

SEFD of CHIME and KKO plotted for the N-S and E-W polarisations. The 30 MHz ripple is expected and is the interference fringe due to the multi-path propagation of the wavefront between CHIME's focal line and the ground plane (CHIME Collaboration, 2022). Features in the RFI dominated frequency bands of 600 - 640 MHz and 700 - 760 MHz show that data in these bands might not be usable. There is an excellent agreement between the SEFD of CHIME and KKO, which tells us that the noise levels of KKO are within our expectations.

## 4.4 VLBI Analysis

After establishing the performance of KKO as a standalone interferometer, we proceeded towards doing VLBI with CHIME and KKO. The integrated visibility  $\langle \mathcal{V}_{P_C P_O} \rangle_{t_w}[m]$  formed by cross-correlating the beamformed data from two telescope sites, its phase  $\phi_{P_C P_O}[m]$  and the delay  $\tilde{\tau}_{total}[m]$  it encompasses are described in Sections 2.4.1 and 2.4.2 where  $P_C$  and  $P_O$  are the polarisations at CHIME and the outrigger (KKO in this case) respectively and m represents frequency channels. The analysis presented here is done using the algorithms described in Section 2.4 but with pulsars and continuum radio sources whose positions are known to milli-arcsecond accuracy. Consequenty,  $\tilde{\tau}_{geo}$  is negligible and  $\tilde{\tau}_{total}[m]$  becomes:

$$\widetilde{\tau}_{\text{total}}[\mathbf{m}] = \tau_{\text{clock}} + \tau_{\text{iono}} + \tau_{\text{inst}} + \xi$$
 (4.2)

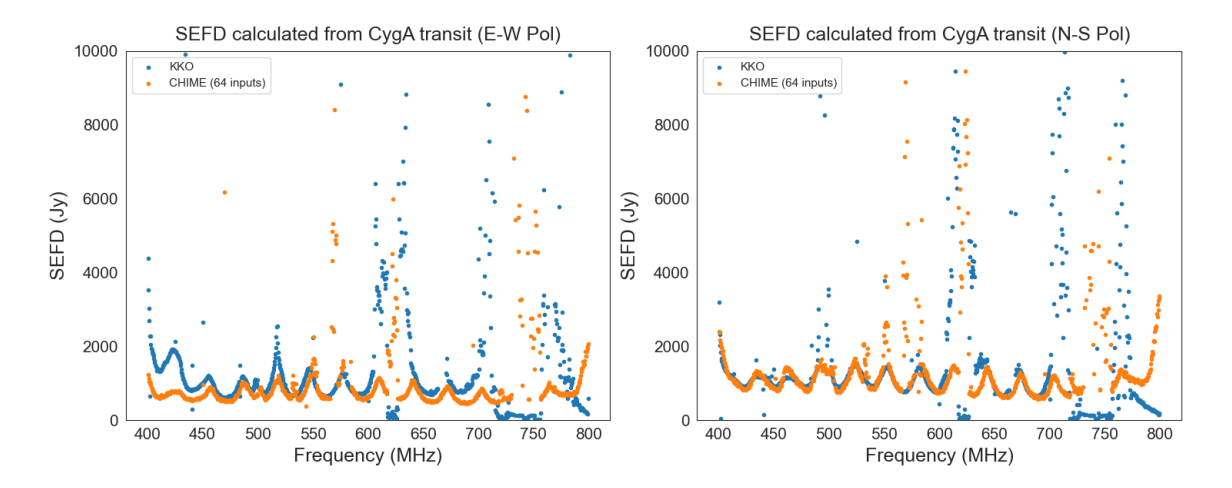


Figure 4.5: A plot made by me showing the comparision of KKO SEFD with CHIME SEFD obtained from 64 antennas for the E-W and N-S polarisations.

This allows us to test the effect of the unwanted delays  $\tau_{\text{clock}}$ ,  $\tau_{\text{iono}}[m]$  and  $\tau_{\text{inst}}[m]$  on  $\tilde{\tau}_{\text{total}}[m]$  and how accurately we can remove them using calibration.

### 4.4.1 Effect of instrument gains on VLBI delays

As described in Section 3.1, instrument gains are applied to the baseband voltage data in the process of beamforming to counter the phases introduced in the data by instrumental effects. These gains are calculated once a day at each telescope site and are expected to be stable for the course of a few days. To test the effect of gains on  $\tilde{\tau}_{\text{total}}$ , I used the baseband data for the Crab pulsar pulse simultaneously obtained at CHIME and KKO using the FRB trigger management system described in Section 4.2.1. I beamformed the Crab pulse at KKO with gains from seven different days, thus generating seven beamformed singlebeam files. These seven days included the day when the Crab data were taken (12-08-2022), and three days before (12-05-2022, 12-06-2022, 12-07-2022), and three days after (12-09-2022, 12-10-2022, 12-11-2022). I also beamformed the corresponding Crab pulse at CHIME but only using the gains of the same day as the data. I cross-correlated the seven KKO beamformed files individually with the one CHIME beamformed file. This generated 7 sets of visibility data from which the coarse delay  $\tau_{\text{cd}} = \tilde{\tau}_{\text{total}}$  (described in Section 2.4.2) was extracted. Figure 4.6 shows the  $\tau_{\text{cd}}$  obtained for the cross-correlation where the data at KKO and CHIME were beamformed using the gains calculated on 12-08-2022. The lower panel of the plot shows the phase residuals  $\phi_{\text{corrected}}$  as a function of frequency.  $\phi_{\text{corrected}}$  is the phase  $\phi_{\text{PCPO}}$  after correcting it for  $\tau_{\text{cd}}$ :

$$\phi_{\text{corrected}}[m] = \text{Arg} \left[ \langle \mathcal{V}_{PCPO} \rangle_{t_w}[m] e^{-i2\pi \tau_{cd} \nu[m]} \right]$$
 (4.3)

If we have correctly estimated the sub-frame delay contained in  $\phi_{P_CP_O}$ , then  $\phi_{corrected}$  should not have a  $\nu$  dependence and should essentially be zero, as can be seen in Figure 4.6, except for the curvature in the RFI contaminated frequency band. There are two different cross-correlations here: 0x0 where the CHIME E-W polarisation is cross-correlated with KKO E-W polarisation and 1x1 where the CHIME

N-S polarisation is cross-correlated with KKO N-S polarisation. There is a difference of  $\sim 0.9$  ns between the 0x0 and 1x1  $\tau_{\rm cd}$ , which can be attributed to different  $\tau_{\rm inst}$  for the E-W and N-S polarizations.

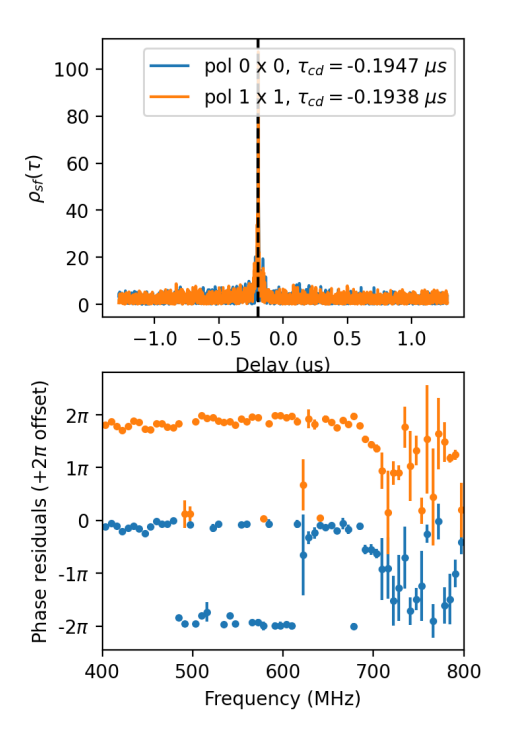


Figure 4.6: Top panel: The coarse-delay  $\tau_{\rm cd} = \tilde{\tau}_{\rm total}$  which maximises the sub-frame cross-correlation function  $\rho_{sf}(\tau)$  for the CHIME-KKO Crab pulse cross-correlation for the 0x0 (blue) and 1x1 (orange) polarisation pairs. Bottom panel: The corresponding  $\phi_{\rm corrected}$  as a function of frequency.

The first column of Figure 4.7 shows the  $\tilde{\tau}_{\text{total}}$  as a function of gain file used for beamforming the KKO data for the 0x0 and 1x1 cross-correlations. As can be seen,  $\tilde{\tau}_{\text{total}}$  is stable for all the different gains used, with a negligible difference of  $\sim 0.07$  ns.  $\sim 0.07$  ns is 2.56  $\mu$ s /  $2^{15}$  which is the resolution of the FFT performed in Equation 2.14. Since we are aiming to obtain  $\tilde{\tau}_{\text{total}}$  with an accuracy of  $\sim 0.1$  ns, we can safely ignore the  $\sim 0.07$  ns difference. This established the stability of KKO instrument gains on timescales of days in the context of VLBI.

To test the stability of CHIME gains, I also beamformed the Crab pulse at CHIME with gains from 7 different days. I then cross-correlated the 7 CHIME beamformed files with the corresponding 7 KKO beamformed files. The second column of Figure 4.7 shows the  $\tilde{\tau}_{\text{total}}$  thus obtained for the 0x0 and 1x1 cross-correlations, which are stable except for the negligible difference of  $\sim$ 0.07 ns.

This analysis obtained the VLBI delay  $\tilde{\tau}_{total}$  for a Crab pulse cross-correlation, where the baseband data were beamformed using instrument gains from 7 different days. The stability of  $\tilde{\tau}_{total}$  for these multiple cross-correlations establishes that instrument gains from a few days before or after the time of the data would not affect  $\tau_{inst}$ , and thus  $\tilde{\tau}_{total}$ . Essentially, it proves that  $\tau_{inst}$ , which is directly dependent on the instrument gains, would be constant for the course of a few days.

As described in Section 2.4.2,  $\tau_{\rm inst}$  is known to have a directional dependence, that is, it depends on the position of the source on the sky. A major reason for this is the directional dependence of the 30 MHz ripple (CHIME Collaboration, 2022), which is also observed in the phase of the visibility. It is thus difficult to quantify  $\tau_{\rm inst}$ , but since we proved that it is constant in time, it can be removed by

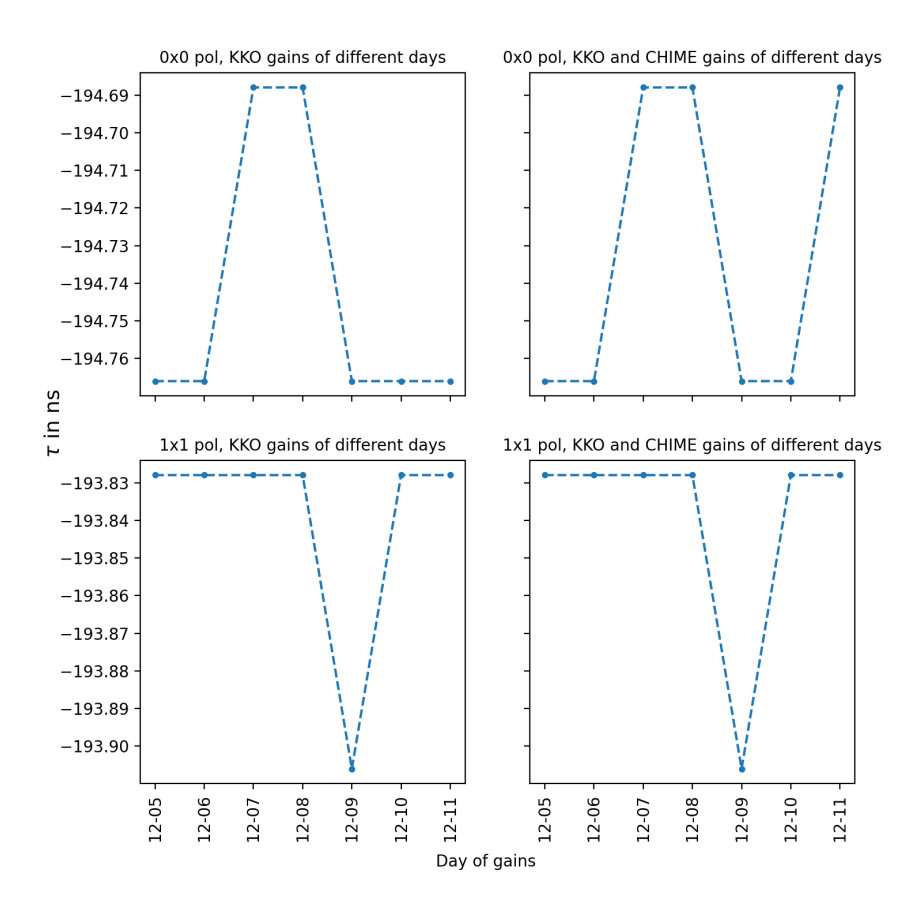


Figure 4.7: The coarse-delay  $\tau_{\rm cd} = \tilde{\tau}_{\rm total}$  for the CHIME-KKO Crab pulse cross-correlation as a function of the gain files used to beamform the data.

referencing the visibility of the source to the visibility of a near-by calibrator. The repetitive errors  $\xi$  would also be removed in the process. Since both the calibrator and source have known positions in this analysis, the delay  $\tilde{\tau}_{\text{total}}^{\text{tc}}[m]$  after referencing becomes:

$$\widetilde{\tau}_{\text{total}}^{\text{tc}}[\mathbf{m}] = \tau_{\text{clock}}^{\text{tc}} + \tau_{\text{iono}}^{\text{tc}}[\mathbf{m}].$$
 (4.4)

## 4.4.2 Effect of clock-drift on VLBI delays

As described in Mena-Parra et al. (2022), the 10 MHz clock signal provided by the Global Positioning System (GPS)-disciplined ovenized crystal oscillator generates a timecode signal synchronised to the clock which is used by the X-engine to timestamp the baseband data. Mena-Parra et al. (2022) carried out simulations to find that in order to localise an FRB to 50 milli-arcsecond precision with a baseline of 1000 km, the error on the measured VLBI delay  $\tilde{\tau}_{\text{total}}$  should be  $\sigma_{\tau} \approx 800$  picoseconds (ps). Considering that ionosphere would be the main contributor to  $\sigma_{\tau}$ , the clock timing error specification was set to  $\sigma_{\tau}^{clk} \lesssim 200$  ps for a calibrator which is  $\Delta t < 10^3$ s apart from the source in time. They show that the CHIME GPS clock does not meet this specification because it drifts more than 200 ps on a timescale of  $\sim 10^3$ s. However, a hydrogen maser, such as the one available at DRAO, meets this specification. They

designed a clock stabilisation system that calculates the drift  $\tau_{\rm maser}^{\rm GPS}$  of the GPS clock with respect to the DRAO maser at a cadence of 0.2 s, which essentially transfers the time measured by the GPS to the time measured by the more precise maser. KKO has a Rubidium (Rb) oscillator clock instead of a maser. GBO and HCO might also have to use a Rb clock depending on the availability of a maser at their respective sites. The Rb clock is more stable than the GPS clock, but it still does not meet the clock timing error specification. However, by interpolating timing solutions between calibrators, we expect to be able to keep timing errors below 225 ps up to  $\Delta t \sim 10^3 s$  (Cary et al., 2021). The clock stabilisation system was deployed at KKO and calculates the drift  $\tau_{\rm Rb}^{\rm GPS}$  of the GPS clock with respect to the Rb clock at a cadence of 0.2 s. With the clock stabilisation system in place,

$$\tau_{\rm clock} = (\tau_{\rm maser}^{\rm GPS} - \tau_{\rm Rb}^{\rm GPS}) \tag{4.5}$$

$$\tau_{\text{clock}}^{\text{tc}} = \left[\tau_{\text{maser}_t}^{\text{GPS}} - \tau_{\text{Rb}_t}^{\text{GPS}}\right] - \left[\tau_{\text{maser}_c}^{\text{GPS}} - \tau_{\text{Rb}_c}^{\text{GPS}}\right]$$
(4.6)

Figure 4.8 shows  $\tau_{\text{maser}}^{\text{GPS}}$  and  $\tau_{\text{Rb}}^{\text{GPS}}$  for CHIME and KKO, respectively, calculated for a duration of 5 hours at a cadence of 0.2 s. As can be seen,  $\tau_{\text{maser}}^{\text{GPS}}$  is more stable in time than  $\tau_{\text{Rb}}^{\text{GPS}}$ . Nevertheless, these measurements would allow us to calculate  $\tau_{\text{clock}}^{\text{tc}}$ , as has been done in the analysis described in the next section.

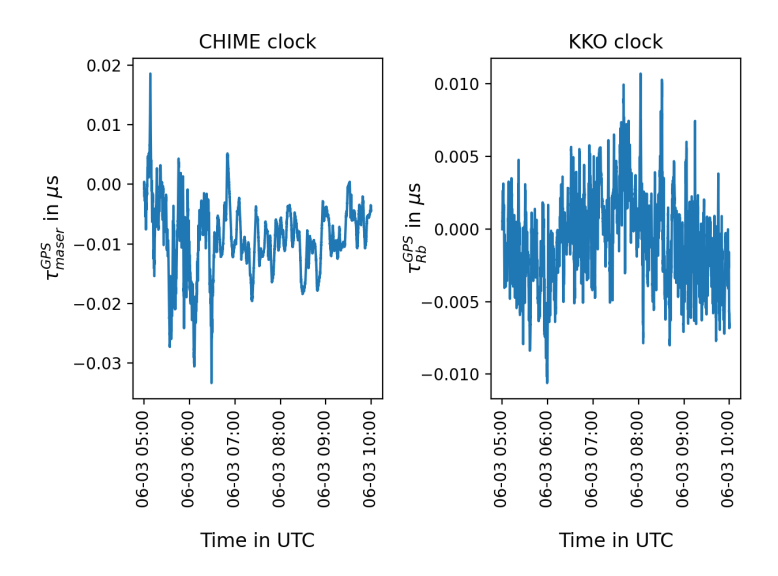


Figure 4.8:  $\tau_{\rm maser}^{\rm GPS}$  and  $\tau_{\rm Rb}^{\rm GPS}$  for CHIME and KKO respectively, calculated for a duration of 5 hours at a cadence of 0.2 s.

#### 4.4.3 Effect of ionosphere on VLBI delays

One of the main challenges of VLBI calibration is the ionosphere, which is the ionised part of the upper atmosphere of the Earth. The free electron density of the ionosphere along the line of sight of the FRB signal causes an additional dispersive delay. For VLBI, since the two telescope sites are separated by a large distance, the line of sights of the FRB signal to the telescopes pass through different electron contents, and thus have different ionospheric dispersive delays which show up in the phases of the visibility as described in Section 2.4.2. The ionosphere varies with time and position on the sky, and thus we want a reference calibrator which is close in space and time to the source so that  $\delta DM_{iono}^{tc}$  and thus  $\tau_{iono}^{tc}$  are small. How close the calibrator needs to be depends on the inhomogeneity in the ionosphere at the time and it is not always possible to find a calibrator which will make  $\tau_{iono}^{tc}$  negligible.

I carried out an analysis to test the effect of ionosphere and the accuracy of  $\tau^{\rm tc}_{\rm clock}$  measured using the clock stabilisation pipeline described in Section 4.4.2 on minutes to hours timescales. For this, I use the steady radio source J0117+8928 with RA (J2000) = 19.3875 degrees, DEC (J2000) = 89.4803 degrees listed in the NVSS catalog (Condon et al., 2002), henceforth referred to as the NCP (North Celestial Pole) source. Because of the very high declination of the source, it is always in CHIME's and KKO's field of view, and will be visible in all baseband data. Using the utility to schedule baseband data described in Section 4.2.2, I collected 12 baseband acquisitions separated by 10 mins at night and 12 baseband acquisitions separated by 10 mins during sunrise at Penticton. The free electron density in the ionosphere is due to the ionising radiation of the Sun and is the minimum at night and maximum during sunrise, thus night and sunrise represent the two extreme ends of the ionospheric impact on  $\tilde{\tau}^{\rm tc}_{\rm total}$ . For each of these two datasets, the very first baseband acquisition is taken as the calibrator for the remaining 11 baseband acquisitions, giving a time  $\Delta t$  between source and calibrator ranging from 10 mins to 1 hr 50 mins.

To find  $\tilde{\tau}_{\rm total}^{\rm tc}[{\rm m}]$  for this NCP dataset, I use the fringe-fitting method described in 2.4.2. I first get the  $\tau_{\rm cd}$  from the coarse-delay method and search for  $\tilde{\tau}_{\rm total}^{\rm tc}$  in an array [-5× $\tau_{\rm cd}$ , 5× $\tau_{\rm cd}$ ] sampled at 10 ps. I also search for the best-fit  $\delta {\rm DM_{iono}^{tc}}$  from an array [-1e<sup>-6</sup>, 1e<sup>6</sup>] pc/cm<sup>3</sup> sampled at 3.85e<sup>-9</sup> pc/cm<sup>3</sup> (Following Equation 2.10, the  $\tau_{\rm iono}^{\rm tc}$  corresponding to 3.85e<sup>-9</sup> pc/cm<sup>3</sup> at 600 MHz is 0.1 ns). I perform the fringe-fit in two ways:

Case1: Assuming a zero DM contribution in  $\tilde{\tau}_{\text{total}}^{\text{tc}}$  and setting  $\delta \text{DM}_{\text{iono}}^{\text{tc}} = 0$ , the resulting best-fit  $\tau_{\text{ff}} = \hat{\tau}_{\text{no-DM}}$ .

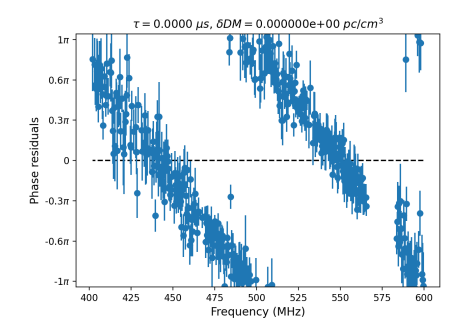
Case2: Assuming a non-zero DM contribution in  $\tilde{\tau}_{total}^{tc}$  and fitting for a  $\delta DM_{iono}^{tc} \neq 0$ , the resulting best-fit  $\tau_{ff} = \hat{\tau}_{DM}$ .

The  $\phi_{\text{corrected}}$  in this case would be:

$$\phi_{\text{corrected}}[\mathbf{m}] = \operatorname{Arg} \left[ \mathcal{V}_{\mathbf{P}_{\mathbf{C}}\mathbf{P}_{\mathbf{O}}}^{\text{tc}}[\mathbf{m}] e^{-i2\pi(\tau_{\text{ff}}\nu[\mathbf{m}] + k_{\text{DM}}\delta \mathbf{D}\mathbf{M}_{\text{ff}}/\nu[\mathbf{m}])} \right]$$
(4.7)

If the ionospheric contribution in  $\tilde{\tau}_{\text{total}}^{\text{tc}}$  is truly small, as expected by referencing with a calibrator which is close in time and space to the source, then the  $\phi_{\text{corrected}}$  would have no  $\nu$  dependence and would be  $\sim 0$  for both the first and the second cases. Figure 4.9 shows an example where the phase-wrap of  $\phi_{P_C P_O}^{\text{tc}}$  is corrected without having to fit for the ionosphere, that is,  $\delta \text{DM}_{\text{iono}}^{\text{tc}}$  is negligible. On the other hand, in Figure 4.10, a non-zero  $\delta \text{DM}_{\text{iono}}^{\text{tc}}$  is required to correct for the  $\nu$  dependence of  $\phi_{P_C P_O}^{\text{tc}}$ . This proves that  $\delta \text{DM}_{\text{iono}}^{\text{tc}}$  is highly time dependent, and would not always be zero. Note that frequency channels with high RFI contamination and with  $\mathcal{V}_{P_C P_O}^{\text{tc}}/\sigma_{\mathcal{V}_{P_C P_O}}^{\text{tc}} < 1$  are masked out.

I obtain  $\tau_{\rm clock}^{\rm tc}$  using Equation 4.6. Since the measurement cadence of the clock stabilisation system



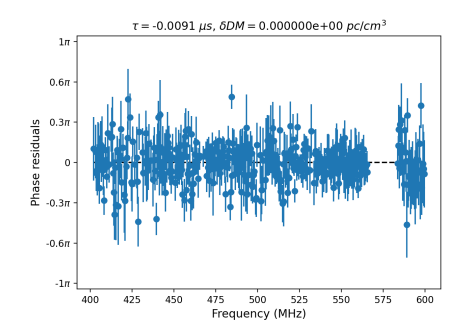


Figure 4.9: Case 1, from left to right the plots represent the wrapped phase  $\phi_{P_CP_O}^{tc}$ ; and the unwrapped phase  $\phi_{corrected}^{tc}$  where the visibility  $\mathcal{V}_{P_CP_O}^{tc}$  is corrected with  $\hat{\tau}_{no-DM}$  and  $\delta DM = 0$ 

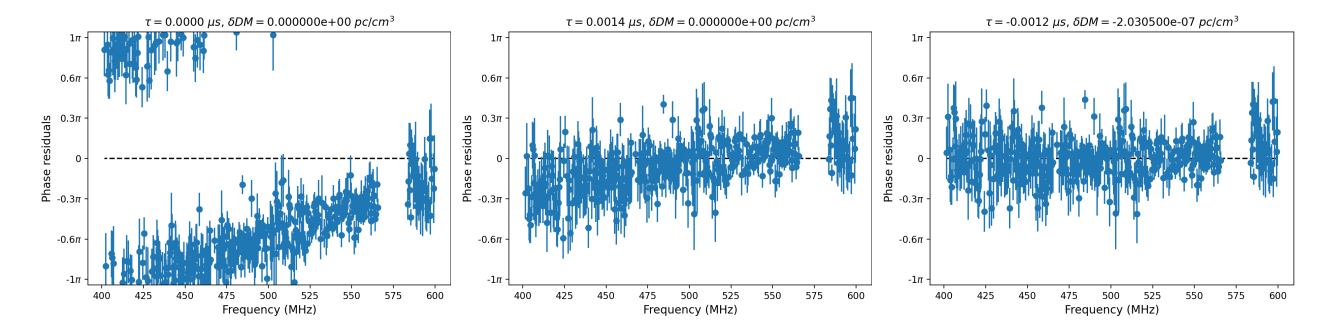
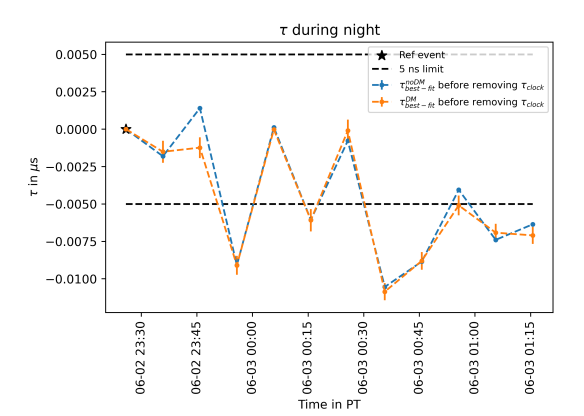


Figure 4.10: Case 2, from left to right the plots represent the wrapped phase  $\phi_{P_CP_O}^{tc}$ ; the unwrapped phase  $\phi_{corrected}^{corrected}$  where the visibility  $\mathcal{V}_{P_CP_O}^{tc}$  is corrected with  $\hat{\tau}_{no\text{-}DM}$  and  $\delta DM = 0$ ; the unwrapped phase  $\phi_{corrected}$  where the visibility  $\mathcal{V}_{P_CP_O}^{tc}$  is corrected with  $\hat{\tau}_{DM}$  and a non-zero  $\delta DM_{ff}$ .

is 0.2 seconds, if the time of observation of the source and reference is between two measurements, the  $\tau_{\text{clock}^t}$  and  $\tau_{\text{clock}^c}$  were found by linearly interpolating the two measurements. I then subtract  $\tau_{\text{clock}}^{\text{tc}}$  from both  $\hat{\tau}_{\text{no-DM}}$  and  $\hat{\tau}_{\text{DM}}$ . Since the reference calibrator and the source are both the NCP sources, which has approximately the same position in the sky at any given time due to its high declination, we expect delay contribution from the instrument to be small. In the case where  $\delta DM_{iono}^{tc}$  is small,  $(\hat{\tau}_{no-DM} - \tau_{clock}^{tc})$ is expected to be  $\sim 0$ . Departure from 0 would indicate the presence of an ionospheric contribution and the need to fit for a non-zero  $\delta DM_{iono}^{tc}$ . In that case,  $(\hat{\tau}_{DM} - \tau_{clock}^{tc})$  is expected to be  $\sim 0$  since the ionospheric contribution will be accounted for while fringe-fitting. Figure 4.11 shows the  $\hat{\tau}_{\text{no-DM}}$  and  $\hat{\tau}_{\text{DM}}$ before and after removing the clock correction for the NCP acquisitions taken during night. Figure 4.12 shows the  $\hat{\tau}_{\text{no-DM}}$  and  $\hat{\tau}_{\text{DM}}$  before and after removing the clock correction for the NCP acquisitions taken during sunrise. As can be seen from the right panel of both of these figures, neither  $(\hat{\tau}_{\text{no-DM}} - \tau_{\text{clock}}^{\text{tc}})$  nor  $(\hat{\tau}_{DM} - \tau_{clock}^{tc})$  are 0, but both quantities are less than 5 ns away from 0. This is crucial for two reasons. Firstly, the non-zero residual delay tells us that either the  $\tau_{\rm clock}^{\rm tc}$  calculated by the clock pipeline is not accurate enough on the timescales used for this analysis, or the instrumental delay is non-zero, or the  $\delta DM_{\rm ff}$  calculated by Equation 2.17 is not an accurate representation of the true ionospheric contribution. Further analysis is required to understand the reasons for the obtained results. Secondly, we wanted to achieve an error of < 5 ns on the residual delay before starting to do VLBI with FRBs. This analysis shows that this criterion is met when a calibrator is close in space to the source and separated in time by up to  $\sim 2$  hours.



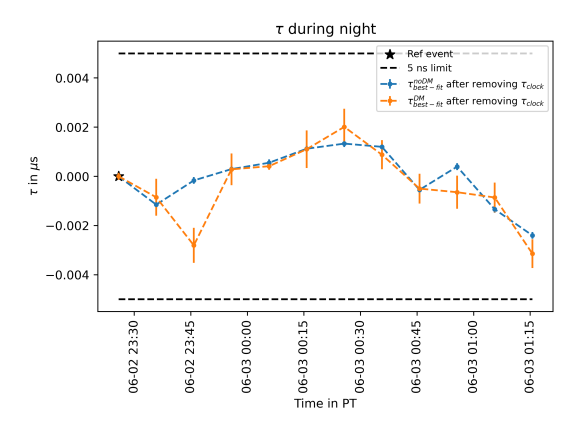
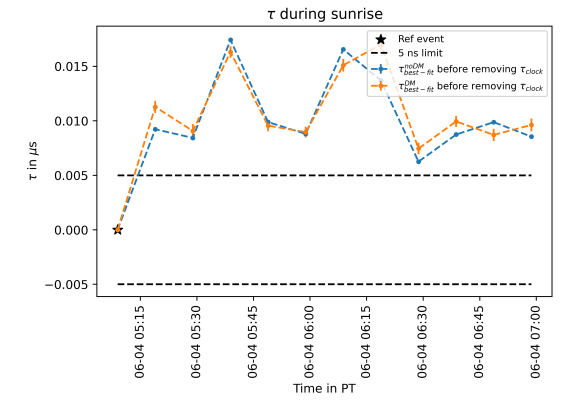


Figure 4.11: Fringe-fit delays for the 12 NCP acquisitions taken during night, each separated by 10 mins. The first acquisition (marked by a black star) is the reference calibrator for all the other acquisitions. The left plot shows the delays before applying clock correction, that is,  $\hat{\tau}_{\text{no-DM}}$  and  $\hat{\tau}_{\text{DM}}$ . The right plot shows the delays after applying clock correction, that is,  $(\hat{\tau}_{\text{no-DM}} - \tau_{\text{clock}}^{\text{tc}})$  and  $(\hat{\tau}_{\text{DM}} - \tau_{\text{clock}}^{\text{tc}})$ . The clock-corrected residual delays are not zero, but within our threshold of <5 ns for all acquisitions spanning  $\sim$ 2 hours.



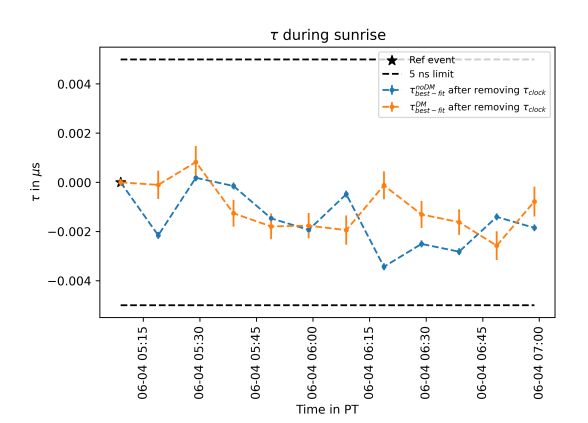


Figure 4.12: Same as Figure 4.11, but for NCP acquisitions taken during sunrise.

## Chapter 5

## Conclusion

It has been a decade and a half since the first FRB was detected, and yet, the origins of FRBs remain unknown. Localising FRBs to their host galaxies, or event better, to their local regions within the hosts can give clues about their origins. The host galaxies of about two dozen FRBs which have been localised exhibit a broad range of properties including colour, stellar mass, star formation rates, ages and luminosities. Localising more FRBs to their host galaxies can allow us to identify their different classes and formation channels based on where they occur. More localisations can also allow us to statistically verify the validity of the Macquart relation and thus trace the "missing" baryons in the Universe.

CHIME and the CHIME/FRB Outriggers will form a VLBI array to localise FRBs to sub-arcsecond precision, allowing host galaxy identification. In this thesis, we discuss the use of pulsars, which are compact and detectable in CHIME's observing band of 400-800 MHz, as calibrators for our VLBI array. The real-time beamformer used to beamform the pulsar calibrators and the offline beamformer used to beamform FRBs should agree so that the process of calibration does not introduce any extra localisation errors. We discussed that a discrepancy of several nanoseconds exists between the two beamformers, mainly because they use different phase centres and methods of hour angle computation. We show that after upgrading the realtime beamformer to use the same phase centre and hour angle computation method as that of the offline beamformer, the beamforming phases of the two beamformers show an excellent agreement. These upgrades have not been deployed at CHIME and the Outriggers yet. The future goal is to deploy these upgrades and test if any discrepancy still exists between the two beamformers.

We also discuss the commissioning of KKO, the first CHIME/FRB Outrigger. FRB data at KKO are acquired using a trigger management system in which baseband data is stored to disk upon receiving a FRB trigger from CHIME. We describe the set up of coco and the coco baseband and baseband\_status endpoints which relay the FRB trigger from CHIME to KKO's X-engine and provide the status of the baseband acquisition. We also discuss the capability to save baseband data to disk during bright source or pulsar transits by sending a coco paylod to the X-engine containing their transit times. We describe the beamforming tests which verified the correctness of the offline beamforming pipeline deployed at KKO and demonstrated KKO's capability to detect pulsar giant pulses. We showed that the noise characteristics of the KKO phased array is comparable to CHIME's which established the performance of

KKO as a standalone interferometer.

We further discuss how the instrument gains used in the process of beamforming, clock drifts and dispersive ionospheric delays impact the VLBI delays obtained for the CHIME-KKO baseline. We crosscorrelated and obtained VLBI delays for a Crab pulse beamformed at CHIME and KKO using instrument gains from different days (3 days before to 3 days after the time of the data) to show that the gains are stable on  $\sim$  days timescales and do not impact the VLBI delays. This in turn shows that apart from its directional dependence, the contribution to the VLBI delay which comes from the instrument is constant on ~ days timescales. Thus, phase-referencing the FRB visibilities with a calibrator close in time and space to the FRB should cancel out this contribution. We also discuss the clock stabilisation pipeline, which allows time measurement at CHIME and KKO to be transferred from the less accurate GPS clock to the more accurate hydrogen maser clock (at CHIME) and Rubidium (Rb) oscillator clock (at KKO). We show that using this pipeline, the difference between the time measured at CHIME and KKO can be calculated, which contributes a few nanoseconds to the VLBI delay. To test the performance of the clock pipeline and the fluctuations in the ionosphere on a time scale of  $\sim 2$  hours, we did an analysis using 12 acquisitions of a radio continuum source at the North Celestial Pole (the NCP source) each during sunrise and midnight. The cross-correlated visibilities of these acquisitions were phase-referenced to the visibility of the very first acquisition obtained in the 2 hour timespan which should cancel out the delays introduced due to the instrument. VLBI delays were obtained from the referenced visibilities by assuming the ionospheric contribution to be zero in one case and non-zero in the other. We show that some acquisitions show the presence of an ionospheric contribution, while some do not. The clock delay was calculated using the clock stabilisation pipeline and subtracted from the VLBI delays. Ideally, we would expect the remaining delay to be zero, but it is observed to be within 5 ns of zero whether we assume a zero or non-zero ionosphere. This shows that we have a few nanoseconds of delay still unaccounted for, either due to errors in the clock pipeline, inaccurate method of measuring ionospheric delays or any remaining instrumental delay. Future works should focus on understanding these remaining delays. Nevertheless, we wanted to achieve an error of <5 ns on our VLBI delays before we start doing VLBI on FRBs. This study shows that the error threshold is met and we are ready to do FRB localisations with the CHIME-KKO baseline.

# **Bibliography**

- K. Bandura, J. F. Cliche, M. A. Dobbs, A. J. Gilbert, D. Ittah, J. Mena Parra, and G. Smecher. ICE-Based Custom Full-Mesh Network for the CHIME High Bandwidth Radio Astronomy Correlator. *Journal of Astronomical Instrumentation*, 5(4):1641004, December 2016. doi: 10.1142/S225117171641004X.
- K. W. Bannister, A. T. Deller, C. Phillips, J. P. Macquart, J. X. Prochaska, N. Tejos, S. D. Ryder, E. M. Sadler, R. M. Shannon, S. Simha, C. K. Day, M. McQuinn, F. O. North-Hickey, S. Bhandari, W. R. Arcus, V. N. Bennert, J. Burchett, M. Bouwhuis, R. Dodson, R. D. Ekers, W. Farah, C. Flynn, C. W. James, M. Kerr, E. Lenc, E. K. Mahony, J. O'Meara, S. Osłowski, H. Qiu, T. Treu, V. U, T. J. Bateman, D. C. J. Bock, R. J. Bolton, A. Brown, J. D. Bunton, A. P. Chippendale, F. R. Cooray, T. Cornwell, N. Gupta, D. B. Hayman, M. Kesteven, B. S. Koribalski, A. MacLeod, N. M. McClure-Griffiths, S. Neuhold, R. P. Norris, M. A. Pilawa, R. Y. Qiao, J. Reynolds, D. N. Roxby, T. W. Shimwell, M. A. Voronkov, and C. D. Wilson. A single fast radio burst localized to a massive galaxy at cosmological distance. Science, 365(6453):565–570, August 2019. doi: 10.1126/science.aaw5903.
- Shivani Bhandari and Chris Flynn. Probing the Universe with Fast Radio Bursts. *Universe*, 7(4):85, April 2021. doi: 10.3390/universe7040085.
- Shivani Bhandari, Kasper E. Heintz, Kshitij Aggarwal, Lachlan Marnoch, Cherie K. Day, Jessica Sydnor, Sarah Burke-Spolaor, Casey J. Law, J. Xavier Prochaska, Nicolas Tejos, Keith W. Bannister, Bryan J. Butler, Adam T. Deller, R. D. Ekers, Chris Flynn, Wen-fai Fong, Clancy W. James, T. Joseph W. Lazio, Rui Luo, Elizabeth K. Mahony, Stuart D. Ryder, Elaine M. Sadler, Ryan M. Shannon, JinLin Han, Kejia Lee, and Bing Zhang. Characterizing the Fast Radio Burst Host Galaxy Population and its Connection to Transients in the Local and Extragalactic Universe., 163(2):69, February 2022. doi: 10.3847/1538-3881/ac3aec.
- M. Bhardwaj, B. M. Gaensler, V. M. Kaspi, T. L. Landecker, R. Mckinven, D. Michilli, Z. Pleunis, S. P. Tendulkar, B. C. Andersen, P. J. Boyle, T. Cassanelli, P. Chawla, A. Cook, M. Dobbs, E. Fonseca, J. Kaczmarek, C. Leung, K. Masui, M. Mnchmeyer, C. Ng, M. Rafiei-Ravandi, P. Scholz, K. Shin, K. M. Smith, I. H. Stairs, and A. V. Zwaniga. A Nearby Repeating Fast Radio Burst in the Direction of M81., 910(2):L18, April 2021. doi: 10.3847/2041-8213/abeaa6.
- Savannah Cary, Juan Mena-Parra, Calvin Leung, Kiyoshi Masui, J. F. Kaczmarek, Tomas Cassanelli, and Chime/Frb Collaboration. Evaluating and Enhancing Candidate Clocking Systems for CHIME/FRB

- VLBI Outriggers. Research Notes of the American Astronomical Society, 5(9):216, September 2021. doi: 10.3847/2515-5172/ac289d.
- T. Cassanelli, Calvin Leung, M. Rahman, K. Vanderlinde, J. Mena-Parra, S. Cary, Kiyoshi W. Masui, Jing Luo, H. H. Lin, A. Bij, A. Gill, D. Baker, Kevin Bandura, S. Berger, P. J. Boyle, Charanjot Brar, S. Chatterjee, D. Cubranic, Matt Dobbs, E. Fonseca, D. C. Good, J. F. Kaczmarek, V. M. Kaspi, T. L. Landecker, A. E. Lanman, Dongzi Li, J. W. McKee, B. W. Meyers, D. Michilli, Arun Naidu, Cherry Ng, Chitrang Patel, Aaron B. Pearlman, U. L. Pen, Ziggy Pleunis, Brendan Quine, A. Renard, Pranav Sanghavi, K. M. Smith, Ingrid Stairs, and Shriharsh P. Tendulkar. Localizing FRBs through VLBI with the Algonquin Radio Observatory 10 m Telescope. , 163(2):65, February 2022. doi: 10.3847/1538-3881/ac3d2f.
- Tomas Cassanelli, Calvin Leung, Pranav Sanghavi, Juan Mena-Parra, Savannah Cary, Ryan Mckinven, Mohit Bhardwaj, Kiyoshi W. Masui, Daniele Michilli, Kevin Bandura, Shami Chatterjee, Jeffrey B. Peterson, Jane Kaczmarek, Chitrang Patel, Mubdi Rahman, Kaitlyn Shin, Keith Vanderlinde, Sabrina Berger, Charanjot Brar, P. J. Boyle, Daniela Breitman, Pragya Chawla, Alice P. Curtin, Matt Dobbs, Fengqiu Adam Dong, Emmanuel Fonseca, B. M. Gaensler, Adaeze Ibik, Victoria M. Kaspi, Khairy Kholoud, T. L. Landecker, Adam E. Lanman, Mattias Lazda, Hsiu-Hsien Lin, Jing Luo, Bradley W. Meyers, Nikola Milutinovic, Cherry Ng, Gavin Noble, Aaron B. Pearlman, Ue-Li Pen, Emily Petroff, Ziggy Pleunis, Brendan Quine, Masoud Rafiei-Ravandi, Andre Renard, Ketan R. Sand, Eve Schoen, Paul Scholz, Kendrick M. Smith, Ingrid Stairs, and Shriharsh P. Tendulkar. A fast radio burst localized at detection to a galactic disk using very long baseline interferometry. arXiv e-prints, art. arXiv:2307.09502, July 2023. doi: 10.48550/arXiv.2307.09502.
- S. Chatterjee, C. J. Law, R. S. Wharton, S. Burke-Spolaor, J. W. T. Hessels, G. C. Bower, J. M. Cordes, S. P. Tendulkar, C. G. Bassa, P. Demorest, B. J. Butler, A. Seymour, P. Scholz, M. W. Abruzzo, S. Bogdanov, V. M. Kaspi, A. Keimpema, T. J. W. Lazio, B. Marcote, M. A. McLaughlin, Z. Paragi, S. M. Ransom, M. Rupen, L. G. Spitler, and H. J. van Langevelde. A direct localization of a fast radio burst and its host., 541(7635):58–61, January 2017. doi: 10.1038/nature20797.
- CHIME Collaboration. An Overview of CHIME, the Canadian Hydrogen Intensity Mapping Experiment., 261(2):29, August 2022. doi: 10.3847/1538-4365/ac6fd9.
- CHIME/FRB Collaboration. The CHIME Fast Radio Burst Project: System Overview. , 863(1):48, August 2018. doi: 10.3847/1538-4357/aad188.
- CHIME/FRB Collaboration, M. Amiri, K. Bandura, M. Bhardwaj, P. Boubel, M. M. Boyce, P. J Boyle, C. . Brar, M. Burhanpurkar, T. Cassanelli, P. Chawla, J. F. Cliche, D. Cubranic, M. Deng, N. Denman, M. Dobbs, M. Fandino, E. Fonseca, B. M. Gaensler, A. J. Gilbert, A. Gill, U. Giri, D. C. Good, M. Halpern, D. S. Hanna, A. S. Hill, G. Hinshaw, C. Höfer, A. Josephy, V. M. Kaspi, T. L. Landecker, D. A. Lang, H. H. Lin, K. W. Masui, R. Mckinven, J. Mena-Parra, M. Merryfield, D. Michilli, N. Milutinovic, C. Moatti, A. Naidu, L. B. Newburgh, C. Ng, C. Patel, U. Pen, T. Pinsonneault-Marotte, Z. Pleunis, M. Rafiei-Ravandi, M. Rahman, S. M. Ransom, A. Renard, P. Scholz, J. R.

Shaw, S. R. Siegel, K. M. Smith, I. H. Stairs, S. P. Tendulkar, I. Tretyakov, K. Vanderlinde, and P. Yadav. A second source of repeating fast radio bursts., 566(7743):235–238, January 2019. doi: 10.1038/s41586-018-0864-x.

CHIME/FRB Collaboration, M. Amiri, B. C. Andersen, K. M. Bandura, M. Bhardwaj, P. J. Boyle,
C. Brar, P. Chawla, T. Chen, J. F. Cliche, D. Cubranic, M. Deng, N. T. Denman, M. Dobbs, F. Q.
Dong, M. Fandino, E. Fonseca, B. M. Gaensler, U. Giri, D. C. Good, M. Halpern, J. W. T. Hessels,
A. S. Hill, C. Höfer, A. Josephy, J. W. Kania, R. Karuppusamy, V. M. Kaspi, A. Keimpema, F. Kirsten,
T. L. Landecker, D. A. Lang, C. Leung, D. Z. Li, H. H. Lin, B. Marcote, K. W. Masui, R. McKinven,
J. Mena-Parra, M. Merryfield, D. Michilli, N. Milutinovic, A. Mirhosseini, A. Naidu, L. B. Newburgh,
C. Ng, K. Nimmo, Z. Paragi, C. Patel, U. L. Pen, T. Pinsonneault-Marotte, Z. Pleunis, M. Rafiei-Ravandi, M. Rahman, S. M. Ransom, A. Renard, P. Sanghavi, P. Scholz, J. R. Shaw, K. Shin, S. R.
Siegel, S. Singh, R. J. Smegal, K. M. Smith, I. H. Stairs, S. P. Tendulkar, I. Tretyakov, K. Vanderlinde,
H. Wang, X. Wang, D. Wulf, P. Yadav, and A. V. Zwaniga. Periodic activity from a fast radio burst source., 582(7812):351–355, June 2020a. doi: 10.1038/s41586-020-2398-2.

CHIME/FRB Collaboration, B. C. Andersen, K. M. Bandura, M. Bhardwaj, A. Bij, M. M. Boyce, P. J. Boyle, C. Brar, T. Cassanelli, P. Chawla, T. Chen, J. F. Cliche, A. Cook, D. Cubranic, A. P. Curtin, N. T. Denman, M. Dobbs, F. Q. Dong, M. Fandino, E. Fonseca, B. M. Gaensler, U. Giri, D. C. Good, M. Halpern, A. S. Hill, G. F. Hinshaw, C. Höfer, A. Josephy, J. W. Kania, V. M. Kaspi, T. L. Landecker, C. Leung, D. Z. Li, H. H. Lin, K. W. Masui, R. McKinven, J. Mena-Parra, M. Merryfield, B. W. Meyers, D. Michilli, N. Milutinovic, A. Mirhosseini, M. Münchmeyer, A. Naidu, L. B. Newburgh, C. Ng, C. Patel, U. L. Pen, T. Pinsonneault-Marotte, Z. Pleunis, B. M. Quine, M. Rafiei-Ravandi, M. Rahman, S. M. Ransom, A. Renard, P. Sanghavi, P. Scholz, J. R. Shaw, K. Shin, S. R. Siegel, S. Singh, R. J. Smegal, K. M. Smith, I. H. Stairs, C. M. Tan, S. P. Tendulkar, I. Tretyakov, K. Vanderlinde, H. Wang, D. Wulf, and A. V. Zwaniga. A bright millisecond-duration radio burst from a Galactic magnetar., 587(7832):54–58, November 2020b. doi: 10.1038/s41586-020-2863-y.

CHIME/FRB Collaboration, Mandana Amiri, Bridget C. Andersen, Kevin Bandura, Sabrina Berger, Mohit Bhardwaj, Michelle M. Boyce, P. J. Boyle, Charanjot Brar, Daniela Breitman, Tomas Cassanelli, Pragya Chawla, Tianyue Chen, J. F. Cliche, Amanda Cook, Davor Cubranic, Alice P. Curtin, Meiling Deng, Matt Dobbs, Fengqiu Adam Dong, Gwendolyn Eadie, Mateus Fandino, Emmanuel Fonseca, B. M. Gaensler, Utkarsh Giri, Deborah C. Good, Mark Halpern, Alex S. Hill, Gary Hinshaw, Alexander Josephy, Jane F. Kaczmarek, Zarif Kader, Joseph W. Kania, Victoria M. Kaspi, T. L. Landecker, Dustin Lang, Calvin Leung, Dongzi Li, Hsiu-Hsien Lin, Kiyoshi W. Masui, Ryan McKinven, Juan Mena-Parra, Marcus Merryfield, Bradley W. Meyers, Daniele Michilli, Nikola Milutinovic, Arash Mirhosseini, Moritz Münchmeyer, Arun Naidu, Laura Newburgh, Cherry Ng, Chitrang Patel, Ue-Li Pen, Emily Petroff, Tristan Pinsonneault-Marotte, Ziggy Pleunis, Masoud Rafiei-Ravandi, Mubdi Rahman, Scott M. Ransom, Andre Renard, Pranav Sanghavi, Paul Scholz, J. Richard Shaw, Kaitlyn Shin, Seth R. Siegel, Andrew E. Sikora, Saurabh Singh, Kendrick M. Smith, Ingrid Stairs, Chia Min

- Tan, S. P. Tendulkar, Keith Vanderlinde, Haochen Wang, Dallas Wulf, and A. V. Zwaniga. The First CHIME/FRB Fast Radio Burst Catalog., 257(2):59, December 2021. doi: 10.3847/1538-4365/ac33ab.
- CHIME/FRB Collaboration, Bridget C. Andersen, Kevin Bandura, Mohit Bhardwaj, P. J. Boyle, Charanjot Brar, Tomas Cassanelli, S. Chatterjee, Pragya Chawla, Amanda M. Cook, Alice P. Curtin, Matt Dobbs, Fengqiu Adam Dong, Jakob T. Faber, Mateus Fandino, Emmanuel Fonseca, B. M. Gaensler, Utkarsh Giri, Antonio Herrera-Martin, Alex S. Hill, Adaeze Ibik, Alexander Josephy, Jane F. Kaczmarek, Zarif Kader, Victoria Kaspi, T. L. Landecker, Adam E. Lanman, Mattias Lazda, Calvin Leung, Hsiu-Hsien Lin, Kiyoshi W. Masui, Ryan McKinven, Juan Mena-Parra, Bradley W. Meyers, D. Michilli, Cherry Ng, Ayush Pandhi, Aaron B. Pearlman, Ue-Li Pen, Emily Petroff, Ziggy Pleunis, Masoud Rafiei-Ravandi, Mubdi Rahman, Scott M. Ransom, Andre Renard, Ketan R. Sand, Pranav Sanghavi, Paul Scholz, Vishwangi Shah, Kaitlyn Shin, Seth Siegel, Kendrick Smith, Ingrid Stairs, Jianing Su, Shriharsh P. Tendulkar, Keith Vanderlinde, Haochen Wang, Dallas Wulf, and Andrew Zwaniga. CHIME/FRB Discovery of 25 Repeating Fast Radio Burst Sources., 947(2):83, April 2023. doi: 10.3847/1538-4357/acc6c1.
- CHIME/Pulsar Collaboration, M. Amiri, K. M. Bandura, P. J. Boyle, C. Brar, J. F. Cliche, K. Crowter,
  D. Cubranic, P. B. Demorest, N. T. Denman, M. Dobbs, F. Q. Dong, M. Fandino, E. Fonseca, D. C.
  Good, M. Halpern, A. S. Hill, C. Höfer, V. M. Kaspi, T. L. Landecker, C. Leung, H. H. Lin, J. Luo,
  K. W. Masui, J. W. McKee, J. Mena-Parra, B. W. Meyers, D. Michilli, A. Naidu, L. Newburgh, C. Ng,
  C. Patel, T. Pinsonneault-Marotte, S. M. Ransom, A. Renard, P. Scholz, J. R. Shaw, A. E. Sikora,
  I. H. Stairs, C. M. Tan, S. P. Tendulkar, I. Tretyakov, K. Vanderlinde, H. Wang, and X. Wang. The
  CHIME Pulsar Project: System Overview., 255(1):5, July 2021. doi: 10.3847/1538-4365/abfdcb.
- J. J. Condon, W. D. Cotton, E. W. Greisen, Q. F. Yin, R. A. Perley, G. B. Taylor, and J. J. Broderick. VizieR Online Data Catalog: 1.4GHz NRAO VLA Sky Survey (NVSS) (Condon+ 1998). VizieR Online Data Catalog, art. VIII/65, November 2002.
- Amanda M. Cook, Mohit Bhardwaj, B. M. Gaensler, Paul Scholz, Gwendolyn M. Eadie, Alex S. Hill, Victoria M. Kaspi, Kiyoshi W. Masui, Alice P. Curtin, Fengqiu Adam Dong, Emmanuel Fonseca, Antonio Herrera-Martin, Jane Kaczmarek, Adam E. Lanman, Mattias Lazda, Calvin Leung, Bradley W. Meyers, Daniele Michilli, Ayush Pandhi, Aaron B. Pearlman, Ziggy Pleunis, Scott Ransom, Mubdi Rahman, Ketan R. Sand, Kaitlyn Shin, Kendrick Smith, Ingrid Stairs, and David C. Stenning. An FRB Sent Me a DM: Constraining the Electron Column of the Milky Way Halo with Fast Radio Burst Dispersion Measures from CHIME/FRB. arXiv e-prints, art. arXiv:2301.03502, January 2023. doi: 10.48550/arXiv.2301.03502.
- J. M. Cordes and T. J. W. Lazio. NE2001.I. A New Model for the Galactic Distribution of Free Electrons and its Fluctuations. arXiv e-prints, art. astro-ph/0207156, July 2002. doi: 10.48550/arXiv.astro-ph/ 0207156.
- C. K. Day, S. Bhandari, A. T. Deller, R. M. Shannon, and V. A. Moss. ASKAP localisation of the FRB 20201124A source. The Astronomer's Telegram, 14515:1, April 2021.

- Wei Deng and Bing Zhang. Cosmological Implications of Fast Radio Burst/Gamma-Ray Burst Associations., 783(2):L35, March 2014. doi: 10.1088/2041-8205/783/2/L35.
- T. Eftekhari and E. Berger. Associating Fast Radio Bursts with Their Host Galaxies. , 849(2):162, November 2017. doi: 10.3847/1538-4357/aa90b9.
- E. Fonseca, B. C. Andersen, M. Bhardwaj, P. Chawla, D. C. Good, A. Josephy, V. M. Kaspi, K. W. Masui, R. Mckinven, D. Michilli, Z. Pleunis, K. Shin, S. P. Tendulkar, K. M. Bandura, P. J. Boyle, C. Brar, T. Cassanelli, D. Cubranic, M. Dobbs, F. Q. Dong, B. M. Gaensler, G. Hinshaw, T. L. Landecker, C. Leung, D. Z. Li, H. H. Lin, J. Mena-Parra, M. Merryfield, A. Naidu, C. Ng, C. Patel, U. Pen, M. Rafiei-Ravandi, M. Rahman, S. M. Ransom, P. Scholz, K. M. Smith, I. H. Stairs, K. Vanderlinde, P. Yadav, and A. V. Zwaniga. Nine New Repeating Fast Radio Burst Sources from CHIME/FRB., 891(1):L6, March 2020. doi: 10.3847/2041-8213/ab7208.
- V. Gajjar, A. P. V. Siemion, D. C. Price, C. J. Law, D. Michilli, J. W. T. Hessels, S. Chatterjee, A. M. Archibald, G. C. Bower, C. Brinkman, S. Burke-Spolaor, J. M. Cordes, S. Croft, J. Emilio Enriquez, G. Foster, N. Gizani, G. Hellbourg, H. Isaacson, V. M. Kaspi, T. J. W. Lazio, M. Lebofsky, R. S. Lynch, D. MacMahon, M. A. McLaughlin, S. M. Ransom, P. Scholz, A. Seymour, L. G. Spitler, S. P. Tendulkar, D. Werthimer, and Y. G. Zhang. Highest Frequency Detection of FRB 121102 at 4-8 GHz Using the Breakthrough Listen Digital Backend at the Green Bank Telescope., 863(1):2, August 2018. doi: 10.3847/1538-4357/aad005.
- David Gordon, Walter Brisken, and Walter Max-Moerbeck. Difxcalc Calc11 for the DiFX Correlator. In Dirk Behrend, Karen D. Baver, and Kyla L. Armstrong, editors, *New Horizons with VGOS*, pages 187–192, December 2016.
- Kasper E. Heintz, J. Xavier Prochaska, Sunil Simha, Emma Platts, Wen-fai Fong, Nicolas Tejos, Stuart D. Ryder, Kshitij Aggerwal, Shivani Bhandari, Cherie K. Day, Adam T. Deller, Charles D. Kilpatrick, Casey J. Law, Jean-Pierre Macquart, Alexandra Mannings, Lachlan J. Marnoch, Elaine M. Sadler, and Ryan M. Shannon. Host Galaxy Properties and Offset Distributions of Fast Radio Bursts: Implications for Their Progenitors., 903(2):152, November 2020. doi: 10.3847/1538-4357/abb6fb.
- G. Jones and K. Bikos. Earth is in a hurry in 2020. https://www.timeanddate.com/time/earth-faster-rotation.html, 2020. Accessed: Sept 16, 2023.
- George H. Kaplan. The IAU resolutions on astronomical reference systems, time scales, and earth rotation models: explanation and implementation. *U.S. Naval Observatory Circulars*, 179, January 2005. doi: 10.48550/arXiv.astro-ph/0602086.
- F. Kirsten, B. Marcote, K. Nimmo, J. W. T. Hessels, M. Bhardwaj, S. P. Tendulkar, A. Keimpema, J. Yang, M. P. Snelders, P. Scholz, A. B. Pearlman, C. J. Law, W. M. Peters, M. Giroletti, Z. Paragi, C. Bassa, D. M. Hewitt, U. Bach, V. Bezrukovs, M. Burgay, S. T. Buttaccio, J. E. Conway, A. Corongiu, R. Feiler, O. Forssén, M. P. Gawroński, R. Karuppusamy, M. A. Kharinov, M. Lindqvist, G. Maccaferri, A. Melnikov, O. S. Ould-Boukattine, A. Possenti, G. Surcis, N. Wang, J. Yuan, K. Aggarwal,

- R. Anna-Thomas, G. C. Bower, R. Blaauw, S. Burke-Spolaor, T. Cassanelli, T. E. Clarke, E. Fonseca, B. M. Gaensler, A. Gopinath, V. M. Kaspi, N. Kassim, T. J. W. Lazio, C. Leung, D. Z. Li, H. H. Lin, K. W. Masui, R. Mckinven, D. Michilli, A. G. Mikhailov, C. Ng, A. Orbidans, U. L. Pen, E. Petroff, M. Rahman, S. M. Ransom, K. Shin, K. M. Smith, I. H. Stairs, and W. Vlemmings. A repeating fast radio burst source in a globular cluster. , 602(7898):585–589, February 2022. doi: 10.1038/s41586-021-04354-w.
- Adam E. Lanman, Bridget C. Andersen, Pragya Chawla, Alexander Josephy, Gavin Noble, Victoria M. Kaspi, Kevin Bandura, Mohit Bhardwaj, P. J. Boyle, Charanjot Brar, Daniela Breitman, Tomas Cassanelli, Fengqiu (Adam) Dong, Emmanuel Fonseca, B. M. Gaensler, Deborah Good, Jane Kaczmarek, Calvin Leung, Kiyoshi W. Masui, B. W. Meyers, Cherry Ng, Chitrang Patel, Aaron B. Pearlman, Emily Petroff, Ziggy Pleunis, Masoud Rafiei-Ravandi, Mubdi Rahman, Pranav Sanghavi, Paul Scholz, Kaitlyn Shin, Ingrid Stairs, Shriharsh Tendulkar, and Andrew Zwaniga. A Sudden Period of High Activity from Repeating Fast Radio Burst 20201124A., 927(1):59, March 2022. doi: 10.3847/1538-4357/ac4bc7.
- Khee-Gan Lee, Metin Ata, Ilya S. Khrykin, Yuxin Huang, J. Xavier Prochaska, Jeff Cooke, Jielai Zhang, and Adam Batten. Constraining the Cosmic Baryon Distribution with Fast Radio Burst Foreground Mapping. arXiv e-prints, art. arXiv:2109.00386, September 2021. doi: 10.48550/arXiv.2109.00386.
- Calvin Leung, Juan Mena-Parra, Kiyoshi Masui, Kevin Bandura, Mohit Bhardwaj, P. J. Boyle, Charanjot Brar, Mathieu Bruneault, Tomas Cassanelli, Davor Cubranic, Jane F. Kaczmarek, Victoria Kaspi, Tom Landecker, Daniele Michilli, Nikola Milutinovic, Chitrang Patel, Ziggy Pleunis, Mubdi Rahman, Andre Renard, Pranav Sanghavi, Ingrid H. Stairs, Paul Scholz, Keith Vanderlinde, and Chime/Frb Collaboration. A Synoptic VLBI Technique for Localizing Nonrepeating Fast Radio Bursts with CHIME/FRB., 161(2):81, February 2021. doi: 10.3847/1538-3881/abd174.
- D. R. Lorimer and M. Kramer. Handbook of Pulsar Astronomy. 2012.
- D. R. Lorimer, M. Bailes, M. A. McLaughlin, D. J. Narkevic, and F. Crawford. A Bright Millisecond Radio Burst of Extragalactic Origin. *Science*, 318(5851):777, November 2007. doi: 10.1126/science. 1147532.
- J. P. Macquart, J. X. Prochaska, M. McQuinn, K. W. Bannister, S. Bhandari, C. K. Day, A. T. Deller, R. D. Ekers, C. W. James, L. Marnoch, S. Osłowski, C. Phillips, S. D. Ryder, D. R. Scott, R. M. Shannon, and N. Tejos. A census of baryons in the Universe from localized fast radio bursts., 581 (7809):391–395, May 2020. doi: 10.1038/s41586-020-2300-2.
- Alexandra G. Mannings, Wen-fai Fong, Sunil Simha, J. Xavier Prochaska, Marc Rafelski, Charles D. Kilpatrick, Nicolas Tejos, Kasper E. Heintz, Keith W. Bannister, Shivani Bhandari, Cherie K. Day, Adam T. Deller, Stuart D. Ryder, Ryan M. Shannon, and Shriharsh P. Tendulkar. A High-resolution View of Fast Radio Burst Host Environments., 917(2):75, August 2021. doi: 10.3847/1538-4357/abff56.

- B. Marcote, Z. Paragi, J. W. T. Hessels, A. Keimpema, H. J. van Langevelde, Y. Huang, C. G. Bassa,
  S. Bogdanov, G. C. Bower, S. Burke-Spolaor, B. J. Butler, R. M. Campbell, S. Chatterjee, J. M. Cordes,
  P. Demorest, M. A. Garrett, T. Ghosh, V. M. Kaspi, C. J. Law, T. J. W. Lazio, M. A. McLaughlin,
  S. M. Ransom, C. J. Salter, P. Scholz, A. Seymour, A. Siemion, L. G. Spitler, S. P. Tendulkar, and
  R. S. Wharton. The Repeating Fast Radio Burst FRB 121102 as Seen on Milliarcsecond Angular
  Scales., 834(2):L8, January 2017. doi: 10.3847/2041-8213/834/2/L8.
- B. Marcote, K. Nimmo, J. W. T. Hessels, S. P. Tendulkar, C. G. Bassa, Z. Paragi, A. Keimpema, M. Bhardwaj, R. Karuppusamy, V. M. Kaspi, C. J. Law, D. Michilli, K. Aggarwal, B. Andersen, A. M. Archibald, K. Bandura, G. C. Bower, P. J. Boyle, C. Brar, S. Burke-Spolaor, B. J. Butler, T. Cassanelli, P. Chawla, P. Demorest, M. Dobbs, E. Fonseca, U. Giri, D. C. Good, K. Gourdji, A. Josephy, A. Yu. Kirichenko, F. Kirsten, T. L. Landecker, D. Lang, T. J. W. Lazio, D. Z. Li, H. H. Lin, J. D. Linford, K. Masui, J. Mena-Parra, A. Naidu, C. Ng, C. Patel, U. L. Pen, Z. Pleunis, M. Rafiei-Ravandi, M. Rahman, A. Renard, P. Scholz, S. R. Siegel, K. M. Smith, I. H. Stairs, K. Vanderlinde, and A. V. Zwaniga. A repeating fast radio burst source localized to a nearby spiral galaxy. , 577 (7789):190–194, January 2020. doi: 10.1038/s41586-019-1866-z.
- Kiyoshi Masui, Hsiu-Hsien Lin, Jonathan Sievers, Christopher J. Anderson, Tzu-Ching Chang, Xuelei Chen, Apratim Ganguly, Miranda Jarvis, Cheng-Yu Kuo, Yi-Chao Li, Yu-Wei Liao, Maura McLaughlin, Ue-Li Pen, Jeffrey B. Peterson, Alexander Roman, Peter T. Timbie, Tabitha Voytek, and Jaswant K. Yadav. Dense magnetized plasma associated with a fast radio burst. , 528(7583):523–525, December 2015. doi: 10.1038/nature15769.
- Kiyoshi W. Masui, J. Richard Shaw, Cherry Ng, Kendrick M. Smith, Keith Vanderlinde, and Adiv Paradise. Algorithms for FFT Beamforming Radio Interferometers. *arXiv e-prints*, art. arXiv:1710.08591, October 2017. doi: 10.48550/arXiv.1710.08591.
- J. Mena-Parra, C. Leung, S. Cary, K. W. Masui, J. F. Kaczmarek, M. Amiri, K. Bandura, P. J. Boyle, T. Cassanelli, J. F. Cliche, M. Dobbs, V. M. Kaspi, T. L. Landecker, A. Lanman, J. L. Sievers, J. L. Sievers, and Chime/Frb Collaboration. A Clock Stabilization System for CHIME/FRB Outriggers., 163(2):48, February 2022. doi: 10.3847/1538-3881/ac397a.
- D. Michilli, A. Seymour, J. W. T. Hessels, L. G. Spitler, V. Gajjar, A. M. Archibald, G. C. Bower, S. Chatterjee, J. M. Cordes, K. Gourdji, G. H. Heald, V. M. Kaspi, C. J. Law, C. Sobey, E. A. K. Adams, C. G. Bassa, S. Bogdanov, C. Brinkman, P. Demorest, F. Fernandez, G. Hellbourg, T. J. W. Lazio, R. S. Lynch, N. Maddox, B. Marcote, M. A. McLaughlin, Z. Paragi, S. M. Ransom, P. Scholz, A. P. V. Siemion, S. P. Tendulkar, P. van Rooy, R. S. Wharton, and D. Whitlow. An extreme magneto-ionic environment associated with the fast radio burst source FRB 121102. , 553(7687): 182–185, January 2018. doi: 10.1038/nature25149.
- D. Michilli, K. W. Masui, R. Mckinven, D. Cubranic, M. Bruneault, C. Brar, C. Patel, P. J. Boyle, I. H. Stairs, A. Renard, K. Bandura, S. Berger, D. Breitman, T. Cassanelli, M. Dobbs, V. M. Kaspi,

- C. Leung, J. Mena-Parra, Z. Pleunis, L. Russell, P. Scholz, S. R. Siegel, S. P. Tendulkar, and K. Vanderlinde. An Analysis Pipeline for CHIME/FRB Full-array Baseband Data., 910(2):147, April 2021. doi: 10.3847/1538-4357/abe626.
- Enno Middelberg and Uwe Bach. High resolution radio astronomy using very long baseline interferometry. Reports on Progress in Physics, 71(6):066901, June 2008. doi: 10.1088/0034-4885/71/6/066901.
- C. Ng, K. Vanderlinde, A. Paradise, P. Klages, K. Masui, K. Smith, K. Bandura, P. J. Boyle, M. Dobbs, V. Kaspi, A. Renard, J. R. Shaw, I. Stairs, and I. Tretyakov. CHIME FRB: An application of FFT beamforming for a radio telescope. In XXXII International Union of Radio Science General Assembly & Scientific Symposium (URSI GASS) 2017, page 4, August 2017. doi: 10.23919/URSIGASS.2017. 8105318.
- F. Nicastro, S. Mathur, and M. Elvis. Missing Baryons and the Warm-Hot Intergalactic Medium., 319: 55–57, 2008. doi: 10.1126/science.1151400.
- K. Nimmo, J. W. T. Hessels, F. Kirsten, A. Keimpema, J. M. Cordes, M. P. Snelders, D. M. Hewitt, R. Karuppusamy, A. M. Archibald, V. Bezrukovs, M. Bhardwaj, R. Blaauw, S. T. Buttaccio, T. Cassanelli, J. E. Conway, A. Corongiu, R. Feiler, E. Fonseca, O. Forssén, M. Gawroński, M. Giroletti, M. A. Kharinov, C. Leung, M. Lindqvist, G. Maccaferri, B. Marcote, K. W. Masui, R. Mckinven, A. Melnikov, D. Michilli, A. G. Mikhailov, C. Ng, A. Orbidans, O. S. Ould-Boukattine, Z. Paragi, A. B. Pearlman, E. Petroff, M. Rahman, P. Scholz, K. Shin, K. M. Smith, I. H. Stairs, G. Surcis, S. P. Tendulkar, W. Vlemmings, N. Wang, J. Yang, and J. P. Yuan. Burst timescales and luminosities as links between young pulsars and fast radio bursts. Nature Astronomy, 6:393–401, February 2022a. doi: 10.1038/s41550-021-01569-9.
- K. Nimmo, D. M. Hewitt, J. W. T. Hessels, F. Kirsten, B. Marcote, U. Bach, R. Blaauw, M. Burgay, A. Corongiu, R. Feiler, M. P. Gawroński, M. Giroletti, R. Karuppusamy, A. Keimpema, M. A. Kharinov, M. Lindqvist, G. Maccaferri, A. Melnikov, A. Mikhailov, O. S. Ould-Boukattine, Z. Paragi, M. Pilia, A. Possenti, M. P. Snelders, G. Surcis, M. Trudu, T. Venturi, W. Vlemmings, N. Wang, J. Yang, and J. Yuan. Milliarcsecond Localization of the Repeating FRB 20201124A. , 927(1):L3, March 2022b. doi: 10.3847/2041-8213/ac540f.
- C. H. Niu, K. Aggarwal, D. Li, X. Zhang, S. Chatterjee, C. W. Tsai, W. Yu, C. J. Law, S. Burke-Spolaor, J. M. Cordes, Y. K. Zhang, S. K. Ocker, J. M. Yao, P. Wang, Y. Feng, Y. Niino, C. Bochenek, M. Cruces, L. Connor, J. A. Jiang, S. Dai, R. Luo, G. D. Li, C. C. Miao, J. R. Niu, R. Anna-Thomas, J. Sydnor, D. Stern, W. Y. Wang, M. Yuan, Y. L. Yue, D. J. Zhou, Z. Yan, W. W. Zhu, and B. Zhang. A repeating fast radio burst associated with a persistent radio source., 606(7916):873–877, June 2022. doi: 10.1038/s41586-022-04755-5.
- S. Pappas. Humans contribute to earth's wobble, scientists say. https://www.scientificamerican.com/article/humans-contribute-to-earth-rsquo-s-wobble-scientists-say/, 2018. Accessed: Sept 16, 2023.

- R. A. Perley and B. J. Butler. An Accurate Flux Density Scale from 50 MHz to 50 GHz., 230(1):7, May 2017. doi: 10.3847/1538-4365/aa6df9.
- L. Piro, G. Bruni, E. Troja, B. O'Connor, F. Panessa, R. Ricci, B. Zhang, M. Burgay, S. Dichiara, K. J. Lee, S. Lotti, J. R. Niu, M. Pilia, A. Possenti, M. Trudu, H. Xu, W. W. Zhu, A. S. Kutyrev, and S. Veilleux. The fast radio burst FRB 20201124A in a star-forming region: Constraints to the progenitor and multiwavelength counterparts., 656:L15, December 2021. doi: 10.1051/0004-6361/202141903.
- E. Platts, A. Weltman, A. Walters, S. P. Tendulkar, J. E. B. Gordin, and S. Kandhai. A living theory catalogue for fast radio bursts., 821:1–27, August 2019. doi: 10.1016/j.physrep.2019.06.003.
- Z. Pleunis, D. Michilli, C. G. Bassa, J. W. T. Hessels, A. Naidu, B. C. Andersen, P. Chawla, E. Fonseca, A. Gopinath, V. M. Kaspi, V. I. Kondratiev, D. Z. Li, M. Bhardwaj, P. J. Boyle, C. Brar, T. Cassanelli, Y. Gupta, A. Josephy, R. Karuppusamy, A. Keimpema, F. Kirsten, C. Leung, B. Marcote, K. W. Masui, R. Mckinven, B. W. Meyers, C. Ng, K. Nimmo, Z. Paragi, M. Rahman, P. Scholz, K. Shin, K. M. Smith, I. H. Stairs, and S. P. Tendulkar. LOFAR Detection of 110-188 MHz Emission and Frequency-dependent Activity from FRB 20180916B., 911(1):L3, April 2021a. doi: 10.3847/2041-8213/abec72.
- Ziggy Pleunis, Deborah C. Good, Victoria M. Kaspi, Ryan Mckinven, Scott M. Ransom, Paul Scholz, Kevin Bandura, Mohit Bhardwaj, P. J. Boyle, Charanjot Brar, Tomas Cassanelli, Pragya Chawla, Fengqiu (Adam) Dong, Emmanuel Fonseca, B. M. Gaensler, Alexander Josephy, Jane F. Kaczmarek, Calvin Leung, Hsiu-Hsien Lin, Kiyoshi W. Masui, Juan Mena-Parra, Daniele Michilli, Cherry Ng, Chitrang Patel, Masoud Rafiei-Ravandi, Mubdi Rahman, Pranav Sanghavi, Kaitlyn Shin, Kendrick M. Smith, Ingrid H. Stairs, and Shriharsh P. Tendulkar. Fast Radio Burst Morphology in the First CHIME/FRB Catalog., 923(1):1, December 2021b. doi: 10.3847/1538-4357/ac33ac.
- K. M. Rajwade, M. B. Mickaliger, B. W. Stappers, V. Morello, D. Agarwal, C. G. Bassa, R. P. Breton, M. Caleb, A. Karastergiou, E. F. Keane, and D. R. Lorimer. Possible periodic activity in the repeating FRB 121102. , 495(4):3551–3558, July 2020. doi: 10.1093/mnras/staa1237.
- V. Ravi, M. Catha, L. D'Addario, S. G. Djorgovski, G. Hallinan, R. Hobbs, J. Kocz, S. R. Kulkarni, J. Shi, H. K. Vedantham, S. Weinreb, and D. P. Woody. A fast radio burst localized to a massive galaxy., 572(7769):352–354, August 2019. doi: 10.1038/s41586-019-1389-7.
- Andre Recnik, Kevin Bandura, Nolan Denman, Adam D. Hincks, Gary Hinshaw, Peter Klages, Ue-Li Pen, and Keith Vanderlinde. An Efficient Real-time Data Pipeline for the CHIME Pathfinder Radio Telescope X-Engine. arXiv e-prints, art. arXiv:1503.06189, March 2015. doi: 10.48550/arXiv.1503.06189.
- Roberto Ricci, Luigi Piro, Francesca Panessa, Brendan O'Connor, Simone Lotti, Gabriele Bruni, and Bing Zhang. Detection of a persistent radio source at the location of FRB20201124A with VLA. *The Astronomer's Telegram*, 14549:1, April 2021.
- Pranav Sanghavi, Calvin Leung, Kevin Bandura, Tomas Cassanelli, Jane Kaczmarek, Victoria M. Kaspi, Kholoud Khairy, Adam Lanman, Mattias Lazda, Kiyoshi W. Masui, Juan Mena-Parra, Daniele

- Michilli, Ue-Li Pen, Jeffrey B. Peterson, Mubdi Rahman, and Vishwangi Shah. TONE: A CHIME/FRB Outrigger Pathfinder for localizations of Fast Radio Bursts using Very Long Baseline Interferometry. arXiv e-prints, art. arXiv:2304.10534, April 2023. doi: 10.48550/arXiv.2304.10534.
- L. G. Spitler, P. Scholz, J. W. T. Hessels, S. Bogdanov, A. Brazier, F. Camilo, S. Chatterjee, J. M. Cordes, F. Crawford, J. Deneva, R. D. Ferdman, P. C. C. Freire, V. M. Kaspi, P. Lazarus, R. Lynch, E. C. Madsen, M. A. McLaughlin, C. Patel, S. M. Ransom, A. Seymour, I. H. Stairs, B. W. Stappers, J. van Leeuwen, and W. W. Zhu. A repeating fast radio burst., 531(7593):202–205, March 2016. doi: 10.1038/nature17168.
- S. P. Tendulkar, C. G. Bassa, J. M. Cordes, G. C. Bower, C. J. Law, S. Chatterjee, E. A. K. Adams, S. Bogdanov, S. Burke-Spolaor, B. J. Butler, P. Demorest, J. W. T. Hessels, V. M. Kaspi, T. J. W. Lazio, N. Maddox, B. Marcote, M. A. McLaughlin, Z. Paragi, S. M. Ransom, P. Scholz, A. Seymour, L. G. Spitler, H. J. van Langevelde, and R. S. Wharton. The Host Galaxy and Redshift of the Repeating Fast Radio Burst FRB 121102. , 834(2):L7, January 2017. doi: 10.3847/2041-8213/834/2/L7.
- Shriharsh P. Tendulkar, Armando Gil de Paz, Aida Yu. Kirichenko, Jason W. T. Hessels, Mohit Bhardwaj, Fernando Ávila, Cees Bassa, Pragya Chawla, Emmanuel Fonseca, Victoria M. Kaspi, Aard Keimpema, Franz Kirsten, T. Joseph W. Lazio, Benito Marcote, Kiyoshi Masui, Kenzie Nimmo, Zsolt Paragi, Mubdi Rahman, Daniel Reverte Payá, Paul Scholz, and Ingrid Stairs. The 60 pc Environment of FRB 20180916B., 908(1):L12, February 2021. doi: 10.3847/2041-8213/abdb38.
- D. Thornton, B. Stappers, M. Bailes, B. Barsdell, S. Bates, N. D. R. Bhat, M. Burgay, S. Burke-Spolaor,
  D. J. Champion, P. Coster, N. D'Amico, A. Jameson, S. Johnston, M. Keith, M. Kramer, L. Levin,
  S. Milia, C. Ng, A. Possenti, and W. van Straten. A Population of Fast Radio Bursts at Cosmological Distances. Science, 341(6141):53-56, July 2013. doi: 10.1126/science.1236789.
- B. Vollmer, B. Gassmann, S. Derrière, T. Boch, M. Louys, F. Bonnarel, P. Dubois, F. Genova, and F. Ochsenbein. The SPECFIND V2.0 catalogue of radio cross-identifications and spectra. SPECFIND meets the Virtual Observatory., 511:A53, February 2010. doi: 10.1051/0004-6361/200913460.
- J. M. Yao, R. N. Manchester, and N. Wang. A New Electron-density Model for Estimation of Pulsar and FRB Distances., 835(1):29, January 2017. doi: 10.3847/1538-4357/835/1/29.
- Bing Zhang. Unexpected emission pattern adds to the enigma of fast radio bursts. , 582(7812):344-346, June 2020. doi: 10.1038/d41586-020-01713-x.